STARS

Electronic Theses and Dissertations, 2004-2019

2019

Fluid Flow Characteristics of a Co-Flow Fluidic Slot Jet Thrust Augmentation Propulsion System

Brian Garrett
University of Central Florida

FLUID FLOW CHARACTERISTICS OF A CO-FLOW FLUIDIC SLOT JET THRUST AUGMENTATION PROPULSION SYSTEM

by

BRIAN GARRETT
B.S. Mechanical/Environmental Engineering May 2016, East Carolina University

A thesis submitted in partial fulfillment of the requirements
for the degree of Master of Science
in the Department of Mechanical and Aerospace Engineering
in the College of Engineering and Computer Science
at the University of Central Florida
Orlando, Florida

Summer Term
2019

ABSTRACT

The UAV industry is booming with investments in research and development on improving UAV systems in order to increase applications and reduce costs of the use of these machines. Current UAV machines are developed according to the quadcopter design which has a rotary propulsion system which provides the lift needed for the aerial vehicles. This design has some flaws; namely safety concerns and noise/vibration production both of which come from the rotary propulsion system. As such, a novel propulsion system using slip stream air passed through high performance slot jets is proposed and analysis of the fluid characteristics is presented in this report.

The test section for the experiment is developed using 3D printed ABS plastic airfoils modified with internal cavities where pressurized air is introduced and then expelled through slot jets on the pressure side of the airfoils. Entrainment processes develop in the system through high momentum fluid introduction into a sedentary secondary fluid. Entrainment is governed by pressure gradients and turbulent mixing and so turbulent quantities that measure these processes are extracted and analyzed according to the independent variable's effects on these quantities. Pitot probe testing extracted one dimensional fluid information and PIV analysis is used to characterize the two-dimensional flow aspects.

High slot jet velocities are seen to develop flows dominated by convection pushing momentum mixing downstream reducing the mixing while low slot jet speeds exhibit higher mass fluxes and thrust development. Confinement spacing is seen to cause a decrease in flow velocity and thrust as the spacing is decreased for high speed runs. The most constricted cross sectional runs showed high momentum mixing and developed combined self-similar flow through higher boundary layer interactions and pressures, but this also hurt thrust development. The Angle of Attack of the

assembly proved to be the most important variable. Outward angling showed the influence of coanda effects but also demonstrated the highest bulk fluid flow with turbulence driven momentum mixing. Inward angling created combined fluid flow downstream with high momentum mixing upstream driven by pressure. Minimal mixing is seen when the airfoils are not angled and high recirculation zones along the boundaries. The optimal setup is seen to when the airfoils are angled outwards where the highest thrust and bulk fluid movement is developed driven by the turbulent mixing induced by the increasing cross sectional area of the system.

This thesis is dedicated to my hard-working, and loving mom. When I was 5 my dad passed away and my mom had to pick up the pieces of her and my life. Taking on the responsibility of a single parent all the while mourning the loss of someone you love so dearly must have been devastating. But my mom did not lose a step and got right back into working and providing for me which allowed me to get to where I am today and for that I am grateful beyond words. You have always been a hard-working mother and setting an example for me in life, and I cannot describe how much I thank you for the example you have set and how much I love you.

ACKNOWLEDGMENTS

I would like to thank my faculty advisor Kareem Ahmed, for the help and time he has given me so that I could have written this paper. I would also like to acknowledge my friends, family, and girlfriend for the help they have given in my academic career. Without all the support this paper would not have been possible.

TABLE OF CONTENTS

LIST OF FIGURES

LIST OF TABLES

CHAPTER 1 INTRODUCTION

Turbulent flow fields have become a widely studied topic due to its passive ability to provide many different benefits to a wide range of applications. Heating and air condition systems such as boilers and other industrial devices can see improved efficiencies through turbulent flows inducing higher energy transfer in the corresponding shear layers [1]. Turbulence between two substances create a turbulent mixing layer which can be used to increase combustion efficiency and the mixing rates between chemicals [2]. Propulsions systems can also see improvements through turbulent induction of exhaust gases leading to higher efficiencies of primary jets as well as the idea for Vertical Takeoff or Landing Vehicles (VTOL)[3]. With a just a few of the operational benefits listed above turbulent flows are seen to have a wide range benefits for numerous different systems. Thrust production is an important area of study to allow for flight and can see benefits with the optimization of the associated turbulent flows for such systems which are utilized everywhere. Unmanned Aerial Vehicles (UAVs) have seen increased attention from both military and private industries in the past years. Government, enterprise, and consumer drones are the three main segments in the drone industry, and all are estimated to see an increase in expenditures and sales in the coming years as reported by Business Insider. This would amount to an estimated 12 billion dollars in sales of drones in 2021, which means a growth rate of about 7.6% of sales every year [4]. As reported in the Drone Year in review: 2017 there was an increase in military drone and UAV utilization from 2016 to 2017, allowing the military to conduct assaults, gather intelligence, and more. There was also an increase in funding for commercial delivery UAVs, research into minimizing UAVs, and continuous research into increasing thrust production efficiency among

other areas [5]. So, the UAV industry has seen increases in funding and interest in the past and is estimated to continue to see interest in the future demonstrating huge possibilities in the field.

Multiple novel ideas for producing and optimizing thrust have been researched and proposed. Entrainment is a turbulent flow process where secondary quiescent fluid is engulfed into a primary turbulent flow due to turbulent mixing and pressure gradients in the system. This process develops secondary velocities going from the sedentary fluid to the primary fluid leading to a passive increase in mass of the primary flow [6]. This passive increase in mass flow leads to a passive thrust augmentation according to Newtons law[2][6]. These are the ideas behind Co Flow Slot Jet Thrust Augmentation concepts which are being used in VTOL aircrafts and the aerospace industry today. This sort of propulsion system has multiple benefits such as less noise production, and higher safety margins during usage when compared to the rotary propulsion system seen in UAV designs. Implementation of this coflow propulsion system will reduce the moving parts in the system and reduce noise as vena contract and cavitation effects are neglected; which is also the main motivation behind this work.

This paper will analyze an experiment conducted on two airfoils installed in a horizontal arrangement with slot jets introduced in between them. The velocity and pressure in the fluid leaving the slot jets start to entrain the quiescent fluid between the airfoils creating secondary flows leading to the production of a thrust force. The propulsion system idea would be to use the quadcopter design seen in many UAV designs today but replace the four rotary blade propulsion system with a 4 ring/shroud system with slot jets on the inside which would provide the thrust needed according to the theory of entrainment. Different airfoil configurations were analyzed using two different methods; Pitot Probe testing, and Particle Image Velocimetry testing. One

Dimensional flow characteristics and Two-dimensional flow characteristics including Mean flow measurements, Halfwidth Thickness, Shear Layer Thickness, Turbulent Intensity and Reynolds Shear Stress are extracted and discussed. The affects the independent variables have on these quantities and the calculated thrust leads to the designation of an optimal propulsion system assembly. Discussion on the uncertainty propagation and the driving forces behind the momentum mixing seen in the different test assemblies further validate why the assembly with the airfoils angled outwards is believed to be the optimal setup. The report ends with a conclusion summarizing the key fluid characteristics and momentum mixing driving forces along with supplemental fluid data in the appendix.

CHAPTER 2 LITERATURE REVIEW

The commercial Unmanned Aerial Vehicle (UAV) industry is booming due to the extensive applications UAV's have and the cheap, simple designs of the aircrafts. Arroyo reports on drones being used in precision agriculture to estimate nitrogen levels in crops so they can precisely administer fertilization in Mexico [7]. Skjervold reports on using UAV's as an inexpensive and effective means of surveillance and presenting a way to lower costs of drone surveillance allowing entities with less money to benefit [8]. The commercial UAV sector is vast, but with an interestingly limited amount of UAV aircraft designs. Essentially, the entire commercial UAV industry revolves around the quadcopter design due to its simplicity, ability to scale, simple to control and many more benefits. The quadcopter aircraft design consists of a central body composed of the computer and wireless receiver held together in a housing. This bundled section is then connected to four arms each of which have rotors at the end which provide the thrust. An example of the design, as well as UAV's being used in the field of work can be seen below in Figure 2.1 [7] and 2.2[8]:

Figure 2.1 Example of a quadcopter design used in industry

Figure 2.2 Examples quadcopter UAV's flying in synchronous
patterns

Even with the popularity of the quadcopter and the multiple benefits that it has there are some problems as well; namely safety, and noise/vibrations of the aircraft.

Drone operation is based on wireless signals and onboard computers, so interference of wireless signals can cause drones to fly away and crash causing harm. "Fly away" drones have been found crashing into planes causing as much damage as a goose strike [9]. There are also reported incidents where people and properties have been hurt due to "flyaway" drones crashing [10][11]. These drones fly using a rotary propulsion system and the components of the four rotor propulsion system are composed of multiple moving parts. Having such excessive rotating parts amplifies the

5

hazards of crashing Unmanned Aerial Vehicle's with problems such as debris scatter and projectile injury possibilities.

Noise and related vibrations stemming from the noise are another negative aspect of the quadcopter design creating negative impacts on the environment, structural integrity of the aircraft and possible uses of the aircraft. Brentner said it best when experimenting on aerodynamically generated noise from rotary engines, "Noise has been an undesirable byproduct of aerospace vehicles from the time of early aircrafts until now." [12] Helicopter rotors which are like the rotors in quadcopter designs are reportedly the main producers of aerodynamic noise as said by Kusyumov. Kusyumov reports that the main reason of the rotor creating noise is the excessive energy produced from the acceleration force generated by the moving blades. This acceleration from the rotating parts creates a large updraft vortex along the main rotor as well as multiple other leading edge vortices creating a complex flow pattern in the blades which when this gets disturbed creates noise [13]. The generated noise is and these disturbances in the flow can generate vibrations in the arms and housing of the vehicle which can hurt the structural integrity of the vehicle.

As these problems can be detrimental, this paper will discuss an alternative propulsion system for the quadcopter design which should increase the safety margin and decrease noise and vibration of the system. The purposed system is replacing the four-rotor system with a four-ringed shroud system with slots on the inside of the shroud where pressurized air gets pumped out of. Pumping this air out of a bounded fluidic system will instigate the process of entrainment and turbulent mixing which become driving producers of thrust. This system will lessen the amount of parts of the UAV by eliminating the rotary components and reduce the aerodynamic noise of the aircraft by negating vena contracta effects through a fifth order contraction and operate with fluid pressures

6

low enough to negate cavitation. Below in Figure 2.3 is a 3D model generated of the proposed system incorporated onto a quadcopter vehicle [43]:

Figure 2.3 Proposed UAV Propulsion Design

With the shroud setup seen above in Figure 2.3: fluid flow is seen to be bounded by the walls of the shroud creating a bounded shear flow field. Such a setup is expected to exhibit similar fluid features to that of a duel plane jet velocity field in literature with some notable differences as well. The difference being that the proposed setup has an opening between the slot jets where more air is pulled into the system and that one side of each slot jet is bounded. Regardless combined flow as is seen in the dual jet systems is seen for the 1inch -5AOA setups and all the .5 inch setups, so dual jet interactions are present in the system.

Dual plane jet velocity fields have been studied and multiple key features have been documented in experiments by Tanaka, Anderson, Nasr, and more [1][15-19]. Tanaka is one of the first to perform experiments on a duel jet setup and found that the flow field can be broken up into three main regions; recirculation region, merging region (between the merge point and combined point), and combined region (after the combined point). Looking at the open side of the airfoils away from

the boundary it was seen that these dual jet interactions come into play for this experiment and an example of the general flow field expected in the system can be seen below
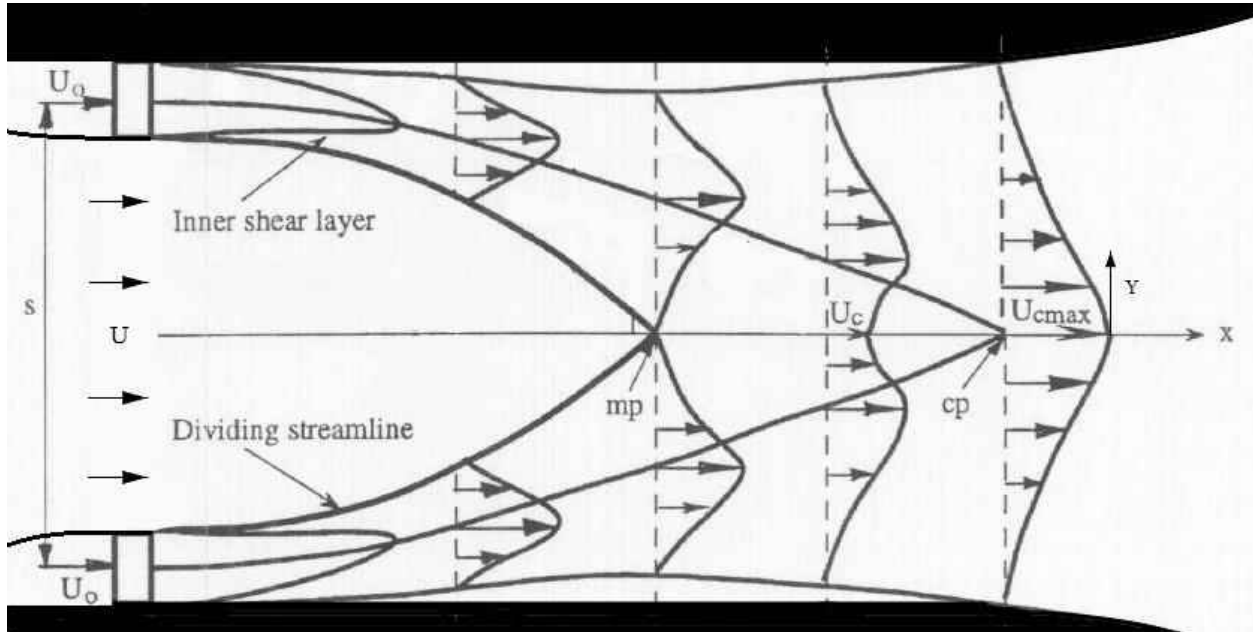
Figure 2.4 Edited Turbulent Plane Parallel Dual Jet Velocity field assumed to be prevalent in the experiment

Where U is the entrained fluid velocities, U_O is the slot jet velocities, s is the confinement spacing, x is the system centerline axis, y is the transverse direction, mp is the merge point, cp is the combined point, and U_C is the centerline velocity. Figure 2.4 above is an edited version of the dual plane jet velocity field with the main difference being that there is no walled boundary between the slot jet exits and a boundary next to each slot jet. The open section between the slot jets effect the recirculation region to some extent by introducing extra mass flows into the system upstream, but the extent of this interaction is beyond the scope of this work.

For dual jets it is seen entrainment and the walled boundary between the jets create a sub atmospheric pressure region between the jets. This region is dominated by two major contra rotating vortices creating negative pressure and velocities but is only established due to the

8

presence of the wall [1][15][19]. Removing this walled boundary creates a vacuum effect in the sub atmospheric region due to entrainment where air is pulled into the system creating secondary flows into the system. This secondary movement is governed by the entrainment and turbulent mixing effects of the two slot jets. This process takes place in a region of the flow known as the shear layer which is developed due to the pressure differences and turbulence seen in the primary jet flows compared to the secondary entrainment flows. Spall has found that the merge point of the jet velocities moves downstream when the distance between the jets is increased and when the turbulent kinetic energy leaving the jets is increased [1].Tanaka also explains that increasing the spacing between the jets leads to a more dispersed distribution of turbulent intensities, an increase in half width distance from the jet centerline, and a sharper max axial velocity decrease in the combined flow region[15][16].

The two main fluid equations governing the dynamics seen in this experiment are known as the conservation of mass and conservation of momentum equations. For the system analyzed here, the flow is assumed two dimensional, so these governing equations are edited a bit and the related equations are seen below in Equations 1 to 3 [25]:

$$\frac{du}{dx} + \frac{dv}{dy} = 0 \tag{1}$$

$$\rho\left(\frac{du}{dt} + u\frac{du}{dx} + v\frac{du}{dy}\right) = -\frac{dp}{dx} + \mu\nabla^2 u + \rho f_x \tag{2}$$

$$\rho\left(\frac{dv}{dt} + u\frac{dv}{dx} + v\frac{dv}{dy}\right) = -\frac{dp}{dy} + \mu\nabla^2 v + \rho f_y \tag{3}$$

Where ρ is density, μ is viscosity, u is velocity in the x-direction, v is the velocity in the y-direction, P is the pressure forces, and f is external body forces. Equation 1 above states that turbulent time dependent mass flow is conserved in a system, and the mass flowing into the airfoils assembly equals the mass flowing out of the system. The two sources of mass flowing into the system is assumed to be the slot jet flows and entrainment flows while the sum of each is assumed to be the flow leaving the system. For this experiment, the slot jets were not seeded and so the flow was not quantified but the secondary flows were seeded and analyzed. Equations 2 and 3 shows the conservation of momentum equations which state that momentum convection through the system is affected by pressure, viscous damping, and non-conservative body forces along with a time dependent unsteady aspect as well. These equations model fluid features in laminar flows and only need some editing to model turbulent features as well, more information of which will be discussed in the next section.

UAV's have gained a lot of popularity and increased research funding due to the multiple applications across multiple industries they have. The simple design of UAV's has some problems focused on the four rotor engine the quadcopter designs have. The proposed propulsion system would replace the current rotary system with the driving forces of the system being entrainment and turbulent mixing. These fluidic processes develop due to the pressure differences and instabilities in the system and augment molecular momentum dissipation allowing for a greater number of air molecules to pick up on the increased momentum energy introduced by the slot jets of the system. Entrainment and turbulent mixing have been studied extensively by many people such as Davidson, Hu, Winant showing a wealth of information available for the experiment [2] [6] [14]. Current general applications of this concept can be seen in the Dyson bladeless fan

assemblies and in the aerospike engine, more details of both can be found in the related text in the references cited section [20] [21].

The current examples of the fluidic processes dominant in the proposed propulsion system as well as the numerous experiments conducted help to validate the propulsion system tested in this experiment. The dominant processes are governed and quantified according to the shear layer development through the system. The shear layer is the area in the velocity field where there are the highest velocity gradients indicating high momentum dissipation form high to low momentum. In this area vortex rollup is induced which leads to an area of high vorticity and turbulence following the flow. Due to the high turbulence and vorticity in the shear layer, high momentum dissipation is present as well and as such Shear Layer Propagation is the most important fluidic feature of the system and will be further analyzed in the following section [6][26]. The aerodynamic feature of thrust is the final optimized desired output which developed according to the momentum interactions in the system. Thrust augmentation is the term used to specify the additional thrust generated due to the dual jet interactions in this proposed system and as such further discussion of general Slot Jet Thrust Augmentation will be presented in the following sections as well.

2.1 Shear Layer Propagation:

On one side of the high momentum slot jet flows are dominant dual jet interactions which are dependent on entrainment and turbulent mixing. Both process that dual jet interactions depend on are quantified by shear layer development in the system, as they both happen in the shear layer. Shear layer development and interactions are well quantified for single jet setups and less so for dual jet setups, but the concepts can be applied in both cases. Primary high momentum flow ejected

11

into a quiescent pool of secondary low momentum fluid can be analyzed as a free shear turbulent

jet flow. A diagram of a single turbulent free shear flow can be seen below in Figure 2.4:
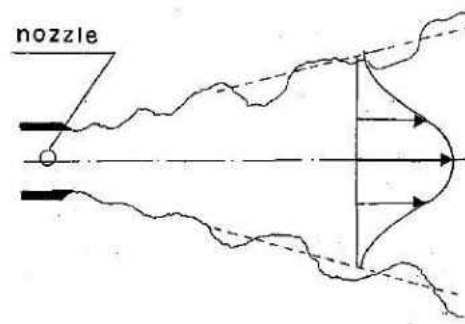
Figure 2.5 Turbulent Jet flow velocity profile and shear layer boundaries [25]

The velocity gradients developed from momentum dissipation when the flow leaves the jet exit

can be seen and demonstrate the bounds of the shear layer in the flow [6][23]. Right at the jet exit,

the shear layer initiates at the flow boundary and propagates towards the center of the jet flow and

at the same time outwards away from the jet flow center. A limited segment of flow right at the jet

exit centerline is not affected by the dissipation at the jet flow edges. This segment follows the

flow but is soon engulfed into the shear layer through momentum mixing and the point where the

shear layer dominates is known as the potential core [6]. Potential core information was not

extracted since the slot jet flow was not seeded but can be an area of further research of this

propulsion system.

12

Right as the flow exits the jet a layer of fluid experiences momentum dissipation which develops velocity gradients between the secondary and primary fluid in the co flow system. In this area of momentum dissipation and velocity gradients, vortex rollup occurs producing vorticity and increasing turbulence [2][6][25]. This area of vorticity generation and high turbulence is called the shear layer and has been stated to be the defining fluidic characteristic of this experiment. This high vorticity and turbulence augment the molecular momentum dissipation and engulfs packets of the secondary fluid. This engulfment coupled with pressure differences between the fast and slow fluids initiates entrainment processes as well. The shear layer outer boundaries are indicated in Figures 2.4 and 2.5 where the jet flow interact with the secondary fluid, where clear turbulence is seen in the chaotic motion of the lines.

A system with different speed fluid flows, pressures are also seen to be different in different sections of the system. Looking at Equations 2 and 3 above and assuming inviscid, steady flow the momentum equation can reduce to Bernoulli's equation which can be seen below in Equation 4 [22]:

$$P_1 + \frac{1}{2}\rho V_1^2 + \rho g h_1 = P_2 + \frac{1}{2}\rho V_2^2 + \rho g h_2 \tag{4}$$

Bernoulli's equation can also be stated in words; an increase in velocity results in a decrease in pressure for inviscid flows. This can also be stated according to energies; an increase in kinetic energy results in a decrease in potential energy of the system. Bernoulli showed that fluid flowing through a pipe with a cross sectional construction would speed up in the constructed cross section but also decrease in pressure [22]. Relating this velocity-pressure interaction to free shear flows one sees that the high velocity turbulent flow entering the quiescent fluid creates a pressure difference. This pressure differential is non-local according to the Biot-Savart law and felt

13

everywhere in the fluidic system [6]. Such a non-local pressure differential propagates through the whole system leading to a vacuum effect developing between the slow fluid having higher pressures and the fast fluid having low pressure. This vacuum effect coupled with turbulent mixing creates a tendency of the secondary flow to move into the primary flow, which developed a passive increase in the mass flux of the primary jet flows.

The two main fluidic processes effecting momentum mixing are dependent on highly turbulent flows which are large areas of research due to the chaotic nature. Turbulence can have multiple benefits in fluidic system depending on the application, but quantification of the flow is difficult due to the time dependent chaotic fashion of the flows. Reynolds decomposition has been used to break the velocity domain of a turbulent system into a time average part and fluctuating time dependent part of velocity [6][27]. Below in Equation 5 can be seen an example of Reynolds decomposition used on the U velocity component of the system:

$$U(x, y, t) = \bar{u}(x, y) + u'(x, y, t) \tag{5}$$

The fluctuating component seen in Equation 5 above is the component of the flow that encompasses the turbulent fluctuations coming from vorticity generation in the flow. One indicator of how strong the turbulence has become in the system is by looking at the time dependent components magnitude. So, taking the root mean square (Urms) of that fluctuating component was done for each velocity field of each experiment and presented in the results section, all of which show that turbulence increases downstream.

Using Reynolds decomposition and replacing the velocities seen in the momentum conservation equations, otherwise known as the Navier Stokes Equations, and applying averaging laws the Reynolds Averaged Navier Stokes Equations (RANS) is developed and seen below [6]:

14

$$\frac{d}{dt}\int (\rho \bar{u}_i)dV = -\int (\rho \bar{u}_i)(\bar{u}_i * dS) + \int \tau_{ij} - \rho\overline{u_i'u_j'}dS - \int \bar{p}\,dS \qquad (6)$$

Where the overbar quantities are time averaged and quantities with ' are fluctuating components. This is a tensor equation used to analyze time dependent chaotic turbulent flows and is very similar to the momentum conservation equations presented earlier except one main difference, the $\rho\overline{u_i'u_j'}$ term [6]. This is called the Reynolds stress term and quantifies the turbulent mixing seen in the system. Extracting velocity information for this experiment, the Reynolds stress was calculated for each experimental assembly at the center or the shear layer where mixing is highest.

For Computational Fluid Dynamics (CFD) simulations and using mathematical processes to simulate flows, it can be found that this term is not discreetly solvable and requires some assumptions to estimate a solution. Popular assumptions made are known as Prandtl's mixing length theory and Boussinesq Turbulent eddy viscosity theory seen below in Equations 7 and 8 [6][27]:

$$u_x' = l\left(\frac{d\overline{u_x}}{dy}\right) \qquad (7)$$

$$\tau_{xy} + \tau_{xy}^R = \rho(v + v_t)\frac{d\overline{u_x}}{dy} \qquad (8)$$

Where l is a large eddy length scale, τ_{xy} is the flow shear stress, τ_{xy}^R is the Reynolds stress, v_t is called the turbulent eddy viscosity and v is viscosity. Prandtl's Mixing length theory (Equation 7) estimates the turbulent momentum diffusion of flow as it goes downstream relating the length scale of turbulent diffusion with the gradient of the U velocity in the transverse direction. Boussinesq eddy viscosity theory (Equation 8) relates the unanswerable Reynolds stress term to a constant known as eddy viscosity and it used widely in turbulence modeling as a closure technique to the

Reynolds Stress. Boussinesq's theory also shows how turbulence augments the shear stress developed in laminar flow.

Examining Equations 6, 7 and 8; high velocity gradients and vorticity generation are seen to promote momentum diffusion all of which is localized to the shear layer. This again shows that looking at the path of the shear layer can tell us where momentum is mixing, and vorticity is generated validating the importance of shear layer propagation. An example of shear layer propagation is seen in Figures 2.4 for dual jet assemblies, and Figure 2.5 for single shear jet flows. The dual jet setups experiments have shown that the shear layers curve towards each other as the fluid moves downstream and the meeting point is dependent on slot jet spacing and upstream turbulence generation. The merging region after the shear layers have meet is seen to have the greatest amount of momentum mixing but since the shear layers have meet, entrainment has stopped, and no more mass is pulled into the system. An optimal setup which allows for enough fluid to enter the system to augment the thrust and allows for enough mixing to occur is the aim for this experiment.

Momentum is being transferred from high energy particles to low energy particles which takes physical form in velocities of these particles. The shear layer is the area of the fluid where this dissipation occurs, and the highest velocity gradients are seen. The distance between the jet center flow (Max velocity flow) and the point where the velocity of the particle is half that max flow is known as the halfwidth thickness. This thickness is a good indicator of momentum dissipation and presented in the results section for each experimental assembly; large thicknesses indicating fast dissipation and researchers such a Tanaka use it to characterize turbulent dual jet flows as well[15][16].

Vorticity generation and advection has been stated to be an important factor on the turbulent mixing in the system and is analyzed according to the mathematical principle of the curl of the momentum equation. Below in Equation 9 we see the 2D vorticity equation which comes from taking the curl of the momentum conservation equation [6][22]:

$$\frac{D\omega}{Dt} = (\omega * \nabla)u + \nu * \nabla^2 \omega - \nabla(\frac{P}{\rho}) \tag{9}$$

Where ω is vorticity, ∇ is the 2D gradient operator, u is the mean flow, ν is viscosity and P is pressure assuming homogenous isotropic flow. Looking at Equation 5 we can see that vorticity acts in an advection-diffusion manner where it is generated and then convected downstream with the mean flow. Pressure is developed in the system as is seen in Equations 2 and 3, but since the flow is non reacting it is believed that the pressure does not affect the vorticity in a significant manner. Examining Equation 9 vortical eddies are seen to form at high velocity gradients (along the shear layer), and viscous effects are similarly seen to act as a dampening agent. It is also known that under Kelvins Theorem and Taylors Frozen Field hypothesis, vortex tube structures which form according to Equation 9 are convected downstream as if frozen in the fluid with zero circulation around the tube [6][22][23]. Examination of Equation 9 again validates the importance of velocity gradients as well as minimizing viscous effects for vorticity generation.

With the chaotic behaviors in turbulent flows, experiments are conducted in order to find trends in certain systems which can be used in optimizing these systems. Self-similar flow is a common trend in fluid dynamics and indicates flow at some downstream distance where the velocity profiles over distance can be collapsed into a single profile [22][28]. For multiple

parallel jets, self-similar flow is reached some distance downstream depending on jet opening width, jet separation distances, and more. But once reached, self-similar flow acts like a single jet flow with a faster decrease in jet streamwise velocities according to Tanka [15][16]. Self-similar flow is seen in the results section for the 1-inch inward angled airfoil runs, and for the .5-inch runs. According to time averaged experiments by Wygnanski, two dimensional turbulent jets attain a self-similar velocity profile some 50-diameter length downstream. Wygnanski's experiments also show that small scale eddies form first from axial velocities and then create perturbations which spread in the other coordinate directions of the flow [29]. Crow's experiments demonstrate turbulence does obtain some orderly structure some distance downstream related to the Strouhal number and the fundamental wave, and these structures can be affected by jet exit effects [30]. Ho also finds eddy structures being developed in the jet and shear layers grow exponentially downstream and the distribution of such structures are affected by jet exit perturbations via the Kelvin-Helmholtz instability [24].

Downstream vortex dynamics is affected by the upstream vortex production. Such effects are shown in Winants experiments; where he shows that downstream turbulent mixing layers are dominated by large scale vortical structures with axes perpendicular to the direction of the mean flow; comparable to fully developed turbulent flows. Winant also saw that the large scale vortical structures begin to pair and revolve around each other downstream and follow the mean flow coupled together (Vortex Pairing as he called it). This can increase mixing but can lead to a decrease in entrainment depending on vortex production frequency and spacing between each vortex [2]. Theoretical considerations and experimental considerations discussed

give an idea of how vorticity is coupled to turbulent mixing which is all centered in the shear/mixing layer. Some key fluidic properties taken from these reports are jet exit parameters, eddy structure development and downstream length all of which effect the mixing layer and momentum diffusion of this system.

It is known that jet exit parameters such as jet exit shape and jet exit contractions effect turbulent flows and create a cascading effect downstream in the development of the vorticity of turbulent flows. Verma and Ho each experimented on moderate to small aspect ratio elliptic slot jets shear layers; and both concluded that elliptic slot jets attained greater mixing and entrainment rates than that of circular jets [24][31]. This greater rate of mixing was due to the 3D azimuthal distortion and axis switching properties such jets have. Verma even studied the effects of tripped turbulence using notches at the jet exit which also led to an increase in the mixing rate [31]. Gutmark experimented on orifice and tapered elliptic slot jets and found increased mixing in both when compared to circular jets. The tapered orifice showed greatest mixing enhancement with higher near field momentum spreading [32]. Hussain also experimented on different contraction shapes leading to slot jets ejectors and found more abrupt or sharper contractions lessen the downstream distances of where uniform velocity is attained [33]. Sfeir analyzed 3D square jets and concluded that shear layer interactions were closely related to elliptic slot jet properties downstream and the jet mouth properties but did not see much increase in mixing layer properties [34]. Transient jets are another area of recent study, and according to an experiment by Hu there is an increase in entrainment from large scale structures during jet deceleration [14]. Thus, flow preconditioning, jet exit parameters,

vortical eddies development are seen to effect turbulent mixing in the systems in different ways of these different experiments discussed. But this also means that such development can be controlled to an extent opening the research into optimizing turbulence for momentum mixing as is the purpose for this experiment. Fluid preconditioning and transient jet conditions were outside the scope of this experiment but are more areas where further research can be performed.

2.2 Ejector Thrust Augmentation and Slot Jet Technologies:

Dual jet fluid dynamic aspects have been discussed, but aerodynamic aspects related to thrust augmentation and slot jet technologies also play an important role in this experiment. Thrust augmentation is a process by which thrust produced may be increased over its normal value by some secondary [passive] means as said by the Merriam Webster dictionary [35]. There have been many different approaches to trust augmentation both mechanical and fluidic; some fluidic processes include synthetic jet actuators, counter flows, co-flow, and more [36]. An ejector is a pneumatic device that pumps a secondary fluid into a primary flow and is used in co-flow systems [37]. Thrust vectoring is an extension of the idea of thrust augmentation but focuses with altering thrust direction instead of magnitude and as such both terms will be used interchangeably.

But the fluidic system presented in this experiment consists of a co-flow system with two slot jet ejectors augmenting thrust due to dual jet entrainment behaviors. On one side of the slot jet flows dual jet interactions dominate and entrainment is present as has been explained. On the bounded side of the slot jets, Coanda effects are seen to develop and can be seen in the velocity contours presented in the appendices. Coanda effects describe the tendency of the jet flows to follow the airfoil boundaries due to entrainment as well [37]. When flow is ejected into a secondary fluid

close to a boundary, pressure differences and turbulence initiate entrainment as was described regarding dual jet interactions. On the side where the boundary is these secondary flows towards the jet flow develop a suction effect between the jet flow and boundary pulling the jet flow toward the boundary [36][37][38]. This creates a passive flow control mechanism on the fluid direction and leads to thrust vectoring dynamics[36][39]. But such components in the system analyzed for this paper are symmetrical and directional considerations are assumed to be negligible, solely the augmentation components are of importance. Entrainment alters the direction of flow and pulls in more flow and so is seen to be a major driving force in the thrust development of the proposed propulsion system.

In order to calculate thrust, Equation 2 is used assuming steady, inviscid flow and negligible pressure differences between the upstream and downstream parts of the system. Under such assumptions, Equation 2 turns into Equation 10 seen below:

$$F = \dot{m}(V_e - V_i) \tag{10}$$

Where F is the thrust force, $\dot{m}$ is mass flow rate in and out, and V is exit and initial velocities in the system. So, it is seen that pulling in more mass through entrainment and transferring as much momentum to this mass increasing the velocity differences in the system will optimize thrust production. Bevilaqua and Heiser have conducted multiple experiments on thrust augmentation concepts involving an injector shroud experimental setup under different conditions. Both authors provide a thrust augmentation ratio equation dependent on mass flow seen below in Equation 11 [37][43]:

$$\psi = \sqrt{1 + \frac{\dot{m}_e}{\dot{m}_\iota}} \tag{11}$$

Where ψ is the thrust augmentation ratio, $\dot{m}_e$ is the mass flow exiting the system, and $\dot{m}_\iota$ is the initial mass flow into the system. Such a ratio provides a good evaluation marker for this experiment and will be used in the results section to evaluate the different experimental setups.

A major current application for thrust augmentation is the study of Vertical or Short Take-Off and Landing (V/STOL) aircraft capabilities, which enhances aircraft maneuverability and effectiveness for the military [40][43]. By using co-flow thrust vectoring the exhaust gases exiting the engines can be recirculated and ejected into the main flow nozzle. The gases are injected close to the boundaries of the nozzle initiating shear layer interactions and coanda effects [38]. These processes then alter the main flow by either introducing more mass and/or altering the exiting flow direction through viscous effects thus creating a passive ability to manipulate the thrust. Saghafi reports that thrust can be vectored up to 29 degrees in any direction, while Banazadeh reports thrust vectoring up to 90 degrees all of which support the idea and feasibility of V/STOL aircrafts [36][40][41]. An example of an aircraft called the F-35B fighter jet with V/STOL abilities can be seen below in Figure 2.5; Bevilaqua provides information on his research into the design of the aircraft and its VTOL abilities in his related report [42]:
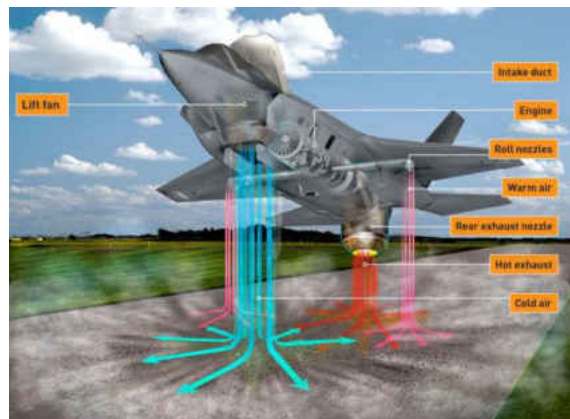
Figure 2.6 F-35 Fighter Jet [Google]

CHAPTER 3 EXPERIMENTAL SETUP

3.1 Experimental Overview

An experiment was conducted at the Propulsion and Energy Research Laboratory (PERL) in the Mechanical and Aerospace Engineering Department at the University of Central Florida. Two airfoils were constructed using acrylonitrile butadiene styrene plastic; or ABS plastic using a 3D printer. The two airfoils were then assembled between two clear acrylic plates allowing for alterations of the setup for multiple experiments. The test assembly was then mounted on a track system to allow for Pitot Probe Testing and PIV analysis. The Pitot Probe measurements aided in the calculation of thrust and analysis of one dimensional fluid characteristics of the system. PIV analysis was conducted afterwards using laser illuminated air flow particles in order to analyze the two dimensional fluid properties of the system and develop an optimized system.

3.1.1 Test Section

The test airfoils were developed using the NACA0024 airfoil design and modified to include slot jets at the quarter chord location on the pressure sides of the airfoils. Each airfoil was 5.5 in (13.97 cm) long, 1.31 in (3.33 cm) wide, and 3 in (7.62 cm) deep. On the suction side of the airfoils two ¼ in NPT holes were drilled; each located .625 in. from the sides and with .75 in. between the holes. Below in Figure 3.1 can be seen the completed experimental setup for the airfoil assembly [44]:
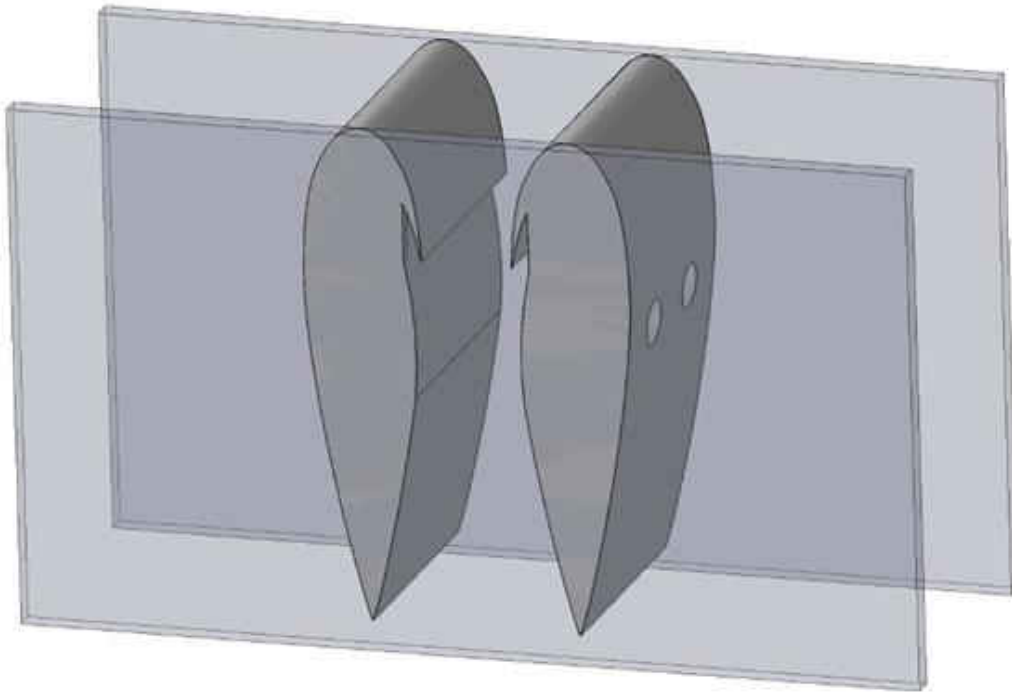
Figure 3.1 Experimental Setup of the two airfoils and acrylic plates holding the airfoils

Below in Figures 3.2 and 3.3 can be seen the assembly drawings of the attachment hose holes and the cross section of the center of the airfoils [44]:
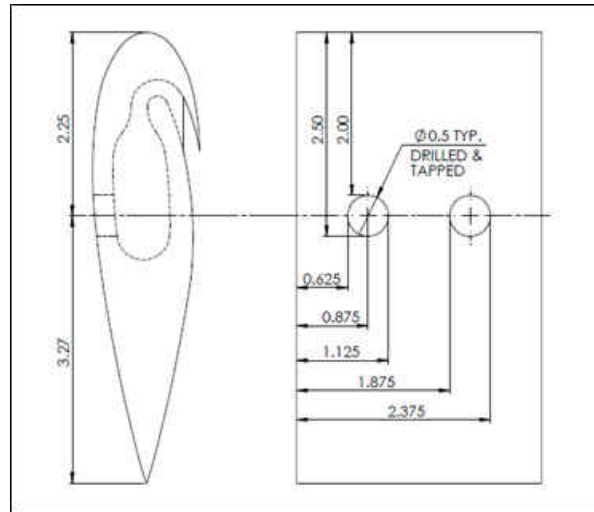
Figure 3.2 Attachments hose technical drawing
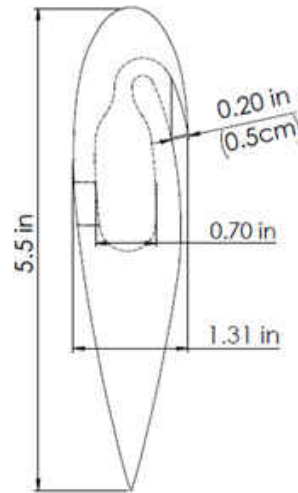
Figure 3.3 Airfoil central cross section technical drawing

Inside each airfoil is a cavity which can be seen in the figures above. This cavity allowed for the pressurization and then exit of the airflow introduced from the attached hoses. The exit of the cavity has a nozzle design using a 5th order polynomial nozzle reduction design to best minimize frictional losses from the contraction. The flow is then turned and ejected into the quiescent fluid with at a certain velocity; such design aspects can be seen in Figures 3.2 and 3.3 above.

25

The airfoils were attached to two pieces of Plexiglass Acrylic sheets using Scotch .75 in. Two-Sided tape to allow for alterations of the assembly for multiple experimental setups. Shop air provided the airflow into the airfoil holes on the suction side of the airfoils. From the wall, a ¼ in. NPT nozzle attached the ½ in. ID high pressure hosing to the airflow. One section was teed off to allow for a 0-200 PSI multipurpose pressure gauge to be used to monitor the flow introduced to the airfoils. Following downstream of the flow the hose was separated by a wye pipe fitting, allowing air to flow to each airfoil. Another wye fitting was then used to allow for two more connections to the two drilled holes on the back of each airfoil before the hose was connected to the airfoils.

3.2 Pitot Probe Testing

Pitot Probes are sensors used to measure pressures in different fluid flows. Pitot probes use fluid meniscus levels in aligned tubes which rise and fall according to Bernoulli's theory and changing pressures. The changing levels or stagnation pressure changes is equal to static pressure plus dynamic pressure. For this experiment a seven-hole pitot probe was used with .5mm static pressure holes. The main dynamic pressure line had an inner diameter of 2 mm. The two lines were then connected to a Supco DDM55 Dual Input Digital Manometer with LCD Display to measure the pressure differential in inches of water.

The Pitot Probe testing setup can be seen below in Figure 3.4 [44]:
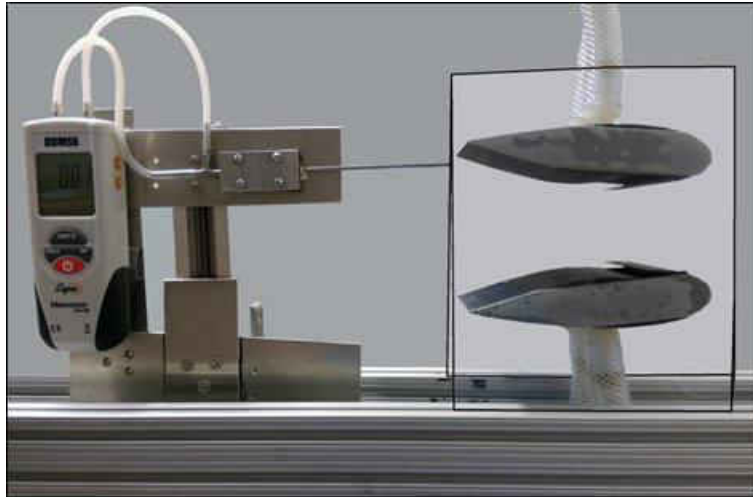
Figure 3.4 Pitot Probe Test Setup

The test assembly was built by attaching the digital manometer to a mount which also held the pitot probe. A Velmex A15 Screw Drive UniSlide was placed on an 80/20 rail to allow for the pitot probe assembly to translate vertically to allow for measurement of different pressure values at different heights between the trailing edges of the airfoils. Two 80/20 rails were laid on perpendicular bars to allow for the test section plexiglass plate edges to be placed into the cavity of the rails. The airfoil assembly was then locked into place using four L-shaped sliding brackets. The Pitot Probe assembly was placed behind the airfoil assembly aligning the transverse moving rail with the downstream position of the airfoils to allow for direct pressure readings of the flow leaving the airfoils. The entire assembly was leveled to assure the flow leaving the airfoil tail would directly enter the main pitot probe pressure tube to minimize static hole readings of the pressure which would lead to invalid readings. The Pitot Probe section was then locked into place by two L brackets. It is assumed that three-dimensional flow effects are minimal due to the chord length being long compared to the airfoil depth. The manometer was set to averaging mode due to

27

the turbulent flows in the system leading to time varying readings so that the measured pressure is a time averaged pressure in inches of water.

The recorded pressure data was used to calculate the velocities exiting the airfoil assembly. Using Bernoulli's equation seen above in Equation 4 and assuming inviscid, steady flow the pressure readings can be restructured into velocity readings. The recorded stagnation pressure of the manometer is assumed the pressure in the moving fluid, ignoring potential energies and any initial pressures the pressure reading is turned into velocity readings using the following Equation 12, which is derived from Equation 4:

$$V = \sqrt{\frac{2P}{\rho}}$$

(12)

Where V is velocity, P is pressure, and ρ is density.

Three different flow pressures were tested; 15, 20 and 25 PSI. To begin recording data the pitot probe was placed directly on top of the trailing edge of the bottom airfoil and the flow was initiated. The pressure gauge in the high-pressure hose introducing the shop air was used to gauge the flow to the correct PSI readings stated earlier. The airflow was then recorded for a minimum of 40 seconds contingent on the time the shop air was able to sustain the desired pressure levels. Once the average pressure measurements were obtained, two additional measurements were obtained using the same process to verify the readings. Once the data was recorded the transverse moving bar was unlocked and the pitot probe was raised .15 in (.381 cm), and the experiment repeated to obtain a new pressure reading. This process was repeated until the top of the airfoil was reached. Upon completion of a single test configuration the test apparatus was disassembled, and the airfoils were reset to the next configuration.

A separation distance of 2, 1.5, and 1 inches were tested each with different flow pressures stated. Referring to a report by Tanaka, it is estimated that jet reattachment happens at a length of about 15-19 times the jet diameter downstream [15][16]. Looking at this reference and data Tanaka published, it is seen that attachment will occur for the jet flow exiting the slot jets and 2-inch separation can be used as the furthest separation point of the airfoils before attachment will not occur. Traversing small increments of transverse length, a large enough sample set of data could be taken where then the ensemble average over the 40 seconds of data collection could be used. Once this was done for each different pressure of flow for each separation distance and airfoil angle, the assembly was reassembled according to the next experiment to be performed.

In order to accurately place the airfoils back on the plexiglass sheets a 1:1 scale drawing was placed under the plexiglass and the airfoils were aligned with the scaled drawing. The airfoils were re-taped down using the double-sided tape. Such caution was taken in order to assure a linear flow between the airfoils because nonlinear airfoils can cause unwanted turbulence in the flow. Below in Table 3.1 can be seen a table of all the test cases for the Pitot Probe Testing where there are 8 experimental assemblies run at different slot jet pressures:

Table 3.1 Pitot Probe Test Cases

Case Number	Angle of Attack (degrees)	Slot Separation (in)	Pressure (PSI)	Entrainment
1	0	2	25	Yes
2	0	2	20	Yes
3	0	2	15	Yes
4	-5	2	25	Yes
5	-5	2	20	Yes
6	-5	2	15	Yes
7	5	2	25	Yes
8	5	2	20	Yes
9	5	2	15	Yes
10	0	1.5	25	Yes
11	0	1.5	20	Yes
12	0	1.5	15	Yes
13	-5	1.5	25	Yes
14	-5	1.5	20	Yes
15	-5	1.5	15	Yes
16	5	1.5	25	Yes
17	5	1.5	20	Yes
18	5	1.5	15	Yes
19	0	1	25	Yes
20	0	1	20	Yes
21	0	1	15	Yes
22	5	1	25	Yes
23	5	1	20	Yes
24	5	1	15	Yes

3.3 PIV

High speed Particle Image Velocimetry (PIV) was employed to non-intrusively characterize the two dimensional aspects of the velocity field in the test assembly. Utilizing a high-speed laser and camera, particles were moved through the system and illuminated using the laser. The high-speed camera then recorded the illuminated flow, and a deconvolution function was used to determine flow rates among other flow quantities.

3.3.1 Test Section Setup

To acquire PIV measurements the laser, camera and test section all had to be setup for testing and aligned as needed for testing. The test assemblies were broken into two test sections, the Middle section right at the slot jet exits and the Bottom section at the tail end of the airfoil assembly. First, the LEE Laser LDP-200MQG Dual Laser and Photron Fastcam SA1.1 675K-M2 camera were positioned in order to set the location of the test assembly. The laser was turned on and sent through a Newport Plano-Convex N-Bk AR.14 coated leans with 50.8 mm diameter to focus the beam. The laser then was passed through a Newport Plano-Concave N-Bk7 AR.14 coated cylindrical lens that is 12.7 mm high, 25.4mm wide, and with a -25mm Focal Length as well in order to turn the laser beam into a laser sheet.

The camera was placed on a tripod and maneuvered such that either side of the camera was within 1mm proximity from the laser sheet. Such alignment allowed for proper imaging of the flow test section for PIV analysis. The camera was then fitted with either an AF-S DX Nikon 18-140mm f/3,5-5.6G or a Nikkon 50mm f/1.2 lens depending on the experiment, and then conjoined with a Vello Manuel Extension Tube Set. A picture of the laser setup can be seen below in Figure 3.5 and a picture of the PIV analysis setup can be seen in Figure 3.6 [43]:
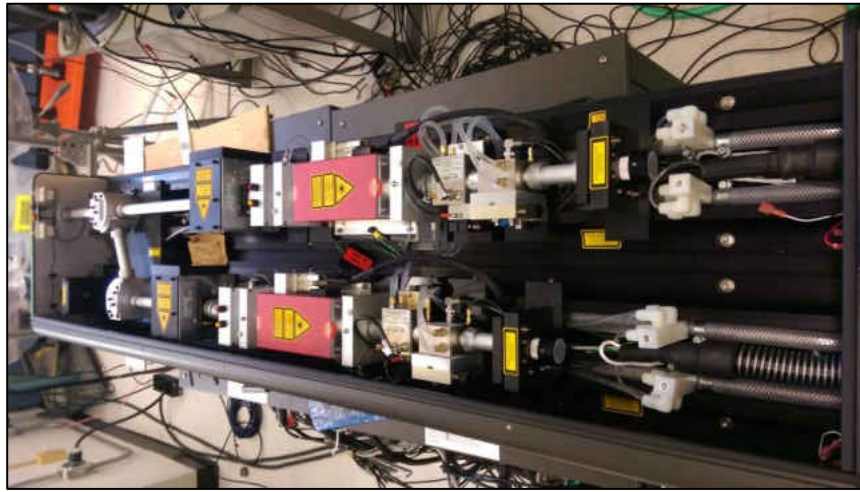
Figure 3.5 Lee Laser LDP-200MQG Dual Laser
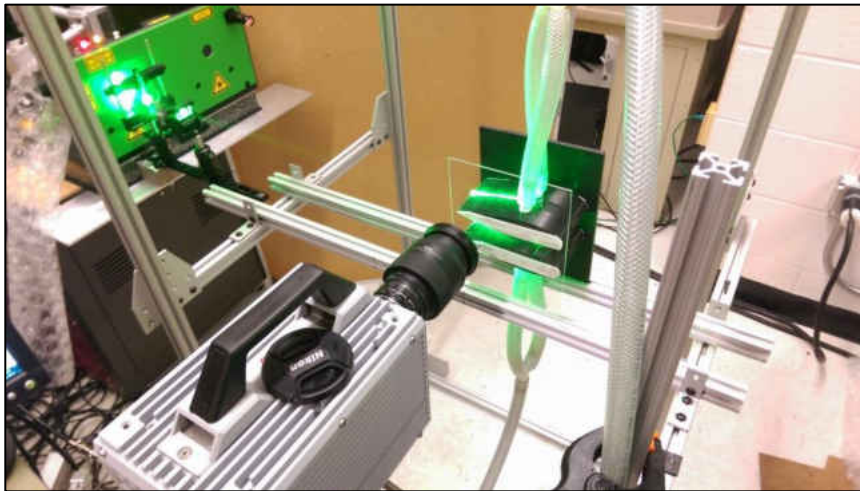
Figure 3.6 PIV Analysis Setup

3.3.2 PIV Test Conditions

The multiple components used to record the data required close synchronization in order to record

valid data. A high enough concentration of particles was required in order to photograph the flow,

and as such the Ate-Aerotect wind tunnel smoke generator had to run about 1 minutes prior to

starting the experiment. This particle cloud was built up in front of the test assembly and once a sufficient concentration of particles was reached, flow was initiated in the airfoils. Then once the desired pressure level was reached in the slot jet flow, the PIV system was activated.

The camera and laser were controlled using a BNC Model 575 Pulse/Delay Generator. This was programmed to send TTL signals to either the camera or laser at appropriate times. The sequence first fired the Photron Fastcam followed by a first pulse suppression (fps) signal to the laser followed by a signal firing laser one and the laser two. The laser pulses were separated by a time of 19 microseconds allowing for high speed imagery to be captured. The laser and camera signals were setup such that the laser was activated with every frequency pulse for the duration of the pulse, and the camera captures a frame for every leading edge of the TTL signal. The sequence was repeated at a frequency of 10 kHz. The data collecting took approximately 2 seconds to complete, in which time approximately 20,000 images were taken. The camera, laser timing sequences can be seen below in Table 3.2 [44], and the PIV Test Setups showing 5 different experimental assemblies can be seen below that in Table 3.3 [44]:

Table 3.2 Timing Box Settings

System Component	Time Delay Form Initiation (µs)	TTL Signal Duration (µs)	Signal Output
Camera	0	0.05	Single Shot
Fps signal	10	10	Single Shot
Laser 1	90	10	Duty Cycle
Laser 2	109	10	Duty Cycle

Table 3.3 PIV Test Cases

Case Number	Separation Distance (in)	Angle of Attack	PSI	Airfoil Section
1	0.5	0	25	Mid
2	0.5	0	25	Bottom
3	0.5	0	20	Mid
4	0.5	0	20	Bottom
5	0.5	0	15	Mid
6	0.5	0	15	Bottom
7	0.5	5	25	Mid
8	0.5	5	20	Mid
9	0.5	5	20	Bottom
10	1	0	25	Mid
11	1	0	25	Bottom
12	1	0	20	Mid
13	1	0	20	Bottom
14	1	0	25	Top
15	1	0	20	Top
16	1	5	25	Mid
17	1	5	25	Bottom
18	1	5	20	Mid
19	1	5	20	Bottom
20	1	-5	25	Mid
21	1	-5	25	Bottom
22	1	-5	20	Mid
22	1	-5	20	Bottom
23	1	-5	30	Bottom

Below in Figures 3.7-3.12 can be seen a diagram for each airfoil configuration experimented on during the PIV analysis:
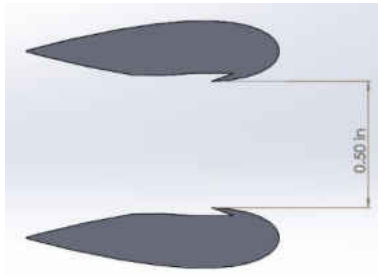
Figure 3.7 .5 in 0 Angle of Attack
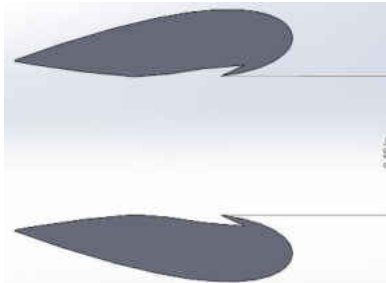
Figure 3.8 5 in. 5-degree Angle of
Attack inward
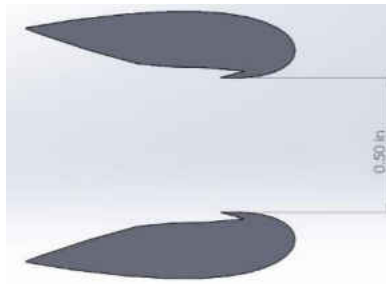
Figure 3.9 5 in. 5-degree Angle of
Attack outward
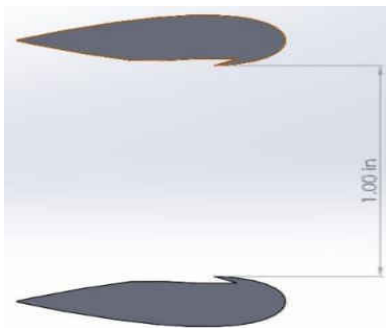
Figure 3.10 1 in. 0 Angle of Attack

35
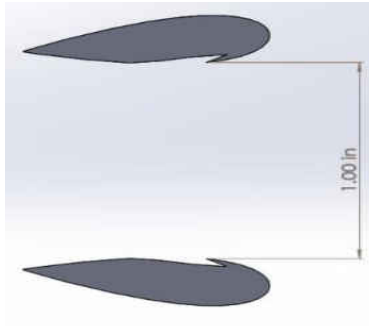
Figure 3.11 1 in. 5 degree Angle of
Attack inward
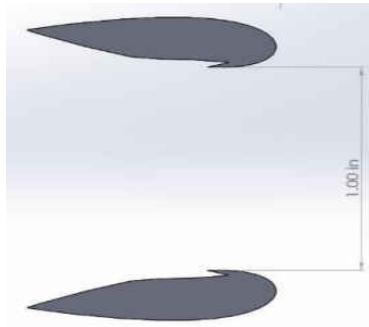
Figure 3.12 1 in. 5 degree Anlge of
Attack outward

CHAPTER 4 RESULTS

In total 13 experimental assemblies were constructed; 8 setups used for Pitot Probe testing and 5

setups for the PIV testing; all of which is outlined in Tables 3.1 and 3.3 where the slot jets pressure

runs are seen to range between 15, 20, or 25PSI. The process of conducting the experiments

consisted of assembling the airfoils a certain distance apart, angling the airfoils outwards

(+5AOA), inwards (-5AOA) or setting them horizontal (0AOA) and then run the experiment at

each allotted slot jet pressure. Data extracted from each experiment is analyzed using Microsoft

Excel and Matlab. The focus of these experiments is to quantify the turbulent momentum mixing

which leads to thrust production. Turbulent flow characteristics are presented here in the results

section; one dimensional aspects from the Pitot testing and two dimensional aspects from the PIV

testing with the associated velocity and uncertainty profiles provided in the Appendix A-D. A

discussion on common trends and the driving force of the momentum mixing between the primary

and secondary fluid is provided at the end of this chapter as well.

4.1 Pitot Probe Analysis

Pitot Probe experiments were conducted to analyze one dimensional fluid characteristics in the

experimental setups. Angle of attack, separation distance, and jet velocities are the three

independent variables tested in these experiments outlined in Table 3.1 above. The velocity

profiles exiting the airfoils is developed using the pressure measurements taken downstream and

converted to velocity measurements using Equation 12 in Chapter 3. Pitot probes take pressure

readings which are then converted to velocities according to Equation 12, and so when referring

to different slot jet runs pressure and velocity will be used interchangeably in the analysis. The

velocity profiles developed are presented in Appendix A of the paper. A discussion on transverse

velocity deficits, tabulated thrust calculations and experimental uncertainty will be given as well at the end of this section.

4.1.1 2-inch Confinement

Higher peak velocities coincide with the higher slot jet velocities as is expected. The two major peaks in each velocity profile are the jet velocities which are seen to stay close to the airfoil bodies. This could mean flow reattachment and coanda effects occurred leading to a loss of thrust. The highest peak velocity of 26.02 m/s occurs during the 25 PSI jet velocity run with no angle of attack. The velocities seen between the jet velocity peaks is the mean mass flow that has developed at the centerline of the system due to momentum mixing upstream. The velocity profiles of each run for the -5AOA 2-inch confinement setup exhibits the smallest velocity differences between jet max velocities and centerline velocities; each at about 17.9, 15.5, and 14 m/s for the 25, 20, and 15 PSI runs respectively. Negating upstream input to the assemblies, thrust can be calculated using Equation 10 and some trends can be analyzed. The greatest thrust over any run is generated during the 25PSI 0AOA run and lowest occurs during the +5AOA 15PSI run. In general, thrust is seen to be greatest for the 0AOA setups from the high velocities leaving the system; but mass flow into the system is expected to drastically effect this and is analyzed during PIV testing.

4.1.2 1.5 Inch Confinement

Higher jet pressure runs correspond to higher velocities in the flow as is expected. The highest velocity recorded is during the 25 PSI run with zero angle of attack; with the velocity being 22.8 m/s. The highest centerline fluid velocity can be seen in each run for the 5-degree inward angle of attack setup. The jet velocity peaks stayed close to the boundaries during each experiment on the 1.5 in. experimental setups as was seen for the 2-inch setups as well, which could indicate some

loses in thrust from reattachment or coanda effects in the flow of the system. The smallest velocity differences occurred in the 5-degree inward runs equaling to 14.7, 12.9, and 10.8 m/s for the 25, 20, and 15 PSI run respectively. Calculated thrust is seen to be greatest for the 25PSI 0AOA experimental run, and lowest for the 15PSI -5AOA setup. The lowest thrust run has changed from the +5AOA setup to the -5AOA setup when moving from 2 to 1.5 inch confinement indicating some boundary effects have become prominent. This again is believed to stem from the high velocities leaving the system but input flows into the system are not quantified and will change the thrust calculations drastically.

4.1.3 1 Inch Confinement

It is seen that the highest velocities are during the runs with the highest slot jet velocities; the highest velocity of 23.9 m/s occurring during the 0AOA 25 PSI run. The highest velocities have been seen to occur for the 0AOA setups for each different airfoil separation distance. The velocity peaks corresponding to the jet velocities stay close to the flow boundaries indicating reattachment or coanda effects could be present in the flow, which has been seen in every assembly. The highest averaged centerline velocity occurred during the zero angle of attack setup at each slot jet velocity. The smallest velocity differences occurred during the setup with zero angle of attack for each run; the differences equaling to 16.8, 16.1, and 13.2 m/s for the 25, 20, and 15 PSI runs respectively. The highest centerline velocities are seen to leave the assembly for the 0AOA assemblies which also produce the highest thrust coming from the high velocities leaving the system.

4.1.4 Discussion of Pitot Probe Testing

Jet pressure converted to velocity was the parameter tested during this experiment. It is seen by looking at the velocity profiles in Appendix A that the highest slot jet exit velocities lead to the

higher velocity readings leaving the airfoils which is expected. The profiles exiting the airfoils from different slot jet velocities are all similar in structure; all the profiles show jet peaks and average mass flow at the centerline of the assembly. The major difference in the profiles is the velocity magnitudes seen. One can think of momentum as a defined quantity entering the system through the slot jet fluid, the conservation equations and RANS equations govern its distribution and convection through the assemblies. Greater amounts of fluid picking up the higher momentum entering the system is desired. The system centerline is furthest from the slot jets and dual jet interactions pull the jet flows towards this area. Therefor the fluid at the center is the last to pick up any of the momentum energy that can make it to the center. That is why fluid velocities at the center of the assembly leaving the airfoils gives some indication of momentum mixing effectiveness upstream.

Higher slot jet runs are seen to develop lower centerline velocities leaving the system which indicates lower momentum mixing. Therefor the differences (or deficits) that develop between max jet flow velocities and centerline velocities in transverse velocity profiles can give some indication to the momentum mixing in the system. As such, Figure 4.1 is presented below showing the velocity deficits seen between the velocity peaks and centralized velocities for each setup:
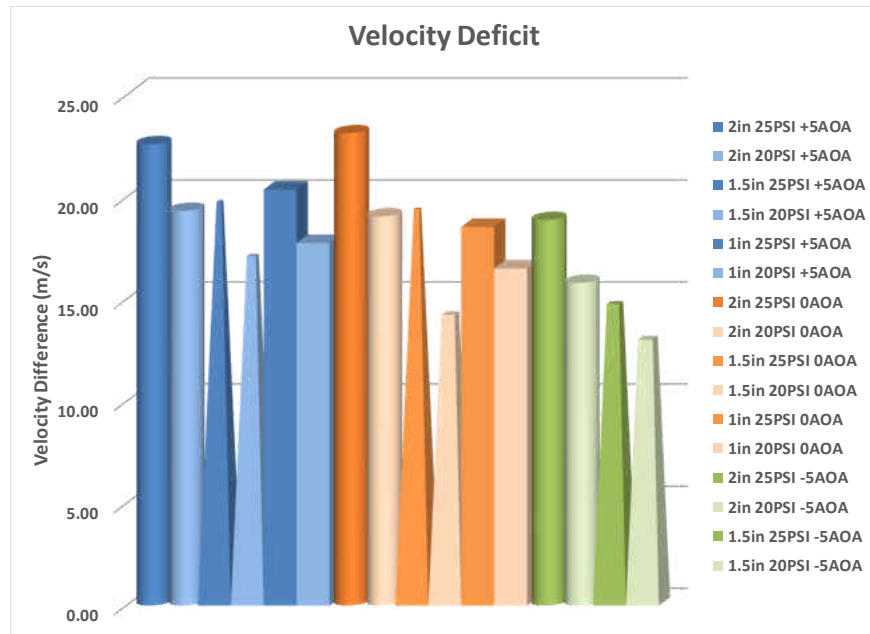
Figure 4.1 Velocity differences between peak velocity and centralized mean velocity of each experimental setup

Figure 4.1 above shows the trends of velocity deficits seen in the transverse profiles developed from the pitot probe testing. The cylindrical shapes show the 2 inch setup, pyramid shape shows the 1.5 inch setups, and the rectangular prism shapes show the 1inch setups. The major trend seen above is that as the airfoils change angle moving from outward to inward, the velocity deficit diminishes. Also, the second major trend shows that as the airfoil spacing diminishes and the airfoils are brought closer together, the deficit diminishes. Angling the airfoils inward restricts the cross sectional area of the flow and Bernoulli's theorem states that this will affect the pressures seen in the system. Bringing the airfoils closer also leads to a cross sectional restriction in the flow which would again affect the pressures in the flow. So, looking at the momentum conservation equations and Bernoulli's theorem, it becomes evident that body forces and pressure play key roles in the momentum dissipation through the system.

To further analyze the information extracted from the pitot probe testing, mass flow into the system is negated and thrust is calculated using Equation 10. As a comparison between the velocity deficits and calculated thrust, Figure 4.2 is presented below:
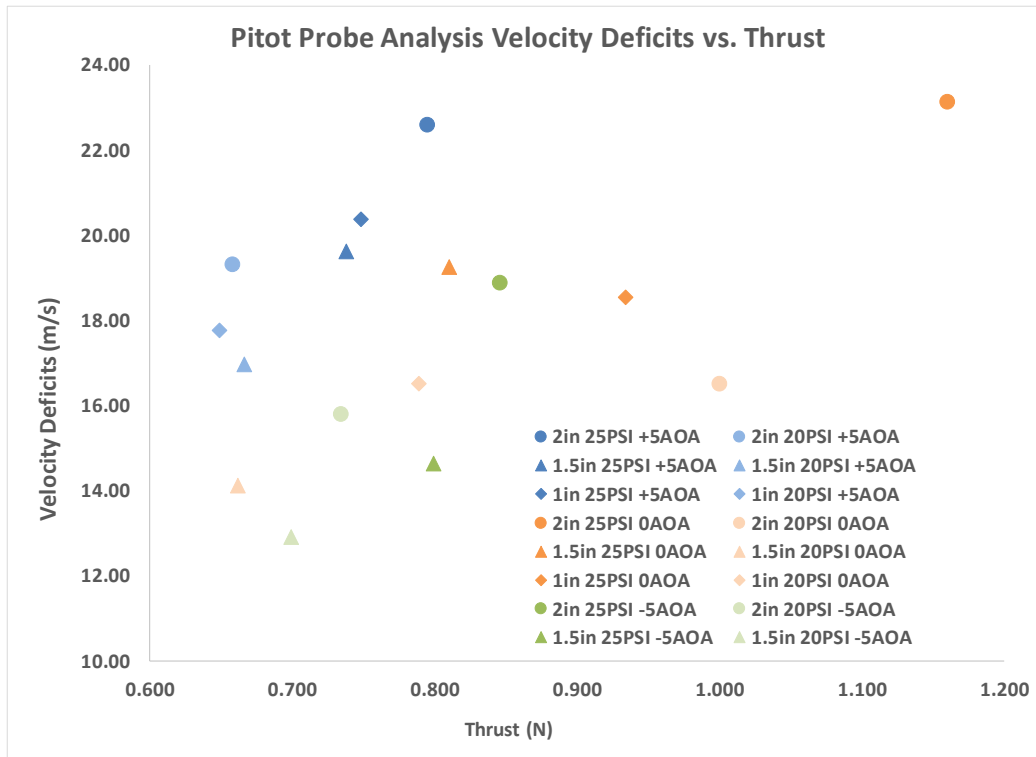
Figure 4.2 Velocity deficits vs Thrust calculated from pitot probe sensor for every experimental assembly

Figure 4.2 above shows the velocity deficits in the transverse direction of the flow leaving the airfoil assembly compared to the associated thrust generated. Higher slot jet velocities show higher thrust generation which is expected. The highest thrust at high speed slot jet runs is seen to occur during the 2in 0AOA setup and at low speed slot jet runs it develops during the 2in 0AOA setup. This indicates that the high velocities leaving the assembly during the 0AOA setups creates the largest thrust, with less mixing upstream then the -5AOA setups but more upstream mixing then the +5AOA setups seen from the velocity deficits.

The scatter of the points, or the differences in thrust and deficits between each slot jet speed runs of the respective assembly can give some information on the system. If the system develops high thrust only when the airfoils are run at high speeds, then there is a low working range for the assembly. The 0AOA setup is seen to have the greatest scatter in Figure 4.2 above indicating that at low speed runs the assembly develops very low thrust compared to the +5 or -5AOA setups. Both the angled assemblies exhibit minimal scatter and lower thrust then the 0AOA setups, but the -5AOA setup has the lowest deficit overall. This indication of high mixing is believed to be driven by something else then turbulent mixing; further analysis will be done with the PIV information.

4.1.5 Pitot Probe Uncertainty Propagation

Manometer readings carry some uncertainty stemming from a multitude of reasons ranging from alignment issues to rounding errors in the pressure readings. Some of these issues are amplified depending on flow conditions but validity of the experimental results require some knowledge of the related uncertainty [45]. As an example, using Equation 10 to convert pressure to velocity; a reading of .01 inches of water pressure translates to a velocity of 2.04 m/s while a reading of .02 inches of water translates to 2.88 m/s. And then looking at higher pressures; a reading of 1.15 inches of water pressure translates to 21.85 m/s while a reading of 1.28 inches of water translates to 23.06 m/s. It is seen that the pressure-velocity relationship is nonlinear creating the necessity to analyze the uncertainty, or error, of the experiment. The only error believed to be affecting this experiment is the calibration error from the manometer readings. Information for the 1 inch -5AOA setups were not recorded and as such all the 1 inch setups were negated in this analysis.

Error propagation stems from different sources in the experimental process and the main one accounted for here is the calibration error specified by the manufacturer of the manometer as .3%.

Three different pressure readings were taken at each point to minimize error using the manometer and so error from alignment or fluid density is believed to be minimal in this analysis. Looking at Bernoulli's equation and the velocity equation given in Equation 10 in the previous chapters, velocity was derived from the pressure readings of the experiment. Uncertainty propagates from these measurements through the calculations and is accounted for using the following equation seen in Equation 13 below [46]:

$$u_r = \sqrt{\sum \left(u_{x_i} \frac{dR}{dx_i} \right)^2}$$

(13)

Where u_r is the expected uncertainty, u_{x_i} is the uncertainty from each measured quantity, R is a function of the measured quantity and x_i is a measured quantity. This is known as the root of the sum of squares uncertainty due to the mathematical setup and will be used to see how measurement uncertainty effects the velocity data. The equation for velocity is seen in Equation 10 in the previous chapters and the uncertainty from the pressure measurement is set at .003. Assuming an unbiased experiment, and one source of uncertainty the following tables are calculated accounting for the max uncertainty seen for each experimental setup with 95% confidence :

Table 4.1 Max Uncertainty propagated from measurement uncertainty for each experimental setup run at 25PSI

25PSI Slot Jet Pressure Runs (95% Confidence)			
2in +5AOA 25PSI	0.00134	1.5in +5AOA 25PSI	0.00134
2in 0AOA 25PSI	0.00113	1.5in 0AOA 25PSI	0.00102
2in -5AOA 25PSI	0.00102	1.5in -5AOA 25PSI	0.00076

Table 4.2 Max Uncertainty propagated from measurement uncertainty for each experimental setup run at 20PSI

20PSI Slot Jet Pressure Runs (95% Confidence)			
2in +5AOA 20PSI	0.00134	1.5in +5AOA 20PSI	0.00134
2in 0AOA 20PSI	0.00113	1.5in 0AOA 20PSI	0.00102
2in -5AOA 20PSI	0.00102	1.5in -5AOA 20PSI	0.00080

Max experimental uncertainty of .00134 is seen in Tables 4.1 and 4.2 above for each slot jet speed run. As the airfoils are altered from being angled out to in, uncertainty is seen to diminish. It can also be seen that as confinement spacing between the airfoils diminishes uncertainty also diminishes. Velocity profiles with error bars of the above uncertainty calculations multiplied by a constant to help with the visualization are found in Appendix B as well. It can be seen in the profiles that uncertainty is largest in the center of the system and that slot jet speeds do not affect the uncertainty magnitudes substantially. Examining the tables above uncertainty in the system is seen to not exceed 1% which indicates that with 95% certainty, the data extracted is credible with less than 1% fluctuation which amounts to less than 1 m/s.

Further uncertainty analysis was performed to look at the confidence intervals of the data. Looking at 95% confidence intervals for the sample mean and variance important data validation regarding bias of the information can be seen. Calculations were conducted following a process outlined by Bendat [47]. Below in Tables 4.3-4.6 can be seen the calculated mean, variance, and 95% confidence intervals for each experimental assembly:

Table 4.3 Sample mean, variance and 95% Confidence intervals for the 2 inch setups run at 25PSI

2in +5AOA 25PSI		
Lower Confidence Interval	Mean Vel.	Upper Confidence Interval
4.064	7.450	16.707
	Variance	
37.810	76.251	126.654
2in 0AOA 25PSI		
Lower Confidence Interval	Mean Vel.	Upper Confidence Interval
9.831	13.269	16.707
	Variance	
37.810	63.212	126.654
2in -5AOA 25PSI		
Lower Confidence Interval	Mean Vel.	Upper Confidence Interval
9.180	12.340	15.500
	Variance	
34.327	49.349	137.080

Table 4.4 Sample mean, variance and 95% Confidence intervals for the 2 inch setups run at 20PSI

2in +5AOA 20PSI		
Lower Confidence Interval	Mean Vel.	Upper Confidence Interval
2.797	6.165	9.533
	Variance	
26.194	56.566	77.647
2in 0AOA 20PSI		
Lower Confidence Interval	Mean Vel.	Upper Confidence Interval
8.127	11.406	14.686
	Variance	
20.805	45.011	69.690
2in -5AOA 20PSI		
Lower Confidence Interval	Mean Vel.	Upper Confidence Interval
7.569	10.703	13.837
	Variance	
17.537	35.296	70.032

Table 4.5 Sample mean, variance and 95% Confidence intervals for the 1.5 inch setups run at 20PSI

1.5in +5AOA 25PSI		
Lower Confidence Interval	Mean Vel.	Upper Confidence Interval
5.096	8.426	11.756
	Variance	
21.446	46.398	71.837
1.5in 0AOA 25PSI		
Lower Confidence Interval	Mean Vel.	Upper Confidence Interval
7.011	11.808	16.604
	Variance	
12.471	56.849	75.197
1.5in -5AOA 25PSI		
Lower Confidence Interval	Mean Vel.	Upper Confidence Interval
11.675	14.977	18.279
	Variance	
12.471	28.049	61.585

Table 4.6 Sample mean, variance and 95% Confidence intervals for the 1.5 inch setups run at 20PSI

| 1.5in +5AOA 20PSI		
Lower Confidence Interval	Mean Vel.	Upper Confidence Interval
4.706	7.598	10.489
	Variance	
16.168	34.981	54.159
1.5in 0AOA 20PSI		
Lower Confidence Interval	Mean Vel.	Upper Confidence Interval
6.156	9.649	13.143
	Variance	
9.989	30.157	39.890
1.5in -5AOA 20PSI		
Lower Confidence Interval	Mean Vel.	Upper Confidence Interval
10.135	13.112	16.090
	Variance	
10.138	22.802	50.065

These confidence intervals state that the data points collected will be within the above intervals with a 95% certainty [47]. Comparing these intervals with the data points in the profiles seen in Appendix A and B, some velocity points fall above and below the intervals of the sample mean.

This indicates some uncertainty does follow the measurements which was evaluated in Tables 4.1 and 4.2. But no real trend is seen to develop regarding points that fall above and below these intervals indicating minimal bias in the information which validates the computed error in Tables 4.1 and 4.2. But in general, between both uncertainty evaluations, the trends seen are that decreasing the airfoil cross sectional spacing and through confinement or angling decreases the associated error of the measurements.

<div align="center">4.2 PIV Flowfield Analysis:</div>

Pitot Probe analysis extracts important one-dimensional information of the flow but does not account for input into the system or provide enough information to fully characterize the two-dimensional flow components. Particle Image Velocimetry (PIV) analysis extracts two-dimensional flow information and input components of the system leading to a more accurate fluid dynamics analysis of the proposed propulsion system. As described in the experimental setup chapter, airfoil configurations with 1-inch confinement and .5-inch confinement spacing are analyzed. For each airfoil assembly the airfoils are set at three different angles; 5 degrees inwards (-5AOA), 0 degrees (0AOA), and 5 degrees outward (+5AOA). For each angled setup the experiments are run at two different jet flow velocities before the test setup is reassembled. In order to get precise flow information, the airfoil assembly was broken into 2 test sections corresponding to the Mid-Section (Slot jet exit location) and Bottom-Section (downstream or tail end). All information obtained in the experiment was compiled and processed using MATLAB, Microsoft Excel and the PIVlab MATLAB Toolset [48]. Below in Figure 4.3 can be seen an example of the type of data extracted from the midsection of the airfoil assembly. It is pictures like

that in Figure 4.3 that is used in the PIVlab software to analyze fluidic characteristics and from which important two-dimensional flow information is extracted:
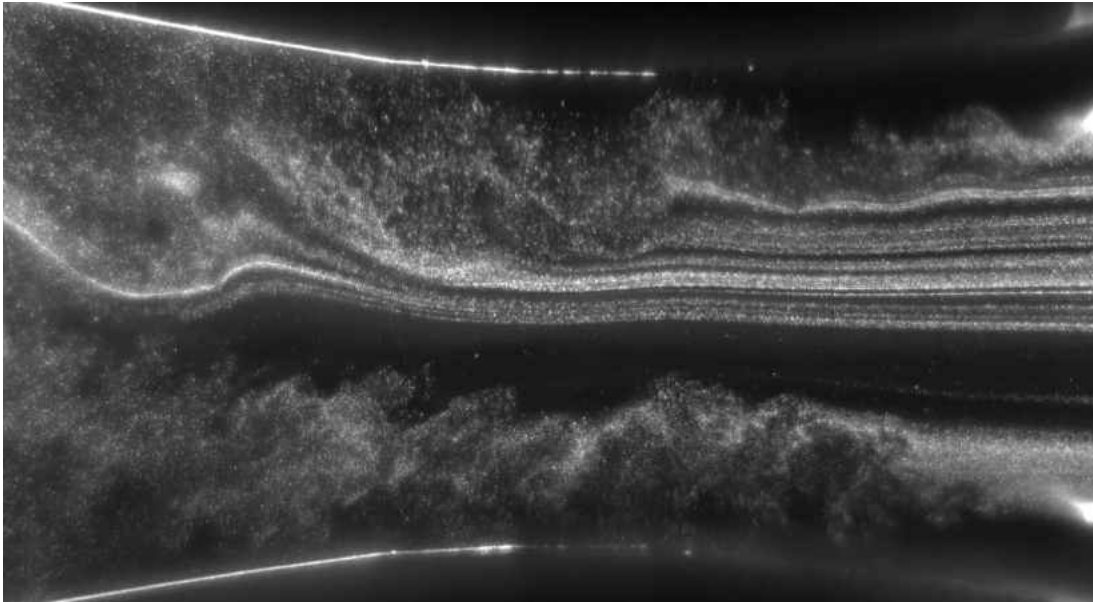
Figure 4.3 Mid-Section Airfoil Flow assembly

The slot jets were not seeded during the experiment so velocities exiting the slot jets, and potential core information were not well quantified in the data collected. Similarly, in the control volume analysis section the inlet boundary of the system only accounts for the entrainment flows entering the system and not slot jet flows. Velocity, Confinement Spacing, and Angle of attack are the three independent variables tested during the experiment and as such each variables effect on the flow will be analyzed and discussed after presenting the results.

The general velocity fields of each assembly are given in the Appendix C and D. Information from one of the slot jets is analyzed here and is assumed to be the same for the second slot jet due to the symmetrical alignment of the system and low bias seen in the pitot testing section. This section begins with a control volume analysis on the mass flow in and out of the system. After, turbulent

quantities known as halfwidth thickness, shear layer thickness, nondimensionalized turbulence intensity (Urms), and Reynold shear stress profiles are presented. This is followed by a discussion of the effects each independent variable has on the turbulent quantities and how that relates to thrust production. Afterwards, tabulated thrust and thrust augmentation ratios are presented followed by an optimal setup presented and then a discussion on the driving force of the momentum mixing in the system.

4.2.1 Control Volume Analysis

Looking at the thrust equation seen in Equation 10, mass flow is seen to play a direct role in thrust production. Creating a control volume around the system and looking at the mass that comes in and out helps see how the slot jets influence mass flux in the system. Analyzing Figure 4.3 above flow is seen to move from right to left and that the slot jets were not seeded in this experiment. Setting the control volume boundary far to the right of the photo seen in Figure 4.3 above, and the other boundary at the outlet of the bottom section photos seen in the appendix; inlet flow and outlet flow information is obtained. The slot jets are not seeded and so the inlet control volume boundary does not mix the slot jet and inlet flows. Velocity contours for each experimental assembly are given in Appendix C below as reference.

Each slot jet is assumed to act like a free turbulent shear jet flow as described in the literature review section. Using Equations 1-3 in the literature review chapter, general system parameters are seen to affect momentum dissipation in different ways. Looking at the continuity equation the angle of the exiting slot jets to the airfoil body, the area of the slot jet exit, boundary effects of the airfoil body, and the mixing layer propagation are key factors in the development of the mass flow through the system. Looking at the momentum conservation equation it is seen that increasing jet

50

velocity spread (momentum diffusion), increasing secondary velocities from the quiescent fluid, and decreasing frictional drag effects from the airfoil body have significant effects on the momentum spreading in the flow of the system which directly effects thrust production. It was established that jet velocity, angle of attack, and confinement effects are key components to the development of the flow field in the system which are also the three independent variables tested in this experiment.

As the flow is moving downstream, dual jet interactions start to become prevalent as shown in Figure 2.4. Looking at Figure 2.4, different dual jet regions of the flow can be seen to affect the velocity profiles in the flow field in different ways. The upstream region where negative pressures develop in plane dual jet flow fields is believed to be where entrainment occurs and pulls extra mass into the system from the opening between the slot jets. The merging region (area between the merge and combined point in Figure 2.4) is seen to be where most of the momentum mixing occurs. It is in this region that the analyzed system of this paper should remain the longest as this would induce the greatest amount of momentum mixing. The combined flow region shows the highest velocity peaks, but also separation from the airfoil leading to increases in adverse pressure gradients along the bodies. Bringing in the most amount of fluid and pushing as much of the high momentum energy to as much of the increased mass flow of the system (highest bulk fluid flow) are the main desired criteria pursued to optimize thrust production.

In order to quantify the jet mass flow, an integral sum of the mass flow leaving the airfoils and that entering the airfoil was taken. Assuming what goes out minus what goes in is equal to the amount of mass introduced by the jet, the jet flow is quantified. Figure 4.4 and 4.5 are developed to compare jet flow with output flow and can be seen below:
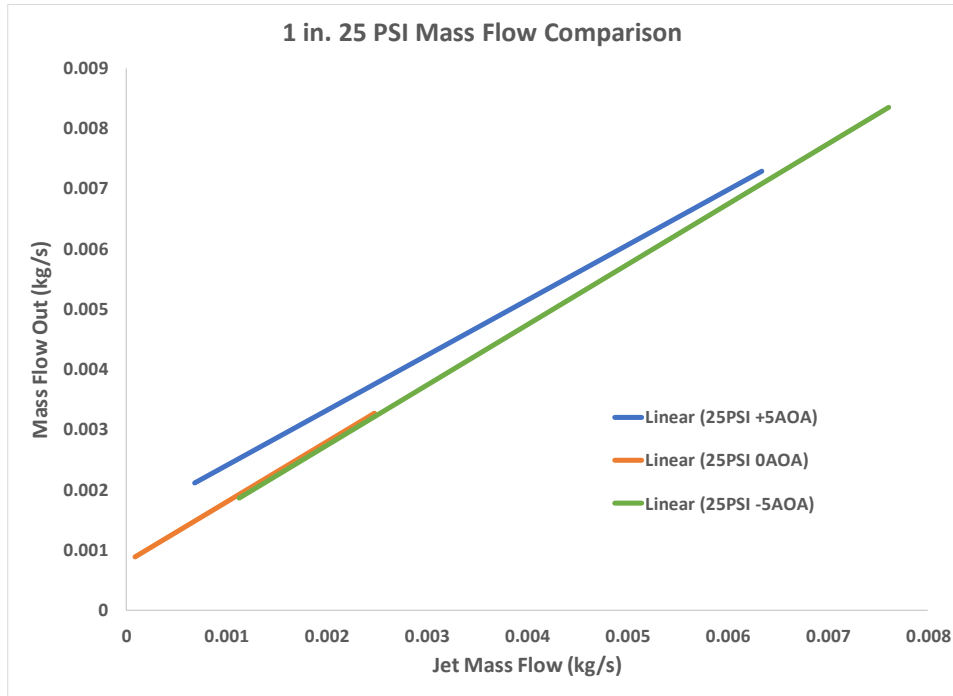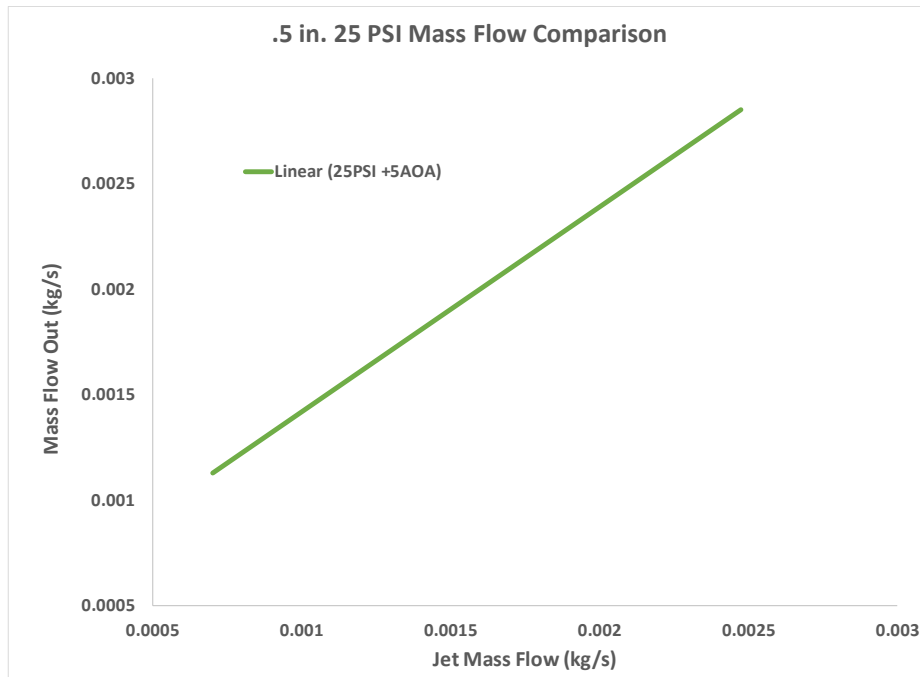
Figure 4.4 Comparison between mass flow coming from the slot jets to mass flow leaving the airfoil assembly for the 1 inch experimental assembly 25 PSI slot jet pressure runs
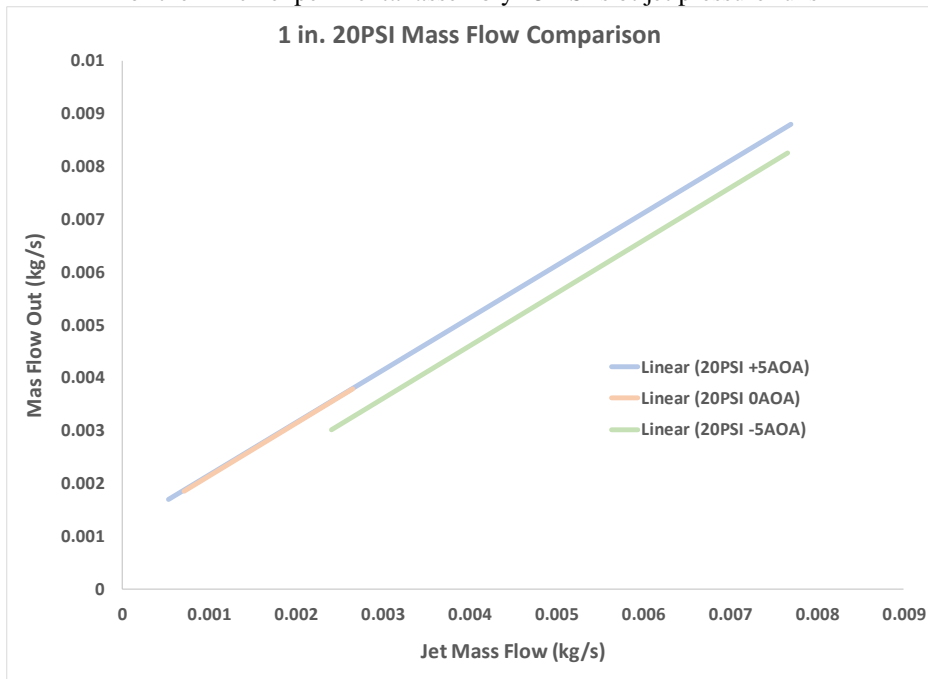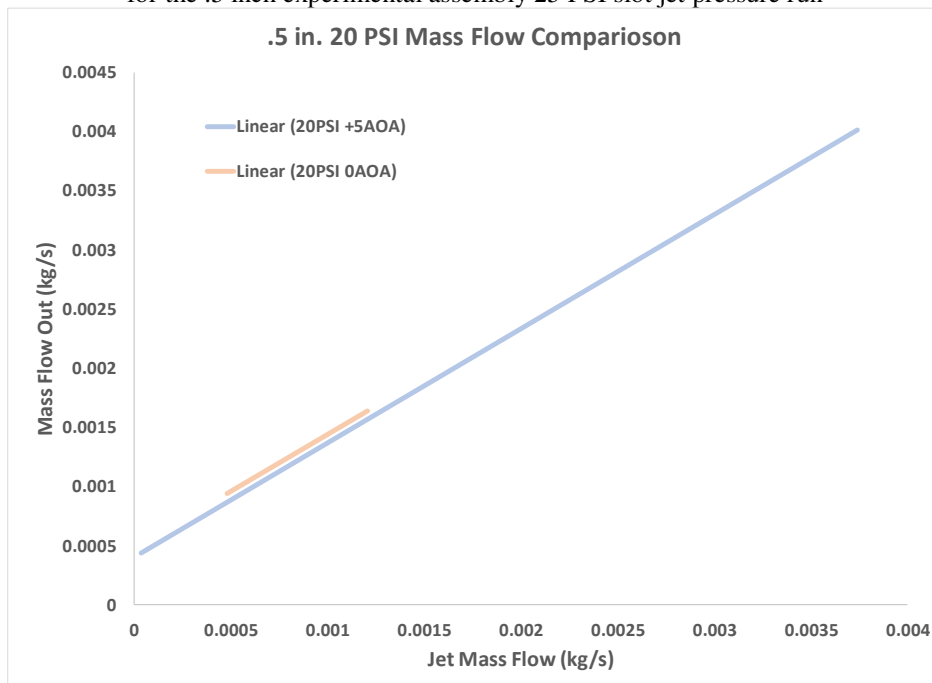

Figure 4.5 Comparison between mass flow coming from the slot jets to mass flow leaving the airfoil assembly for the 1 inch experimental assembly 20 PSI slot jet pressure runs

Below in Figures 4.6 and 4.7 are the same graphs for the .5 in. experimental assemblies, remembering that information from the bottom section for the .5in. +5AOA assembly (output information) and for the .5in. assemblies with airfoils angled inwards (-5AOA) were not recorded:

Figure 4.6 Comparison between mass flow coming from the slot jets to mass flow leaving the airfoil assembly for the .5 inch experimental assembly 25 PSI slot jet pressure run

Figure 4.7 Comparison between mass flow coming from the slot jets to mass flow leaving the airfoil assembly for the .5 inch experimental assembly 20 PSI slot jet pressure runs

Looking at the figures above, the control volume analysis shows a strong linear trend between jet mass flow and mass flow leaving the airfoil assembly as is expected. This tells us that increasing the slot jet velocities will increase velocities leaving the system. Higher mass flow magnitudes are seen for 1 inch separation as compared to .5 inch separation as is expect due to larger cross sections in the flow. The highest mass flows are seen when the airfoils are angled outwards due to the increase in cross sectional area of the system as the fluid leaves the system. Lowest mass flows are seen when the airfoils are not angled indicting minimal flow in or out of the system. The greatest slopes for high speeds slot jet runs are seen when the airfoils are angled inwards, and no real distinctions about the slopes can be made at low speeds. This indicates faster mixing of momentum of the slot jets to the secondary fluid for the -5AOA setups at high speed. To compare the mass flux through the system and thrust which are directly related, Figure 4.8 is shown below which displays the difference between the average mass in and out compared to thrust production:
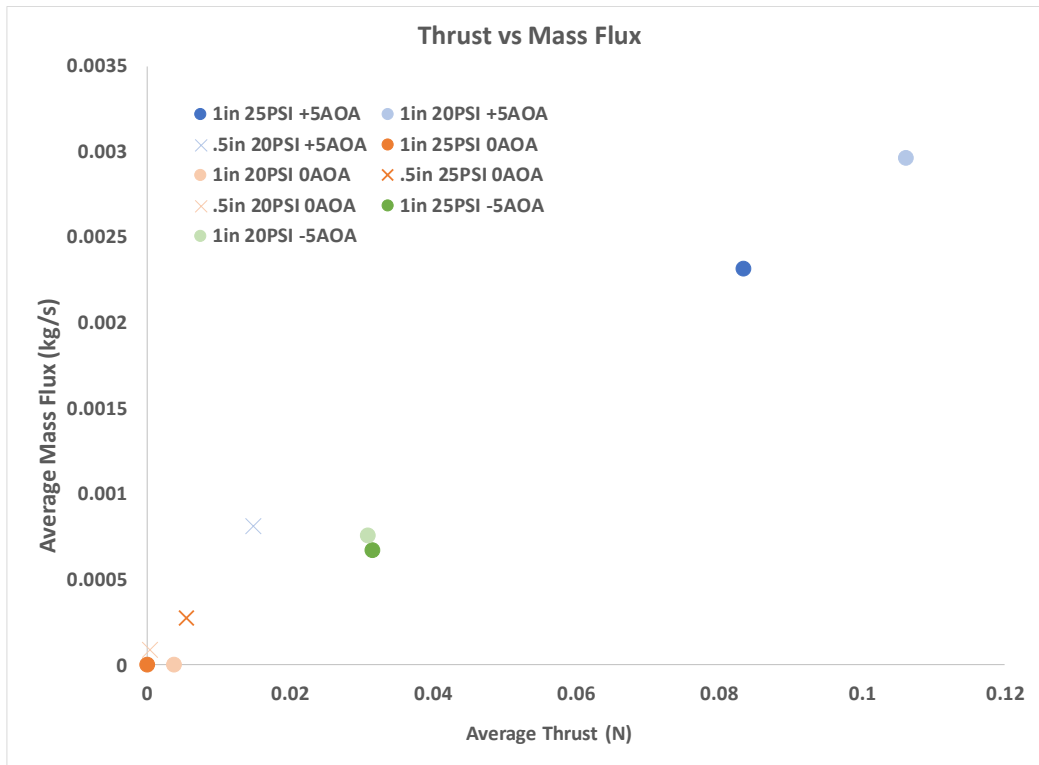
Figure 4.8 Difference between mass in and mass out for each 1 inch test assembly

The figure above shows a direct relation between mass flux through the system to thrust development which validates the assumption that high bulk fluid movement which correlates to high mass flux is desired. Mass flow differences through the system are the highest at low speed slot jet runs. It can also be seen that the highest mass flow differences, indicating minimal mass input, comes when the airfoils are angled outwards followed by the -5 and then 0AOA setups. Higher confinement spacing is also seen to have higher mass flux coming from the larger cross sectional area. Angling the airfoils shows a direct increase in the momentum mixing of the system, but the +5AOA setups show highest bulk movement from the slot jet momentum which develops the greatest thrust as well.

4.2.2 1-inch Separation

The first experimental configuration analyzed is the assemblies with the airfoils set 1 inch apart (or 1-inch confinement space) and at +5,0, and -5 AOA. For each setup the experiments were run two times, at 25 and 20 PSI slot jet pressures and the data recorded. Using Reynolds decomposition, Reynolds averaged Navier Stokes equations, and gradient calculations as described in chapter 3; turbulent flow quantities known as jet halfwidth propagation, shear layer propagation, turbulent intensities, and Reynolds stress profiles for every 1 inch test assembly is presented here.

4.2.2.1 Jet Halfwidth Propagation

The high momentum energy entering the system from the jets gets dispersed into the slow-moving air in between the airfoils. This creates velocity profiles that start with high peaks and velocity deficits between the slow moving and fast moving fluid. But as the fluid moves downstream these peaks and velocity differences start to decline and the profiles start to become flatter and wider downstream as compared to skinny and tall upstream. The physical meaning of this is that the high velocity jet flow is mixing its momentum with the low velocity fluid thus dispersing the momentum energy. A good physical representation of this dispersion is called the jet halfwidth, which is a measure of the distance away from the jet velocity maximum to where the velocity is half the jet maximum. The halfwidth thickness for the 1 inch assemblies can be seen below in Figures 4.9 and 4.10:
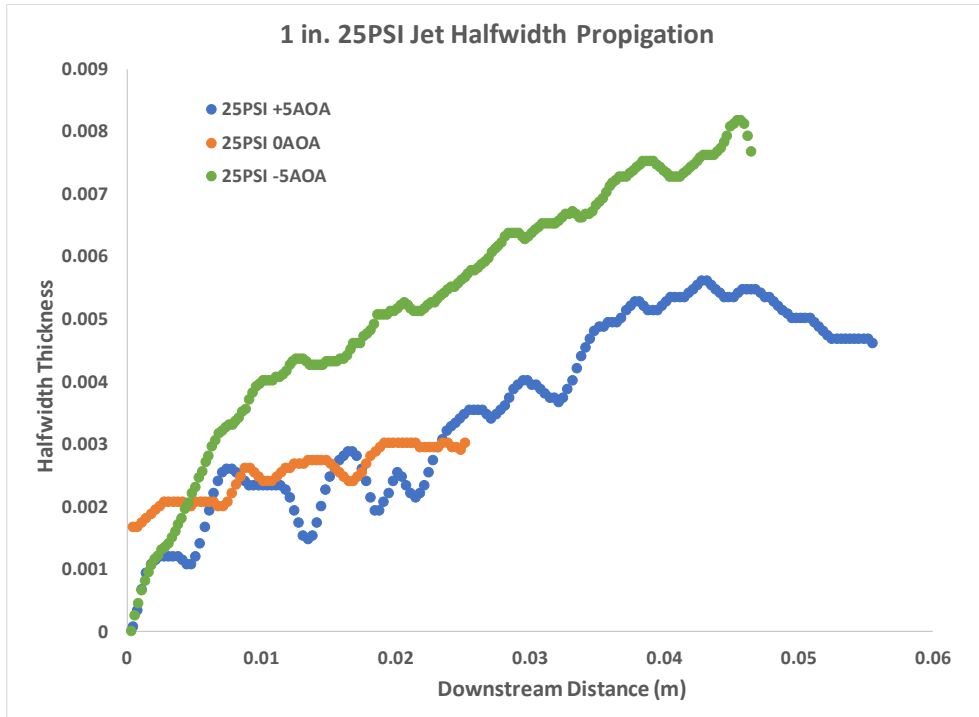
Figure 4.9 Jet halfwidth propagation downstream for the 1 in. assembly run at 20PSI
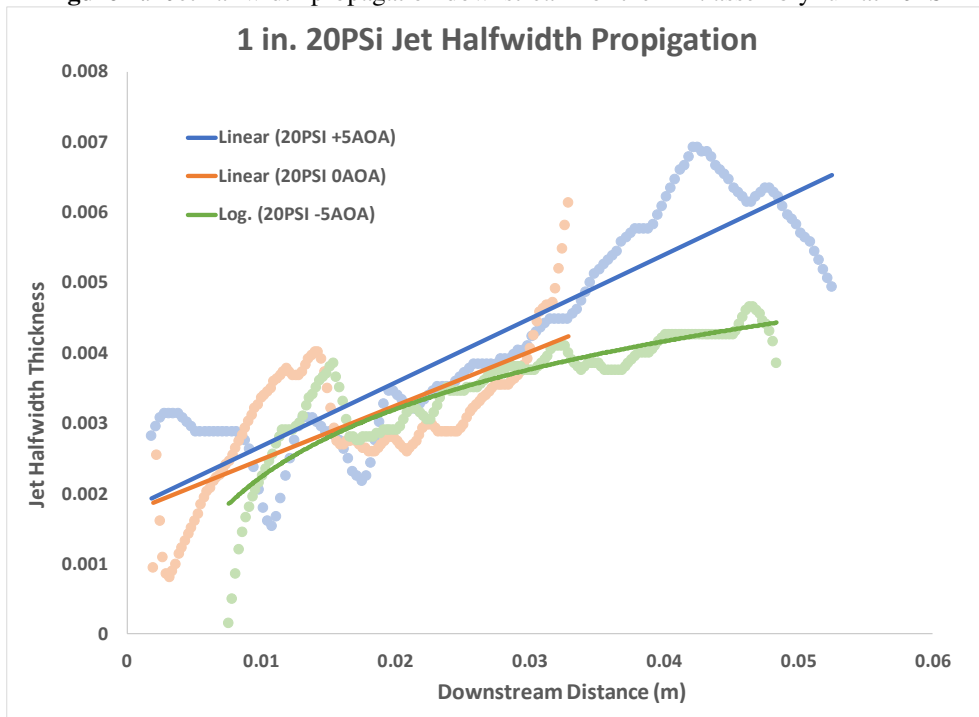

Figure 4.10 Jet halfwidth propagation downstream for the 1 in. assembly run at 25PSI

At higher speeds, the halfwidth for the -5AOA setups is greatest followed by the +5AOA setups. At low speeds, the halfwidth thickness converge and the +5AOA setups becomes thickest downstream. The halfwidth is thickest upstream for the 0AOA setups but quickly converges to that of the other setups indicating high entrainment velocities entering the system for the 0AOA assemblies. Figure 4.11 is overlaid with the trendlines of each data set which is applicable for both slot jet speed runs. The +5AOA and 0AOA setup show strong linear trends indicating they will keep growing further downstream. The -5AOA setup shows a logarithmic trend indicating it will dampen out upstream, but something has caused the high momentum to jump towards the centerline. It is believed that when the airfoils are angled inwards and cross section is constricted, there is bluff body interactions coupled with Bernoulli's theorem regarding pressure gradients causing this steep jump in halfwidth thickness and then the drop off downstream. This would affect the pressure and body forces in the flow which would develop into the driving force behind the momentum dissipation in the system; further discussion of this is given at the end of this chapter.

4.2.2.2 Shear Layer Propagation

As stated in the literature review chapter, shear layers are the area in a free shear flow fluidic system where vorticity is generated, and turbulence is developed. Shear layer thickness measures the size of this layer which indicates turbulence generation; thick shear layers lead to high turbulence, mixing, and entrainment. Below in Figures 4.11 and 4.12 can be seen the shear layer thickness profiles as the fluid moves downstream:
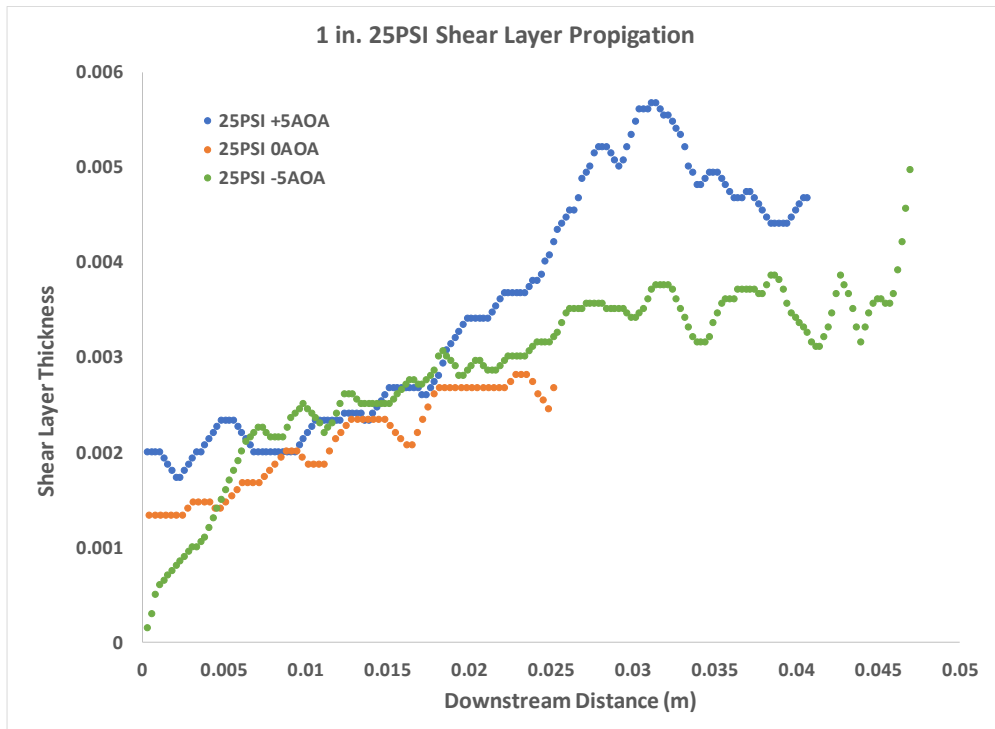
Figure 4.11 Shear layer Thickness propagation for the 1 inch test assembly run at 25PSI
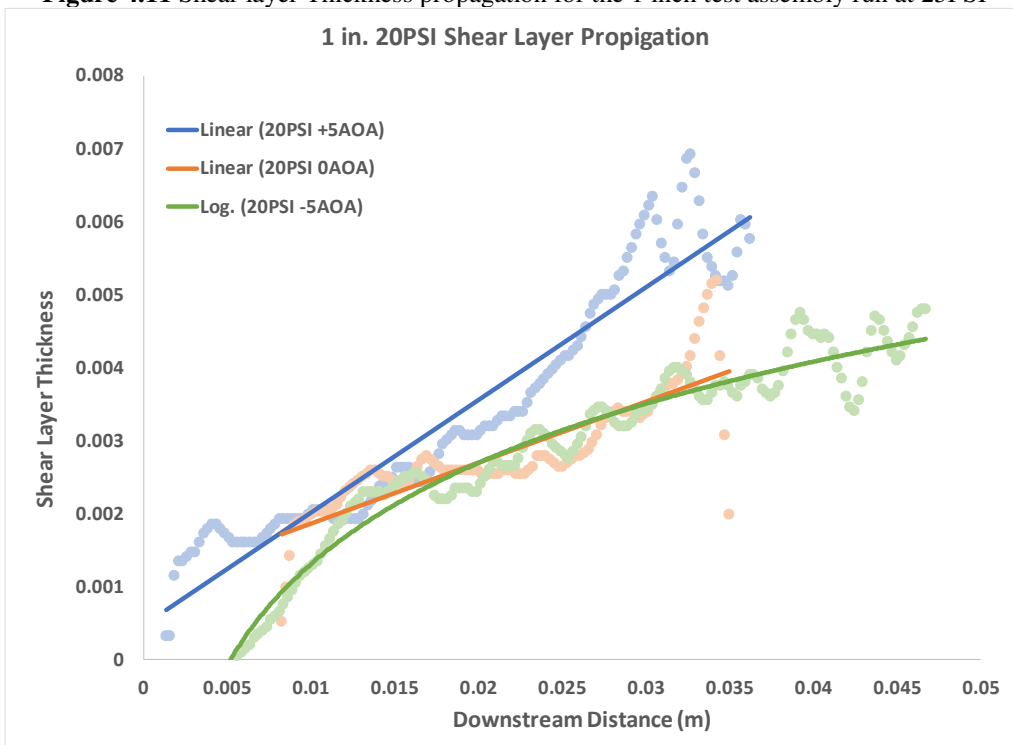
Figure 4.12 Shear layer Thickness propagation for the 1 inch test assembly run at 20PSI

60

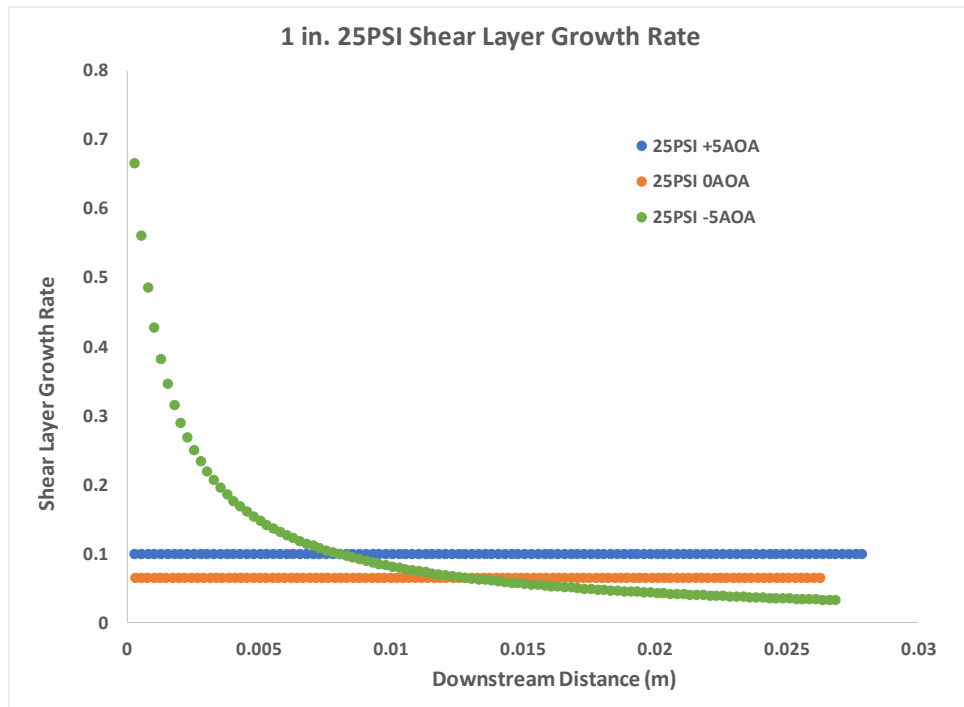Below in Figures 4.13 and 4.14 can be seen the shear layer growth rate for the 25and 20 PSI runs:

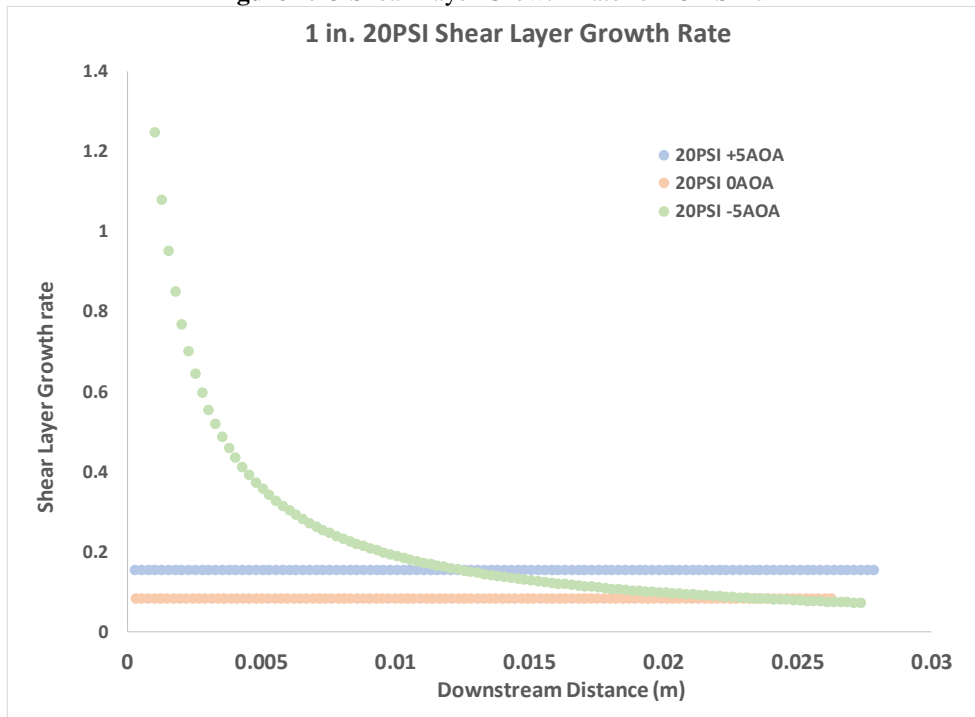

Figure 4.13 Shear Layer Growth Rate for 25 PSI run

Figure 4.14 Shear Layer growth rate for the 20PSI run

61

Figures 4.11 to 4.14 above show the shear layer thickness, and the shear layer growth rates for each experimental run. At both speeds the shear layer is largest for the +5AOA setups downstream. Upstream, the 0AOA trendlines indicate larger shear layers for both jet speed runs indicating some high entrainment flows entering the system. The -5AOA setups shear layer thickness develops furthest downstream but has the highest growth rate upstream. The shear layer profile increases in a logarithmic fashion, so it becomes the thick downstream. This similar growth rate is seen in the halfwidth profiles for the -5AOA setups as well. This indicates fast upstream momentum dissipation from the slot jets which is again believed to come from bluff body and pressure effects which can also choke out entrainment flows coming into the system. The size of the shear layer for each setup begin at different sizes and end at different points in the system, but in the middle of the flow field the shear layers converge at similar point for all angles of the airfoils. The largest growth rate is seen for the -5AOA setups in a logarithmic trend. But this dies downstream where the +5AOA's linear growth rate becomes the largest.

4.2.2.3Turbulent Intensities

Turbulence is quantified using Reynolds decomposition, where the velocity field is broken into two pieces; a time average component and fluctuating component as was discussed in the literature review chapter. The fluctuating components are vector quantities that vary with time and give insight into fluid movement. Finding the Urms values essentially finds the magnitude of the time varying vector quantity and so is a good indicator of turbulence intensity. Magnitudes of the fluctuating components are extracted and nondimensionalized Urms values with mean flow are calculated along the centerline of the system and presented here in Figures 4.15 and 4.16:
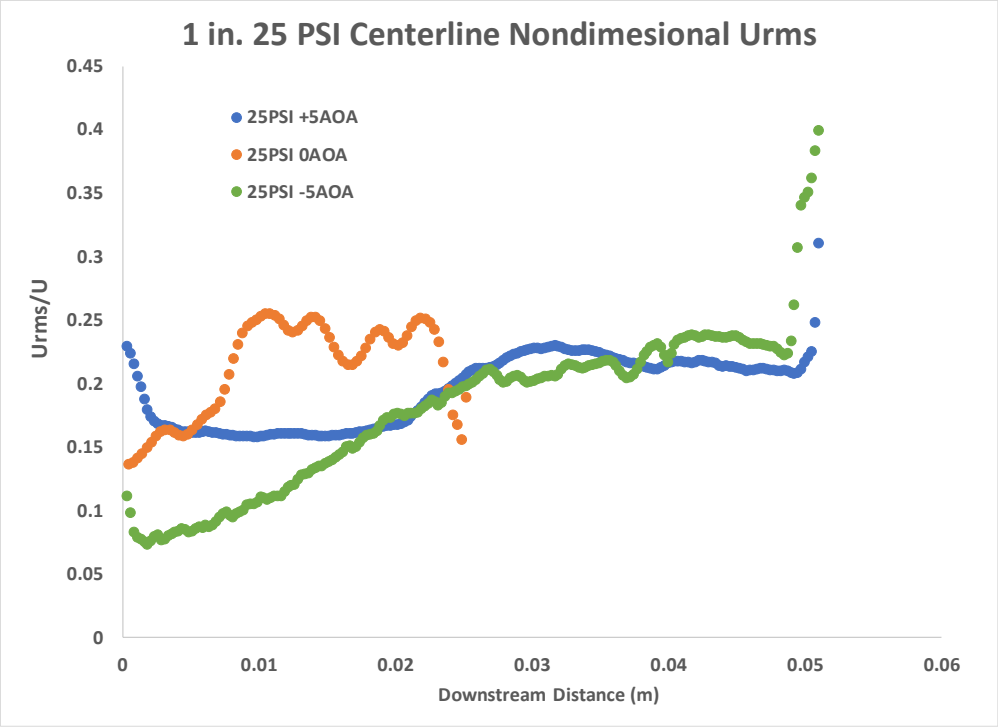
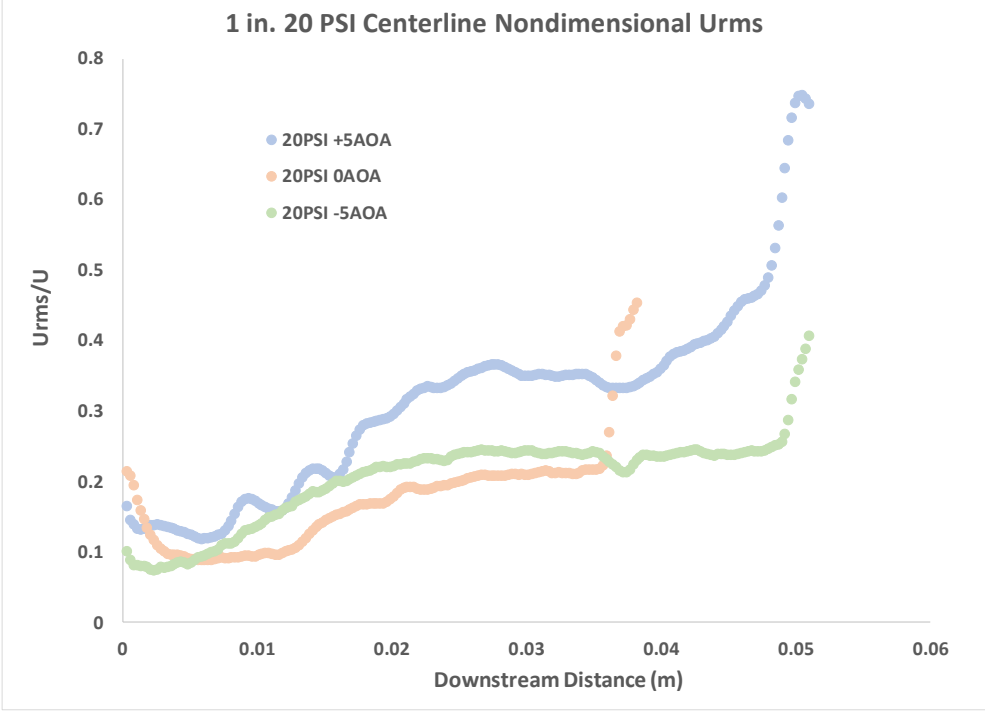**Figure 4.15** Nondimensional Streamwise Urms for the 1 inch test assemblies run at 25PSI


Figure 4.16 Nondimensional Streamwise Urms for the 1 inch test assemblies run at 20PSI

63

Figure 4.15 and 4.16 show the nondimensionalized Urms values at the centerline of the system as the fluid moves downstream. Turbulence seems to increase as the fluid moves downstream which is to be expected. At higher speeds, the highest turbulence is seen in 0AOA setups upstream but as the fluid moves downstream the highest turbulence is seen in both angled setups. At lower speeds' turbulence is highest upstream for the 0AOA setups but moving downstream turbulence grows larger in the +5AOA setup. This validates the earlier statement that high amounts of turbulence and flow are sucked into the system upstream when the airfoils are not angled. For every run turbulence seems to converge mid-way through the mid-section of the system but then disperse further downstream.

To look at boundary layer effects, transverse Urms profiles are developed and seen below in Figures 4.17 and 4.18:
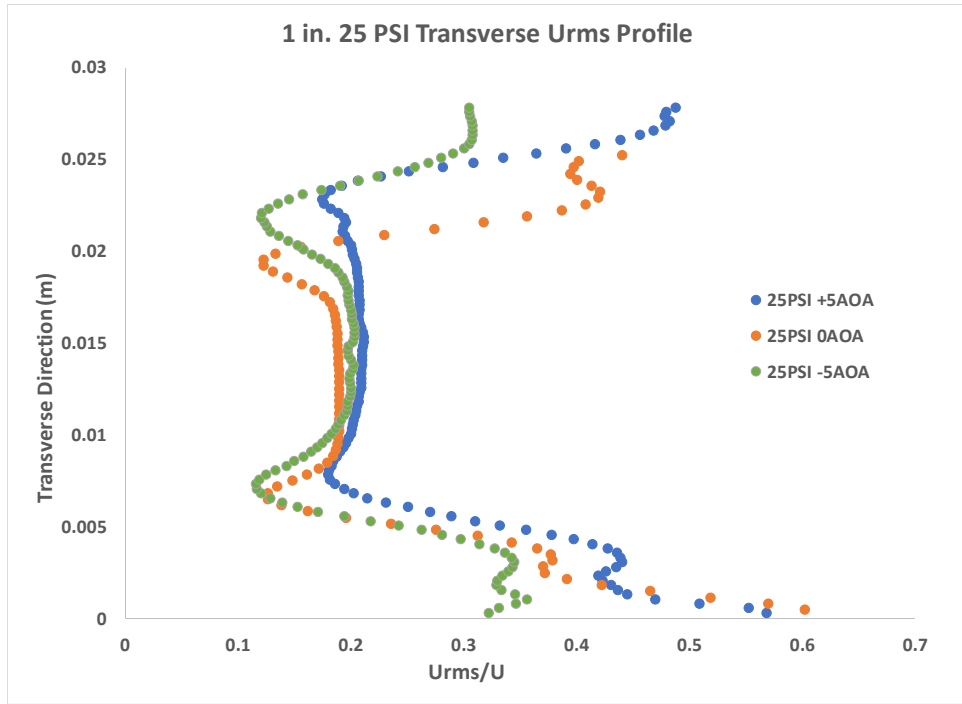
**Figure 4.17** Transverse Urms Profiles for the 1 in. setups run at 25PSI
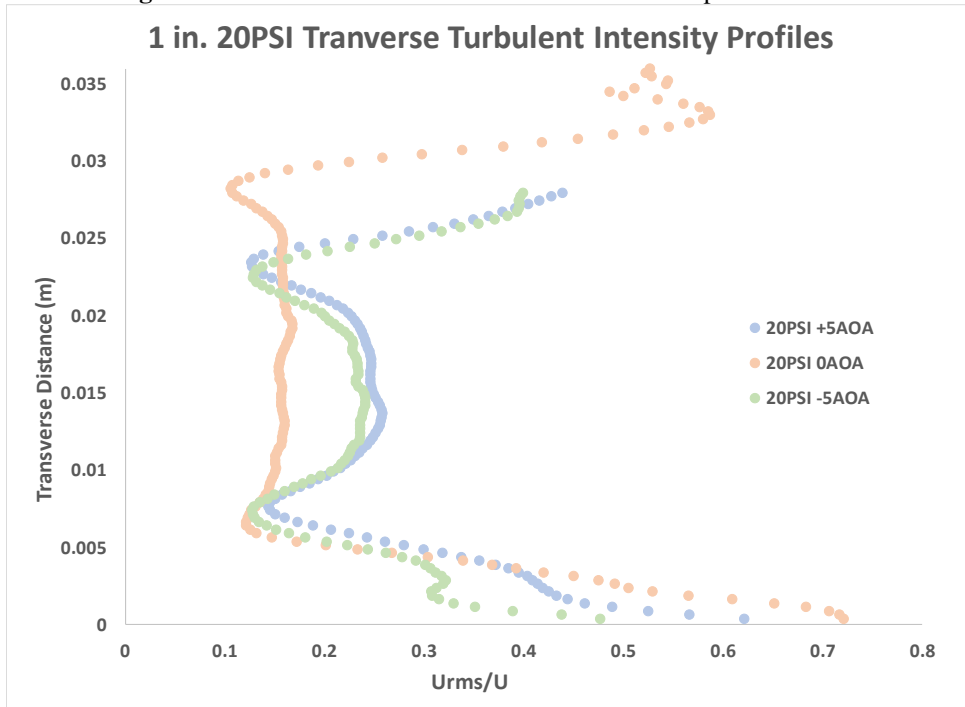
**Figure 4.18** Transverse Urms Profiles for the 1 in. setups run at 20PSI

Looking at the transverse turbulence profiles above in Figures 4.17 and 4.18, it is seen that a base amount of fluid turbulence has developed which is why these profiles do not go down to zero at the centerline. Maximum turbulent peaks are seen close to the boundaries and at the centerline of the system while minimum peaks are seen where the jet velocities are believed to be. Turbulence is generated from vorticity, and vorticity develops according to the vorticity equation seen in Equation 9. According to this equation, vortex roll up occurs in areas of the highest velocity gradients and minimal vorticity develops at jet velocity maximums where there are minimal gradients. Turbulence is greatest at the boundaries for the 0AOA setups and greatest at the centerline for the +5AOA setups. The boundary turbulence is highest due to boundary layers and free shear layers interacting and increasing turbulence. This also leads to recirculation zones developing along the boundary, maximum of which can be seen when the airfoils are not angled. This can explain why the 0AOA setups have the smallest shear layers downstream; they lose their momentum energy to recirculation and adverse pressure gradients close to the boundary.

4.2.2.4 Reynold Shear Stress

Reynold shear is a mathematical term coming from the Reynolds Averaged Navier Stokes equation. It quantifies the turbulent mixing seen in free shear flows and is calculated for this system in the middle of the shear layer right at the slot jet exits where it should be maximum. Below in Figures 4.19 and 4.20 can be seen the Reynold shear magnitudes right where the slot jet enters the system at the center of the shear layer:

66
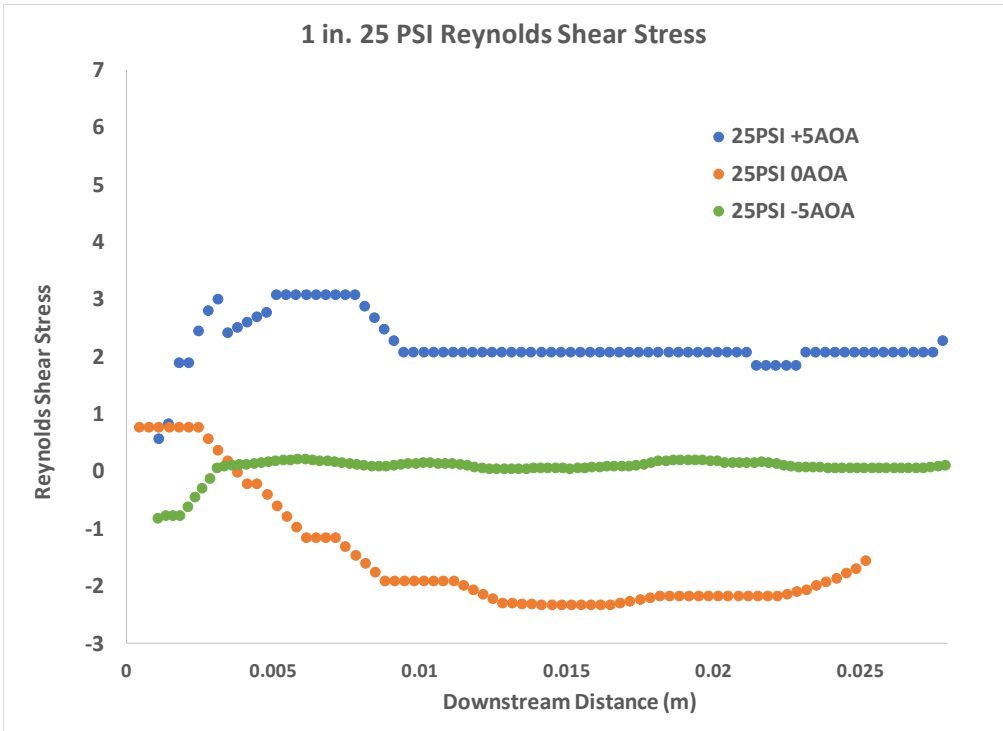
Figure 4.19 Reynold shear stress for the 1 in assembly run at 25PSI
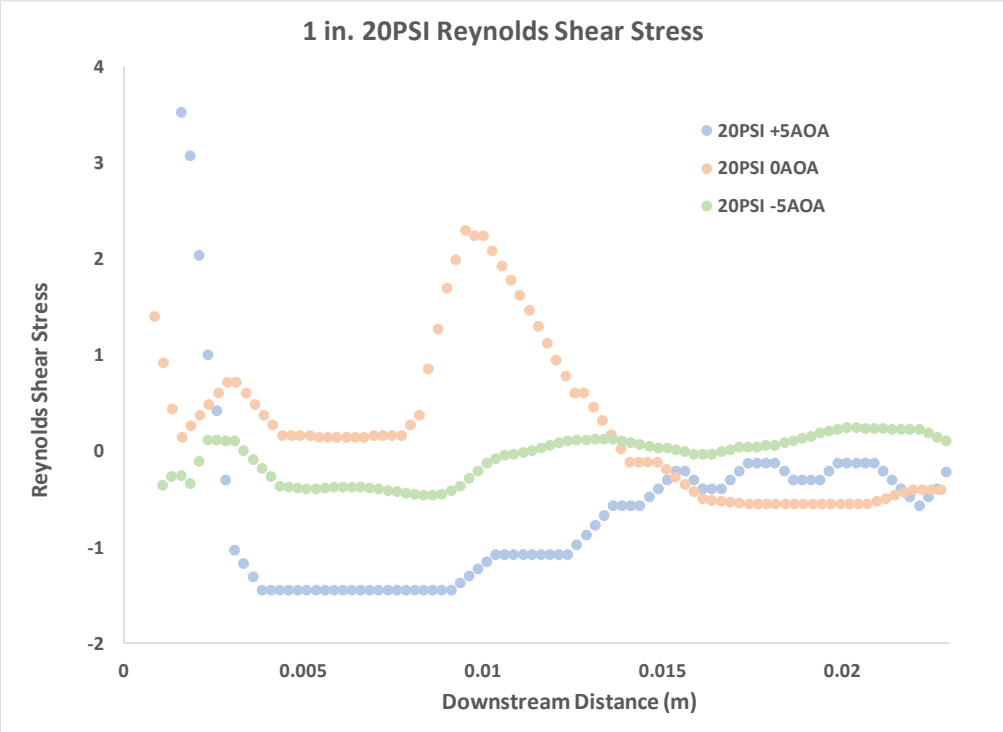
**Figure 4.20** Reynold Shear stress for the 1 inch assembly run at 20PSI

67

Reynold shear stress right at the slot jet exits in the center of the shear layer is shown in Figures 4.19 and 4.20 above. This shear stress is a vector quantity multiplying U and V fluctuations and so the values are dependent on flow direction and magnitude. Higher slot jet speeds produce higher Reynolds stress magnitudes which is expected since there are larger amounts of momentum energy in the system. At high speeds, the largest Reynolds magnitude is seen for the +5AOA setup and lowest is seen for the 0AOA setup. Both profiles become constant a small distance downstream. At low speeds, the 0AOA setups show highest Reynolds upstream and then converge together downstream. The lowest Reynolds seen at low speeds is for the +5AOA setups which then converges towards the other setups downstream. The Reynold stress magnitudes for the -5AOA setups stays constant around 0 indicating limited mixing for each experimental run. This further validates the assumption that other fluid dynamics besides turbulent mixing are driving the high momentum mixing seen for the -5AOA setups.

4.2.3 .5-inch Separation

In this section, data from the experimental setup where the airfoils are separated by .5 an inch will be presented. Information from the mid-section of the +5AOA setups and all the 0AOA information is presented, while information from the bottom section of the +5AOA setups and the -5AOA setups was not recorded.

4.2.3.1 Halfwidth Propagation

As was stated earlier, the halfwidth of the jet flow is where velocity is half that of the max jet centerline and gives a good physical indication of how the jet flow momentum is dissipated. Below in Figures 4.21 and 4.22 can be seen the halfwidth thickness as it propagates downstream for the .5 inch setups:
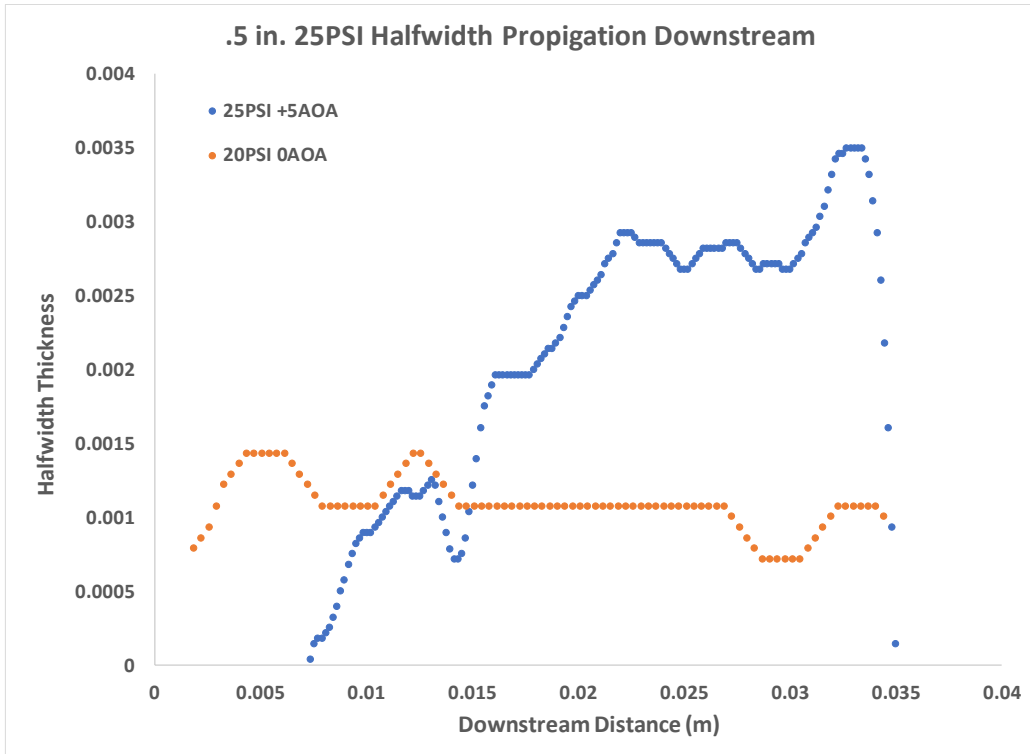
Figure 4.21 Slot Jet Halfwidth propagation downstream of .5 inch setup run at 25PSI
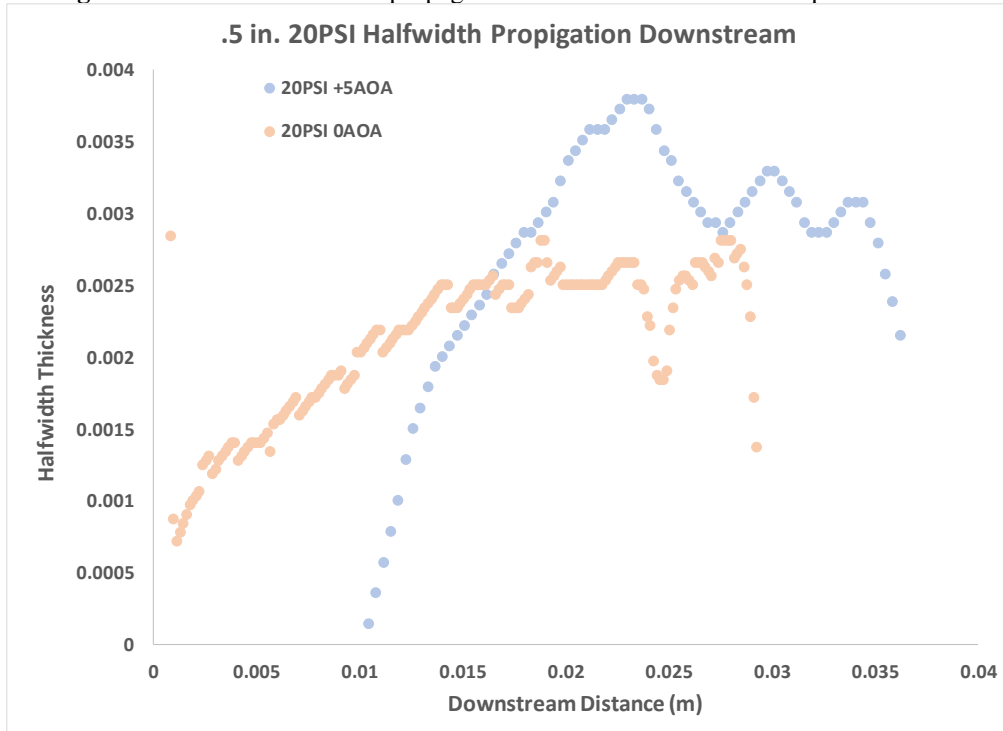
Figure 4.22 Slot Jet Halfwidth Propagation downstream of the .5 inch setup run at 20PSI

Figures 4.21 and 4.22 show the halfwidth thickness of the .5 inch setups. No matter the speed, the halfwidth thickness was larger upstream when the for the 0AOA setups but downstream the halfwidth becomes thicker for the +5AOA setups. This trend compares well with the 1 inch setup and again showing the validity of the statement that higher turbulent flows are entering the system when the airfoils are not angled as compared to angled. Higher growth rates of the halfwidth can be seen for the +5AOA setup by looking at the higher slope of the trend that the data show in the figures above. Therefor more mixing occurs when the airfoils are angled outwards as compared to not angled which compares well with the 1inch setups as well.

4.2.3.2 Shear Layer Propagation

Shear layer thickness is the next turbulent quantity analyzed and below in the following figures can be seen the shear layer thickness for both the 25 and 20 PSI runs:
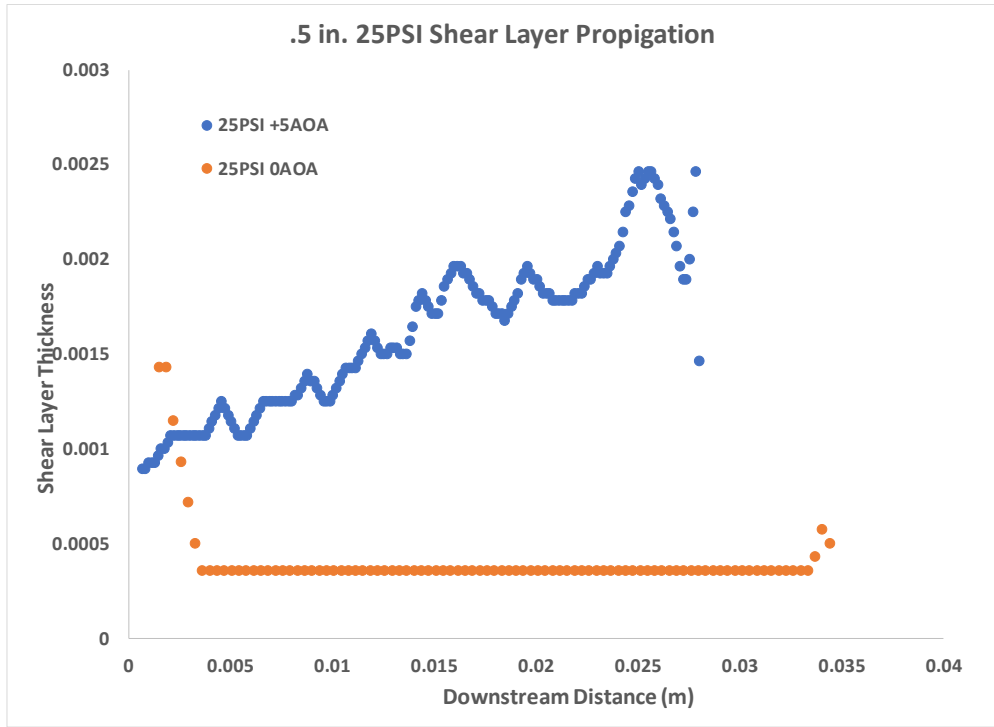
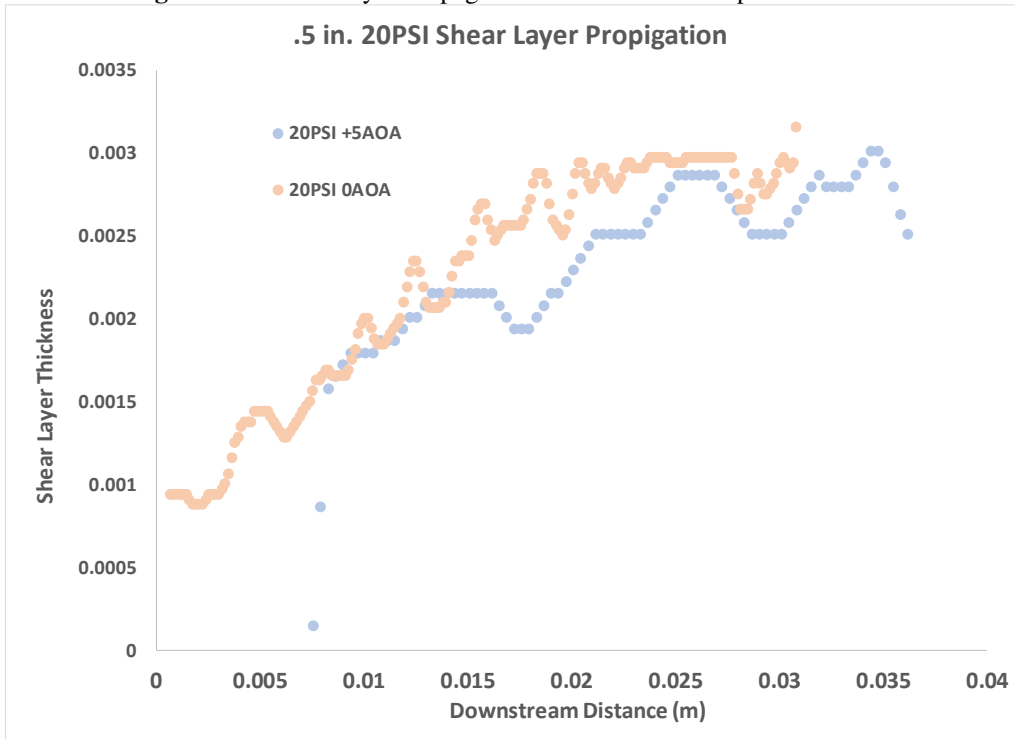**Figure 4.23** Shear Layer Propagation for the .5 inch setup run at 25PSI

**Figure 4.24** Shear Layer Propagation for the .5 inch setup run at 20PSI

71

In Figures 4.23 and 4.24 above can be seen the shear layer thickness of the turbulent jets seen in the experiment as the fluid moves downstream. The common trend in these experiments of thickest shear layer when the airfoils are not angled upstream is seen here for all the experimental runs. But at high speeds the shear layer thickness drops off quickly leading to a small shear layer downstream. At low speeds the shear layers converge at about the same thickness and downstream distance for each slot jet speed run and stay like that as the fluid moves downstream. Greater mixing is achieved by the +5AOA setups as the shear layer is largest at high speeds and the same size with the 0AOA setup at low speeds.

4.2.3.3 Turbulent Intensities

Centerline nondimensionalized Urms of the system can be seen below in Figures 4.25 and 4.26 for the two experimental assemblies run at two different speeds:
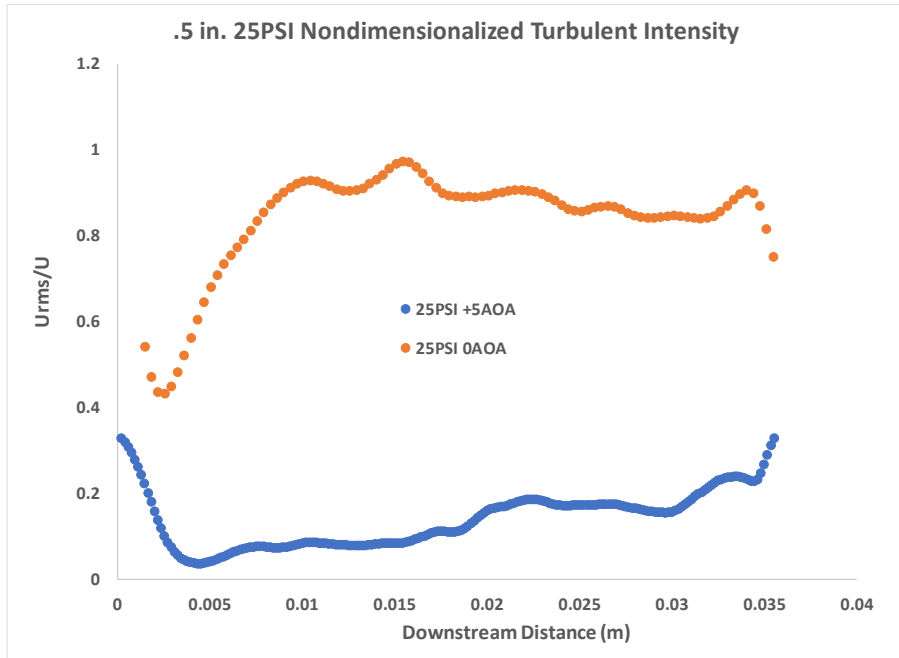
**Figure 4.25** Urms/U at the centerline of the system for the .5 inch setup run at 25PSI
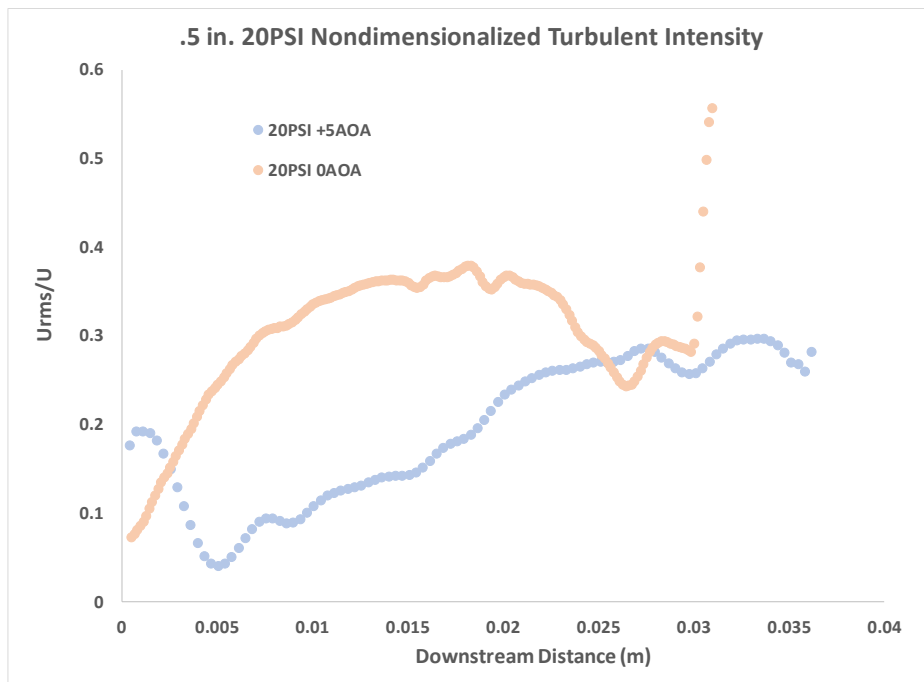
Figure 4.26 Urm/U at the centerline of the system for .5 inch setup run at 20PSI

Figures 4.25 and 4.26 show the turbulent intensities for each experimental run at the centerline of the system as the fluid moves downstream. At high speeds, there is higher turbulence when the airfoils are not angled. This trend can be seen to be dissipating as the fluid moves downstream due to the growth rate of the profiles dissipating downstream. At low speeds, turbulence is seen to be greatest for the 0AOA setup upstream but as the fluid moves downstream the turbulence levels are seen to converge between the +5 and 0AOA setups.

Below in Figures 4.27 and 4.28 can be seen the transverse profiles of turbulence at the center of the mid-section of the experiment:
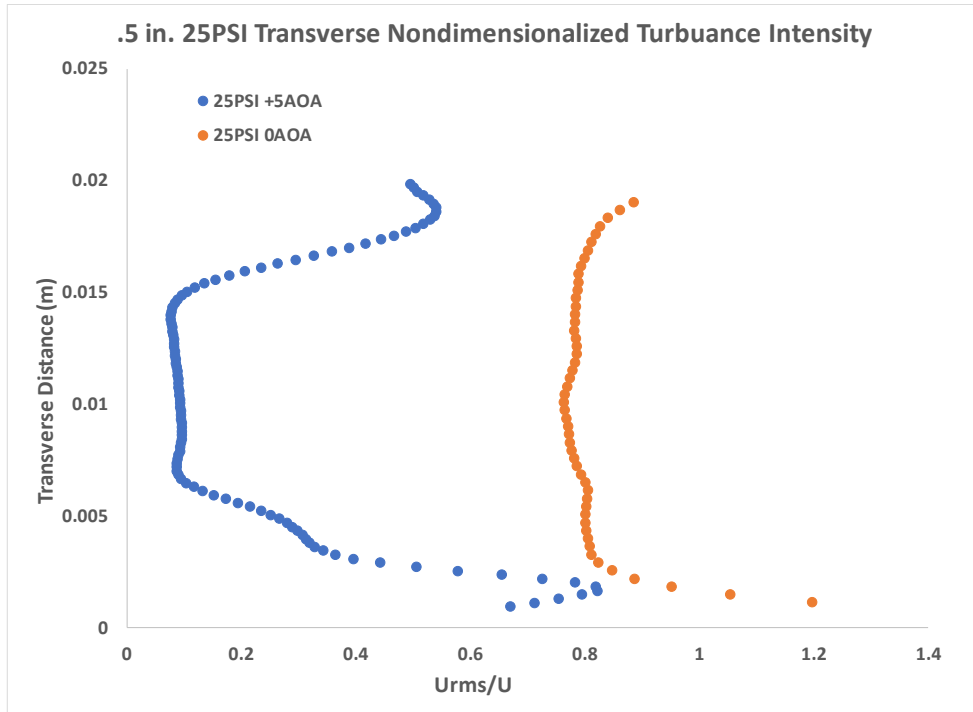
Figure 4.27 Urms/U in the cross stream direction at the center of the mid-section for the .5 inch assembly run at 25 PSI
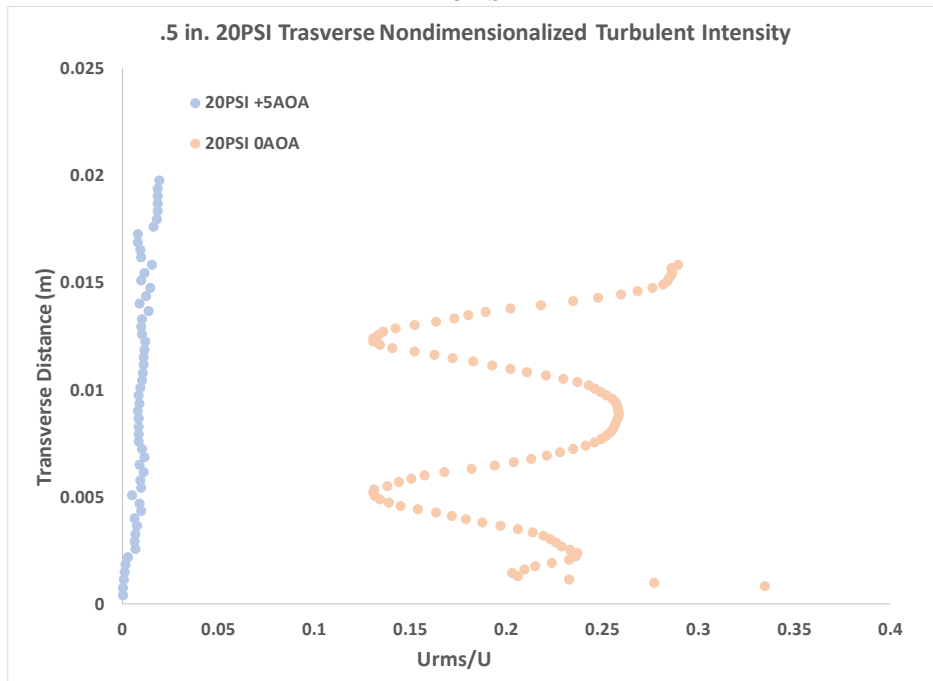
Figure 4.28 Urms/U in the cross stream direction of the center of the mid-section for the .5 inch assembly run at 20PSI

Looking at the figures above and comparing them to the transverse profiles for the 1inch setups, higher turbulence magnitudes are seen here but close to the boundaries. Higher turbulence at the boundaries indicate more recirculation which hurts thrust production. So, the .5 inch setups produce more turbulence in the recirculation zones which hurt the system's ability to produce thrust. It also shows that boundary layer turbulence is more prominent in the .5 inch assemblies which is to be expected. The minimal turbulence seen in the +5AOA setup run at 20PSI is thought to be caused by some incorrect data, as the fastcam pictures were too zoomed in on the system to properly catch boundary layer effects. Otherwise the trends seen in the turbulence profiles above compare well with the 1 inch setup.

4.2.3.4 Reynolds Shear Stress

Reynolds stress quantifies the turbulent mixing seen in the system. Reynold stress magnitudes at the center of the shear layer are calculated and in Figures 4.29 and 4.30 below can be seen the profiles of these calculations:
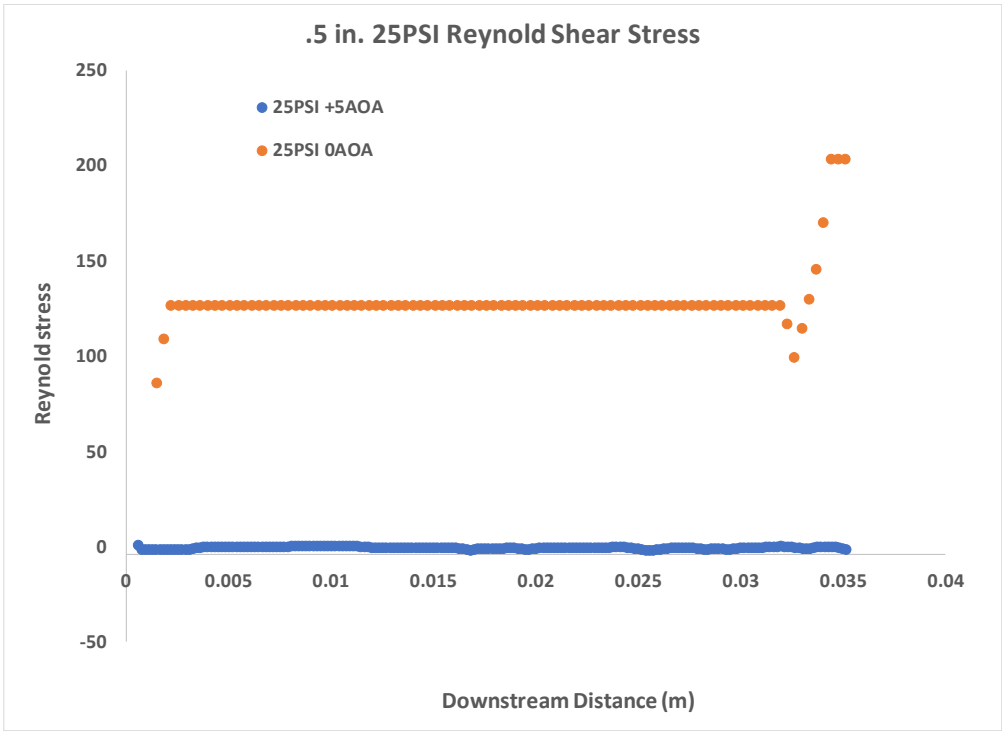
Figure 4.29 Reynold Shear Stress at the center of the shear layer in the .5 inch assembly run at 25PSI
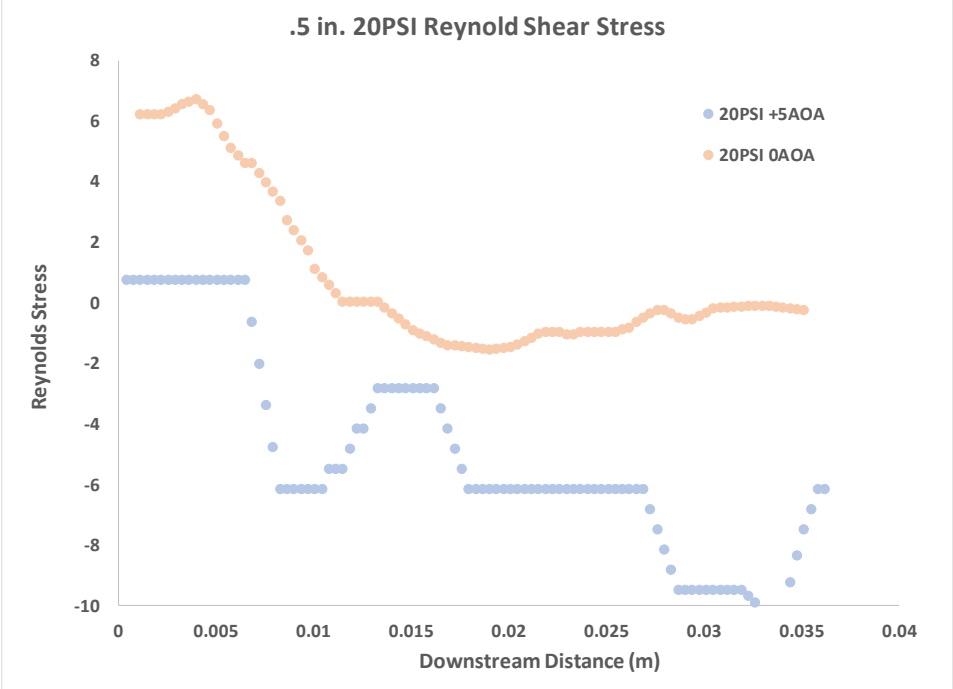

Figure 4.30 Reynold Shear Stress at the center of the shear layer in the .5 inch assembly run at 20PSI

Figures 4.29 and 4.30 show the Reynold shear stress seen at the center of the shear layer in the .5 inch experimental setups. The center of the shear layer is where the highest velocity gradients are, where vorticity develops with vortex rollup, and where there is the highest mixing and so max Reynolds shear is present. At higher speeds larger Reynold shear is seen which is to be expected; since there is more momentum in the system. The experimental assembly with the airfoils not angled is seen to have the highest Reynold as well, but it was seen with the Urms quantities that the higher mixing is coming from larger recirculation zones close to the boundaries of the 0AOA assemblies. The negative Reynolds seen for the 20PSI runs is thought to be caused by entrainment velocities dominating the mixing close to the slot jet exits. The lower slot jet speeds are not strong enough to dominate the mixing and so more velocity is coming into the slot jet flow creating negative V fluctuations which creates negative Reynolds.

4.2.4 Data Discussion on the effects of the independent variables on flow characteristics

The halfwidth thickness, shear layer thickness, Urms, and Reynolds shear stress profiles have been extracted and presented. Growth rates of the profiles halfwidth and shear layer profiles are seen and show that the -5AOA setups exhibit different growth rates then the other experimental assemblies. Relationships and trends seen between the average values of these quantities and how these trends are affected by the changing independent variables are discussed here. Followed by tabulated thrust and thrust augmentation ratios which will lead to the decision of which assembly optimizes thrust production.

Halfwidth propagation is the first fluid property presented and analysis of the profiles show an interesting growth rate for the -5AOA setups at high and low speed runs. The profile of the -5AOA assemblies show a logarithmic growth which allows it to jump suddenly in a short distance but

then dampen out downstream as well. The other assemblies exhibit a linear growth rate showing a slower growth upstream but also continued growth where the -5AOA profiles dampen out. This shows that the momentum from the slot jets mixes quicker and further upstream for the -5AOA setups. This indicates better momentum mixing but also limited entrainment upstream. A comparison of the average halfwidth thickness between all setups is seen below in Figure 4.31:
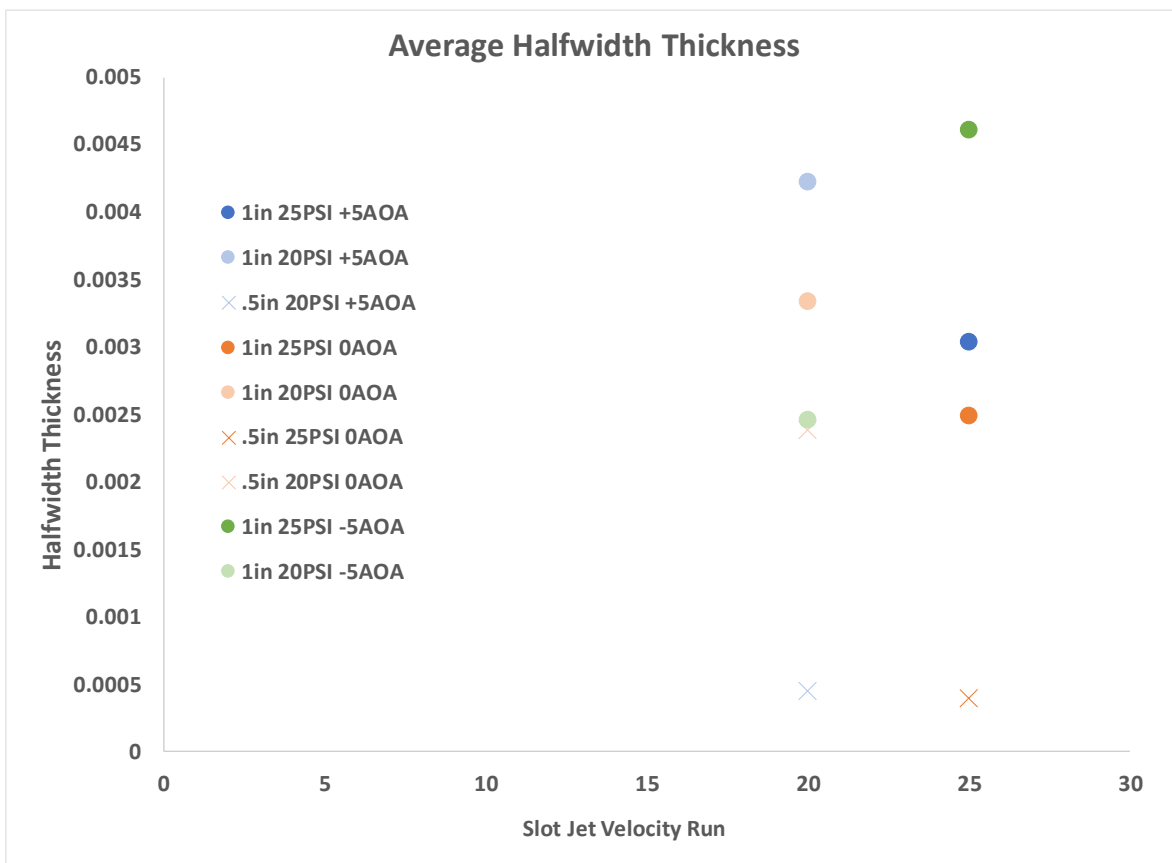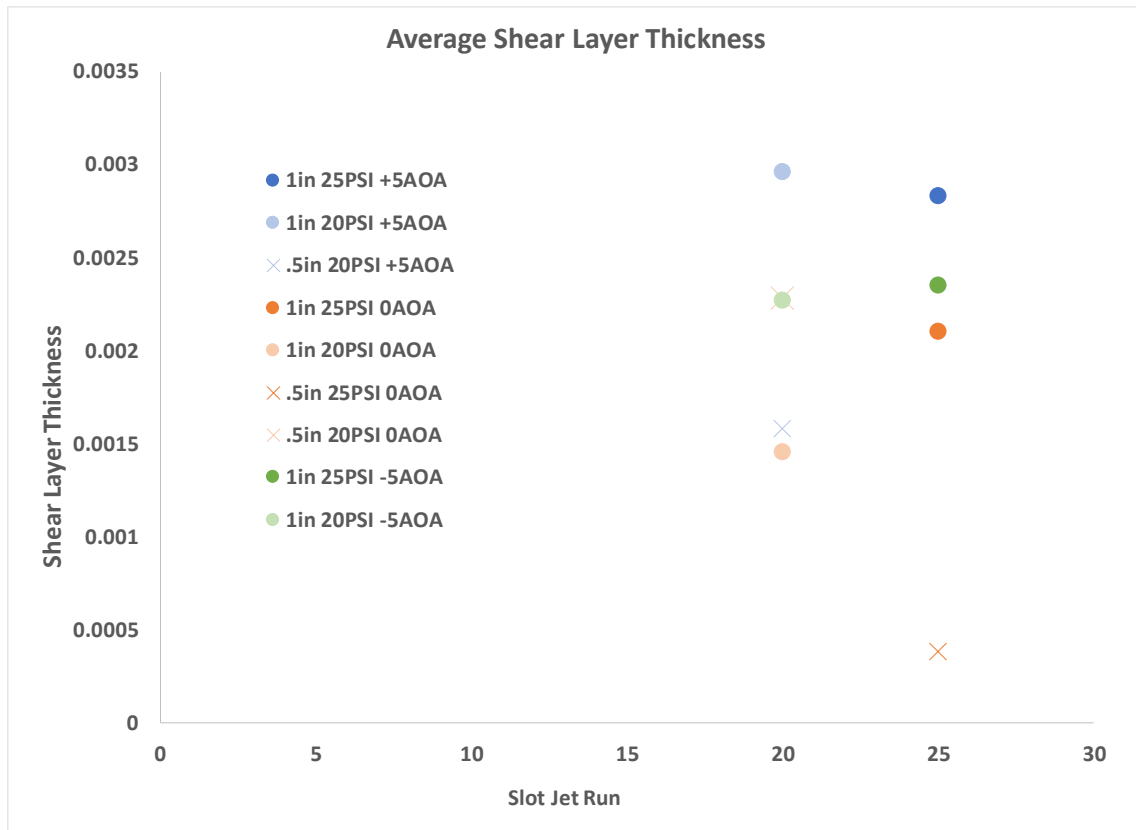

Figure 4.31 Average Halfwidth Comparison for all experimental setups

For high speed slot jet runs, the -5AOA setup is seen to have the largest halfwidth followed by the +5 and then 0AOA setups. For lower speeds, the halfwidth for the largest halfwidth is seen for the +5AOA setup followed by the 0 then -5AOA assemblies. The -5AOA assembly doesn't reach an

average thickness greater than the other assemblies at low speeds, but the thickness is still growing and will probably become thickest downstream. Lower slot jet velocity runs are seen to have thicker halfwidths then fast runs. This could be from the fact that higher momentum will push the dual jet merge point further downstream which would shrink the halfwidth as well. Halfwidths are seen to be smallest for the .5 inch setups as well indicating low momentum mixing.

The logarithmic jump for the -5AOA setups is believed to come from the constricted cross sectional area of the flow. As the fluid moves downstream, the cross sectional constriction cause the air to jump up mixing the high momentum quickly. The same concept is seen in Bernoulli's experiments that show a constriction in the cross section will lead to a change in velocity and pressure in the flow. This also lessens the amount of air being sucked into the system by shortening the time entrainment can be effective upstream by causing the jets to merge quicker. But this minimal input creates a larger mass deficit seen in Figures 4.8 which is good for thrust production. This extra force pushing the slot jet momentums together allows for efficient mixing of the high momentum upstream leading to higher bulk movement of the fluid particles which is also desired.

Shear layer thickness is the next turbulent quantity presented and quantifies the region of turbulent mixing seen in the experiments. Free shear flows develop velocity gradients due to viscous dissipation between the primary and secondary fluids, which can also develop turbulent mixing. These effects begin at the slot jet exits and create vorticity in the flow which increases the turbulence of the flow. These effects create a region of intense turbulence known as the shear layer. Seeing how this layer develops helps quantify the system turbulence characteristics which directly affect momentum transfer in the fluid particles which is how thrust is generated. The profiles of the shear layer thicknesses are presented in the results section and show the similar logarithmic

jump in shear layer thickness for the -5AOA setup as was seen for the halfwidth thickness. The constricting cross sectional area of the -5AOA setup is again thought to cause this jump. Below in Figure 4.32 is seen a comparison of average shear layer thickness between all the experimental assemblies:


Figure 4.32 Average Shear Layer Thickness Comparison of all experimental setups

The +5AOA setups show the thickest shear layer, followed by the -5 and then 0AOA setups. But the similar logarithmic growth rate of the halfwidth again appears in the profiles presented earlier indicating jet merging further upstream and limited entrainment into the system as was said for the halfwidth comparisons. This constriction in cross sectional area is believed to introduce a nozzle effect, or Bernoulli effect in the flow where constriction in the cross section speeds up the flow

but lowers the pressure. This Bernoulli effect is evident when looking at the U velocity contours in Appendix C as the -5AOA setups show the highest velocity peaks leaving the system and combined flow indicating high mixing upstream and bulk fluid movement.

Turbulent intensity (Urms) is the next variable extracted from PIV testing and quantified at the system centerline in the streamwise direction, and at the center of the mid-section in the transverse direction. The transverse profiles show high turbulence at the boundaries where boundary layers are prominent and expected. The Urms values at the centerline of the system show the magnitude of the fluctuating component of the velocity domain at the center of the system where the dual jet interactions are prominent. The streamwise profiles show increasing trends in the turbulence as fluid moves downstream which is expected, as the dual jets pull the flow towards the center. A comparison of the average nondimensionalized intensities in the stream wise direction for each setup can be seen below in Figure 4.33:
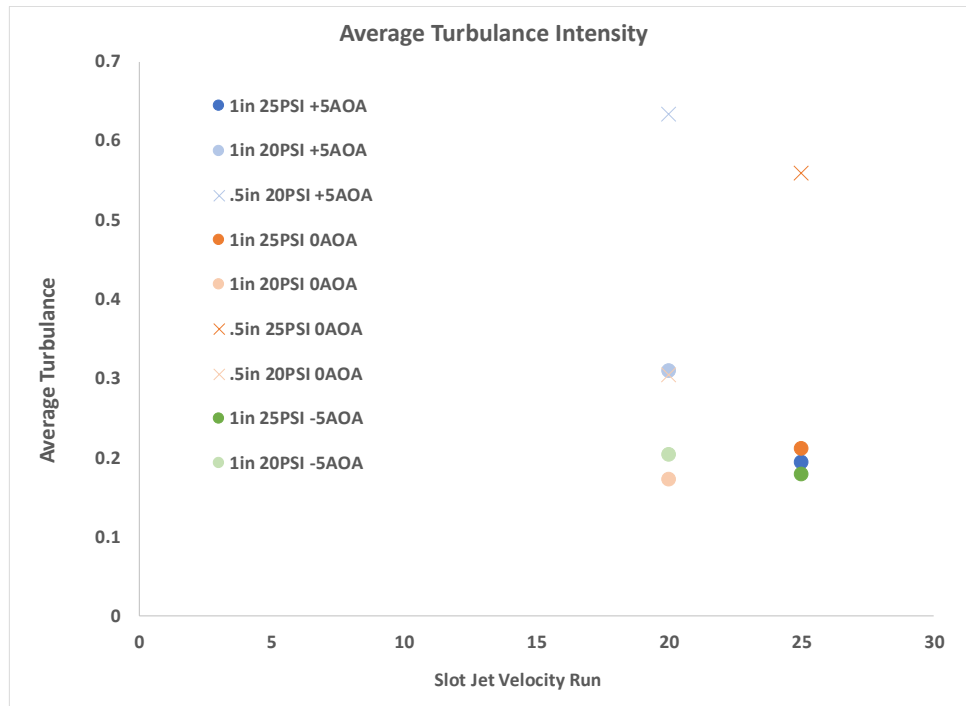
Figure 4.33 Average Centerline Urms/U comparison between each experimental setup

With increasing turbulence downstream higher momentum mixing is achieved which is desired for this experiment. Looking at the comparison above, the .5 inch setups show the greatest turbulence. This is interesting but is thought to be caused by the confined space of these setups increasing boundary layer effects in the system. This increase in boundary effects will increase turbulence and increase shear effects coming from the boundary layers formed. For the 1 inch setups, not much difference is seen in the average turbulence at high or low speed. The +5AOA assemblies are seen to develop the largest turbulence by a minimal amount, but the interesting part of this figure is that the -5AOA setups show minimal turbulence at the centerline. This indicates that turbulent mixing is very minimal in the -5AOA setups and that there is another driving force behind the high momentum mixing seen for this setup as has been indicated earlier as well.

83

The Reynold shear stress is the last turbulent quantity analyzed in this experiment and quantifies the turbulent mixing in the system. Higher Reynold magnitudes indicate higher turbulent mixing which can stem from multiple sources of turbulence and leads to better momentum mixing. The value is a vector quantity, so the sign of the Reynold stress indicates direction and magnitude indicates amount. If one was to imagine a pocket of fluid moving in a high momentum positive flow in the x direction, and this fluid pocket jumps up to a lower momentum fluid. This jump introduces high momentum to the low momentum and was in a positive direction which would create a positive Reynolds; this is the general idea of Reynolds stress. A comparison of the average Reynold stress quantities evaluated at the center of the shear layer where mixing is maximum can be seen below in Figure 4.34:
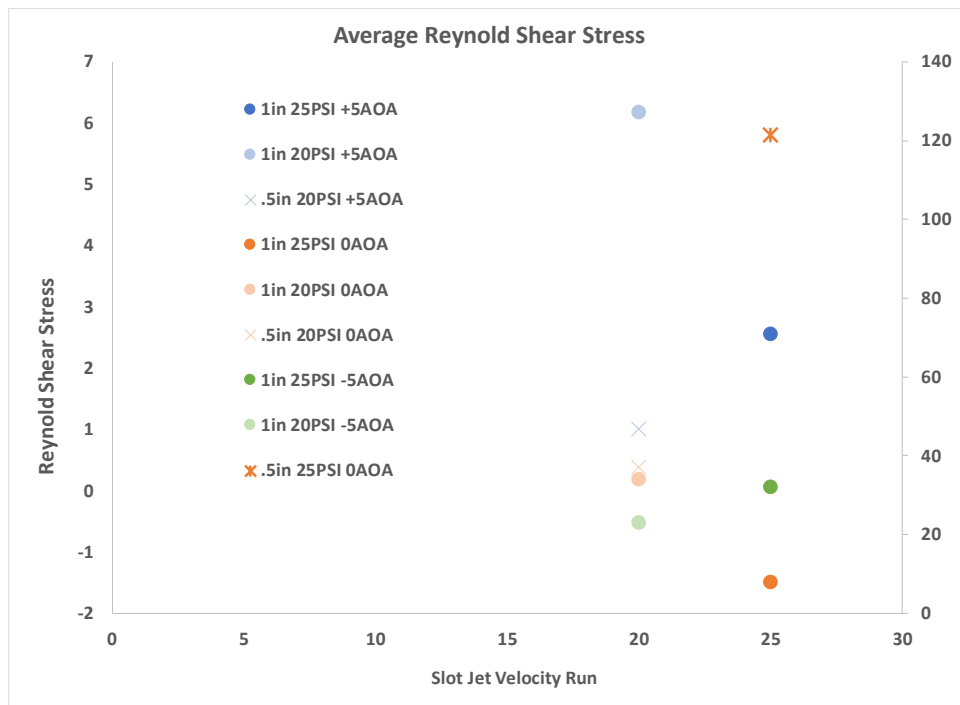
Figure 4.34 Average Reynold Stress comparison between all experimental setups

Reynold stress for the .5in 25PSI 0AOA setup was so large that it was the only point put on the secondary y-axis. This shows that that high turbulent mixing occurs during the .5 inch setups which shows again the dominant role boundary layers play in this constricted setup. But after that, the +5AOA setups show moderate mixing and then the rest of the setup show very low Reynold stress indicating low turbulent mixing. The -5AOA setup shows almost no Reynold stress in the profiles or in this comparison all of which stay at around 0. This indicates that turbulent mixing is minimal in these setups but the halfwidth and shear layer profiles show that the momentum mixing for these setups is high. This is the final indicator that there is another driving force factor that leads to the thick shear layers and halfwidths in the -5AOA assembly, discussion of which will be given in the following sections.

4.2.4.1 Slot Jet Velocity, Angle of Attack, Confinement Effects on Thrust Production

The main purpose of these experiments is to assess the fluidic properties of the proposed propulsion system and decide on the most efficient setup. Thrust is generated from the transfer of momentum energy in this fluidic system, and the governing thrust equation is given in Equation 10 of this paper. Examining that equation, it is evident that high mass flow and velocity differences are desired. Still looking at the thrust equation, it can also be seen that efficient thrust is developed when the highest bulk fluid flow is attained meaning the highest amount of fluid particles gain more momentum through the momentum mixing seen in the system, which is shown in Figure 4.8 for the control volume analysis. The driving factors behind this momentum transfer in the system is given in the governing equations and RANS equations presented in earlier chapters. It is believed that turbulent mixing will help transfer the high momentum introduced into the system but there are also other factors effecting momentum transfer to account for.

85

Slot jet velocity effects are one of the three independent variables tested in these experiments. Looking at the one dimensional effects of the flow with the Pitot testing, it is seen that higher velocity deficits in the transverse profiles were seen for higher slot jet runs. High deficits indicate lower bulk fluid movement which is an indication of less efficient momentum transfer in the system. Looking at the two dimensional effects of the flow with PIV testing, it is seen that lower speed slot jet runs lead to higher mass flow differences in the system, thicker shear layers for the angled setups, higher turbulence at the center, and higher Reynolds stress for the +5AOA setup. Higher slot jet runs developed higher entrainment and centralized flows which in turn convects vorticity and turbulence downstream at a quicker rate . Higher convection rates of vorticity and turbulence is believed to be the driving factor behind the trends seen for the slot jet velocities.

The confinement spacing between the airfoils showed minimal effects on the turbulent quantities presented. Velocity deficits lowered as the airfoils were brought closer together in the Pitot Probe testing. All the .5 inch setups developed fully combined flow leaving the system according to the velocity profiles in the appendix. Halfwidth and shear layer thicknesses were lowest when the airfoils were brought closer together. But turbulence and Reynolds shear magnitudes are seen to be highest when the airfoils are close together. This is thought to come from boundary layers playing a more dominant role in the fluid dynamics of the system which introduces another source of turbulence increasing turbulent mixing as well.

Angle of attack is the last and key independent variable tested in these experiments. The three different angles tested were +5,0, and -5 degrees which is the same as moving the airfoils from outward to inward angling by 5 degrees. From the Pitot testing it is seen that velocity deficits of the transverse profiles decreased as the airfoils were moved from out to inward angling. Average

halfwidth and shear layer thickness are largest for the +5AOA setup followed by the -5AOA setup, except for the 1in 25PSI run where the -5AOA setup is largest. But as has been stated and seen in the profiles presented, the growth rate of these parameters for the -5AOA setup follows a peculiar logarithmic trend indicating another driving factor of the momentum mixing in that assembly. Turbulence is seen to be greatest for the 0AOA setup followed by the +5AOA setup at high slot jet speeds and is greatest for the +5AOA setup at low slot jet speeds. The -5AOA setup shows lower turbulence at the centerline and small differences in turbulence between high and low slot jet speeds. The Reynolds shear stress is highest for the .5in 0AOA setup but following that is the +5AOA setups. It can also be seen that the -5AOA setup has lowest Reynolds indicating low turbulent mixing. But the velocity contours, halfwidth, and shear layer thickness profiles indicate high momentum mixing. Further validation to the statement that momentum mixing is driven by pressures in the -5AOA system stemming from Bernoulli's theorem and cross sectional constriction is given in the next section.

Thrust is the system component that is the be optimized in its development. Thrust generation is governed by the momentum conservation equation seen in Equations 2 and 3 in earlier chapters Assuming homogenous flow with limited pressure differences between the inlet and outlet of the system thrust is calculated using Equation 10. Bulk fluid movement is the general desired outcome from the momentum mixing examined as this will create the most efficient thrust. In other word, the largest amount of momentum energy should be picked up by the largest amount of fluid mass in the system. Below in Tables 4.7 and 4.8 are the time average calculated thrust values for each 1inch assembly, and for the .5in 25PSI 0AOA and .5in 20PSI +5 and 0AOA assemblies:

Table 4.7 Tabulated Time Average Thrust for each 1 inch assembly

1 inch Test Assembly			
25PSI		**20PSI**	
+5AOA	0.0835	+5AOA	0.1061
0AOA	0.0000	0AOA	0.0038
-5AOA	0.0315	-5AOA	0.0309

Table 4.8 Tabulated Time Average Thrust for each .5 inch assembly specified

.5 inch Test Assembly			
25PSI		**20PSI**	
0AOA	0.0054	+5AOA	0.0149
		0AOA	0.0004

Thrust augmentation ratios each respective setup seen in Tables 4.7 and 4.8 can be seen in Tables

4.9 and 4.10 below:

Table 4.9 Thrust Augmentation Ratio for each 1 inch experimental assembly

1 inch Test Assembly			
25PSI		**20PSI**	
+5AOA	1.8422	+5AOA	2.1319
0AOA	1.2663	0AOA	1.4767
-5AOA	1.6340	-5AOA	1.8441

Table 4.10 Thrust Augmentation Ratio for the associated .5 inch experimental assembly

.5 inch Test Assembly			
25PSI		**20PSI**	
0AOA	1.8848	+5AOA	2.3537
		0AOA	1.5499

Thrust calculations are seen above in Tables 4.7 and 4.8. Largest thrust is seen to develop for the

+5AOA setups, followed by the -5 and then 0AOA assemblies. The 0AOA assemblies developed

zero thrust invalidating that assembly as a viable option for the proposed propulsion system.

Comparing these numbers to that seen in Figure 4.2 a large difference is seen due to the additional

input flow data gathered through the PIV testing and such a difference is to be expected. Figure 4.8 shows the calculated thrust and mass flux comparison where a direct relation between mass flux and thrust production is seen. Using the computed thrust and thrust augmentation ratios it is clear to see that the 1in. +5AOA assembly is the optimal thrust production setup. This setup allows for the greatest amount of the air to be sucked into the system through entrainment and efficient momentum mixing create high bulk fluid movement indicated in the mass flux information. But what is the driving force behind this optimal system; is to be discussed in the next section.

4.2.5 Driving Force Behind Momentum Dissipation

Bulk fluid movement as described earlier is an indicator of efficient momentum dissipation between primary and secondary fluids. Figure 4.8 shows that the highest bulk fluid movement and thrust production is seen in the +5AOA assemblies. What driving force in the fluid causes the high momentum mixing in the +5AOA setups; What us the driving force behind the abnormal logarithmic growth rate of the -5AOA setups? These are some of the questions to be discussed here in order to see what forces are dominant in the fluidic system. In this discussion the .5 inch assemblies and the 1 inch 0AOA assemblies are negated as they are already shown to develop substantially lower thrust and mixing and so not feasible for the proposed system.

Analyzing the conservation equations and the RANS equations, momentum dissipation and convection is seen to be affected by pressure gradients, body forces, viscous dissipation, and turbulent mixing. Viscous dissipation is assumed constant among the different assemblies as the flow is non reacting and there is only one fluid in the system. Analyzing the presented profiles and thrust calculations, it is seen that the cross sectional area is the main changing parameter as the airfoils are moved from outward to inward angling or when the airfoil bodies are brought closer

89

together. Using Bernoulli's theorem, cross sectional geometry change is seen to effect pressures in the system. To look at the pressures developed in the system, Equation 12 which used to calculate velocity in the Pitot Probe experiments is rearranged to back calculate for pressure. Analyzing the units of pressure, it is seen to be a force applied over an area. To compare the pressure changing per flow cross sectional area change a time averaged pressure ratio of output pressure over input pressure is multiplied by the changing cross sectional area. The horizontal configuration (0AOA) is given a cross sectional area of 1 and the +5AOA assemblies have a cross section of 1 plus the change due to angling and -5AOA assemblies have a cross section of 1 minus the change due to angling. A comparison of this pressure related force to changing cross sectional areas coming from the airfoil angling is seen in Figure 4.36 below:
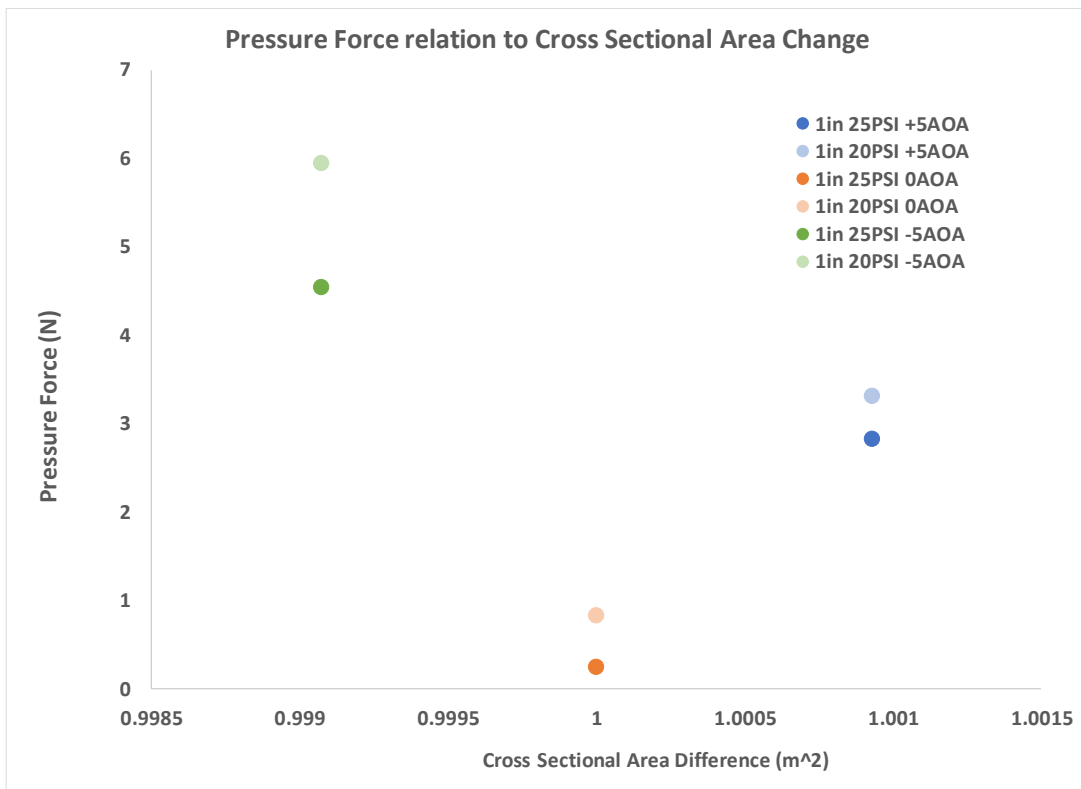
Figure 4.35 Pressure Ratio vs Cross Sectional Area Ratio for the 1 inch setups

As can be seen in Figure 4.36, pressure dominates in the -5AOA assemblies as compared to the other assemblies. This causes the logarithmic growth rates of the halfwidth and shear layers seen in the profiles of this assembly. Which then leads to high upstream momentum mixing causing combined flow to develop. Pressure pushed the high momentum flow towards the center of the assembly quickly mixing the flows creating the combined flow seen in the velocity contours, but this also chocks the entrainment flows into the system which ended up hurting thrust.

The +5AOA assemblies are calculated and presented to be the optimal setups with highest thrust production coming from the highest bulk fluid movement. Pressure is seen to be driving the momentum mixing seen for the -5AOA setups but is not so prominent in the +5AOA setup. The +5AOA assemblies develop the largest shear layers at high slot jet speeds and the largest halfwidths, shear layers, turbulence, and Reynolds at low slot jet speeds. These profiles indicate that turbulence and turbulent momentum mixing plays a larger role in the +5AOA assemblies then in the rest of the setups. The cross sectional area also increases as flow moves downstream which would slow down fluid according to Bernoulli's but also allows for more fluid mass to be in the system. Turbulent mixing is governed by the RANS equation and quantified by Reynolds Shear Stress. Analyzing the units of this stress a force is developed over an area coming from the shear development of the turbulence. As was done for the pressure, multiplying the Reynolds shear stress by the cross sectional area difference turbulent effects can be analyzed. Below in Figure 4.37 can be seen the comparison of this stress associated force to the cross sectional area difference coming from the airfoil angling:
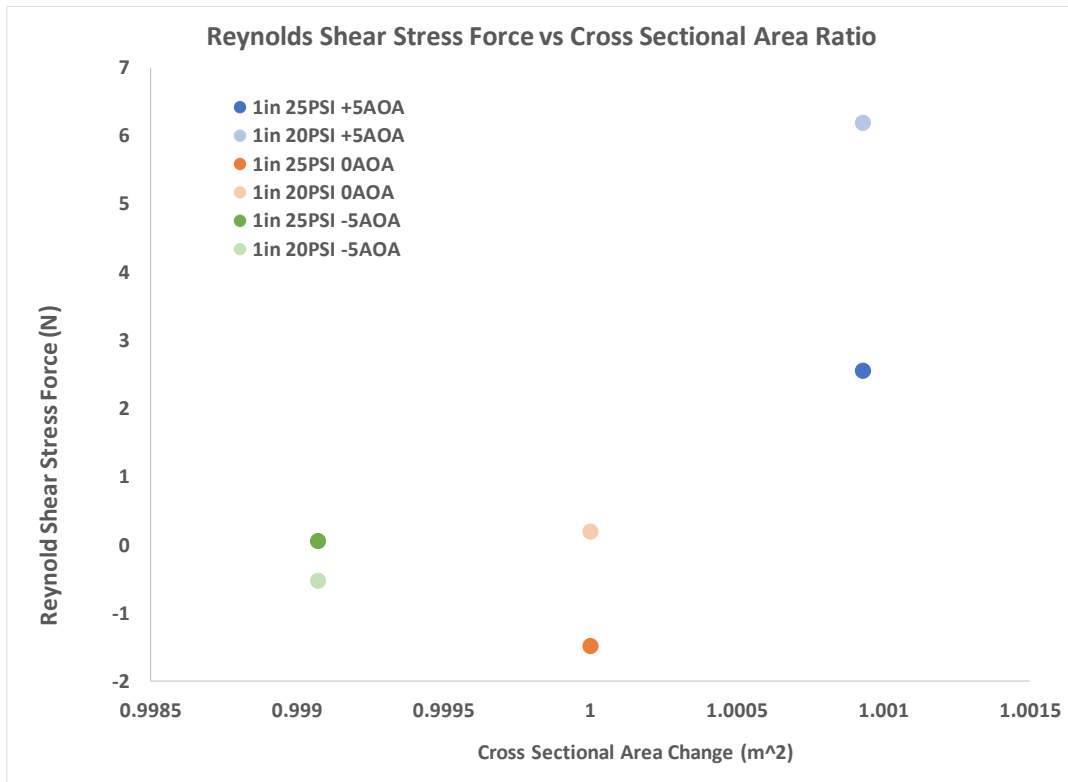
Figure 4.36 Time Averaged Reynold shear stress associated force for the 1 inch assemblies

The +5AOA assemblies are seen to have substantially larger Reynolds force which means substantially larger turbulent mixing for that assembly. The area increase from the angling of the airfoils shows to increase the Reynolds force indicating that increasing the cross sectional area increases the turbulent mixing in the assembly. This proves that the momentum mixing seen in the +5AOA assemblies is driven by turbulent mixing coming from the increase in cross sectional area as fluid moves downstream. As a final comparison, the associated Reynold force and thrust is graphed together and presented below for each 1 inch assembly in Figure 4.38:
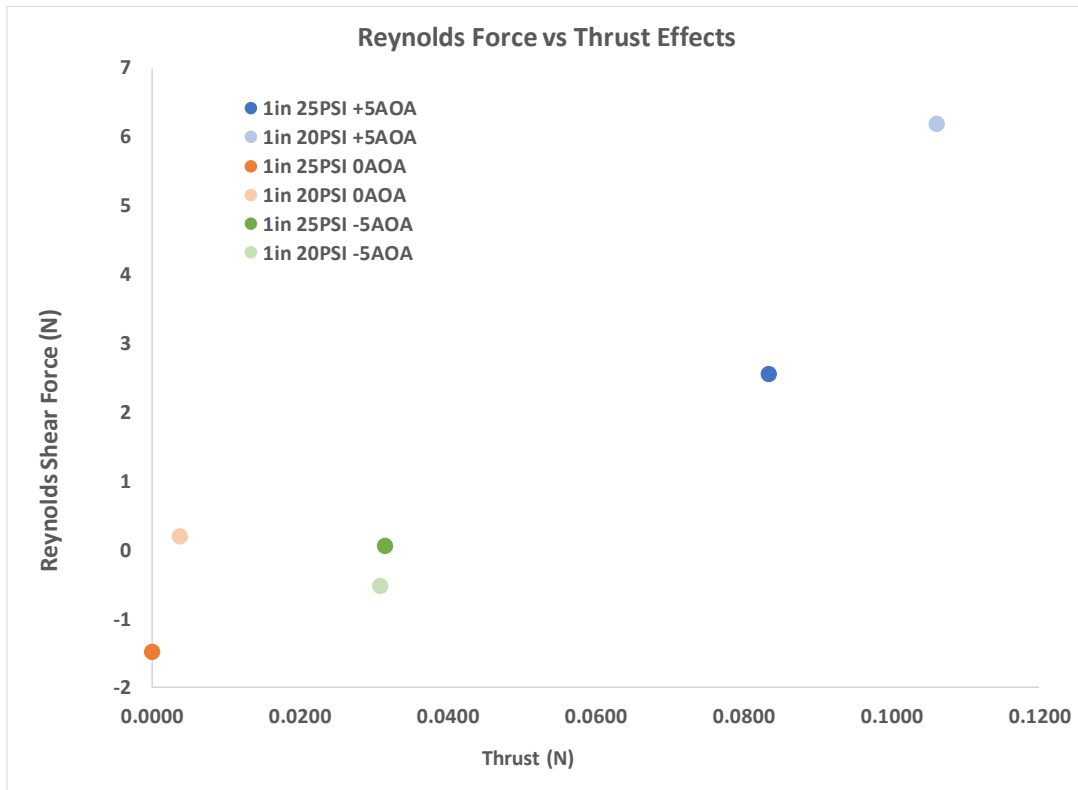
Figure 4.37 Reynolds shear force vs Thrust for the 1 inch assemblies

It is clearly seen in Figure 4.38 above, as Reynolds and by association turbulent mixing increases thrust increases. It is also clearly seen that the momentum mixing obtained in the +5AOA assemblies is driven by turbulent mixing coming from the increase in cross sectional area as the fluid moves downstream. The turbulent driven momentum mixing then produces the highest bulk fluid movement which then creates the highest thrust. Uncertainties are seen to be larger for the +5AOA assemblies, but the large jump in thrust and thrust augmentation ratio for the +5AOA setups compared to the other setups makes up for any instabilities the system can develop.

CHAPTER 5 CONCLUSION

The research conducted for this experiment helps to characterize the fluid dynamics of a high-performance co-flow fluidic thrust augmentation propulsion system. Better understanding of the fluid dynamics leads to the development of the optimal setup and further knowledge in the field of propulsion systems. Co-flow systems use the principle of entrainment in order to increase the mass flow of air in the system which in turn produces a passive means of thrust augmentation. Momentum mixing though turbulence and pressure gradients are seen to be the main driving forces behind thrust development in the system. Prior research is incorporated into this experiment in order to increase the understanding of the effects of this ejector, airfoil setup. Fluidic characteristics are presented from two different testing apparatuses, Pitot Probe and PIV testing and a discussion of the effects the independent variables have on these fluid characteristics is presented. This report ends with a presentation of an optimal system and discussion on the driving forces behind the optimal momentum mixing obtained in the setup.

The experiment was conducted in two phases; design and testing. The design phase consisted of producing an airfoil that can be used for UAV propulsion considering structural integrity, weight, materiel, and aerodynamic effects. 3D printing using ABS plastic is used to create the airfoils for the experiment and atmospheric air is the primary fluid. Testing consisted of 2 main experiments; Pitot Probe testing, and PIV testing. The three independent variables tested were slot jet velocities, confinement spacing, and angle of attack for all experimental assemblies. Pitot probe testing is used to analyze one dimensional flow aspects and velocity deficits. An uncertainty analysis is also performed on the Pitot data to see how error propagates through such experimental assemblies; whether it increases, decreases, or if there is minimal effect. PIV testing is done in order to

characterize the two-dimensional aspects of the fluid flow. Interesting growth rates are seen to develop for the halfwidth thickness and shear layer thickness developed when the airfoils are angled inwards. Turbulence is also seen to increase at the center as fluid moves downstream with increasing dual jet effects. Max Reynolds shear stress at the center of the shear layer also shows limited turbulent mixing for the -5AOA assemblies indicating limited turbulent mixing for these assemblies.

Slot jet exit speed is one of the independent variables tested. The main trend seen associated to the slot jet speed is that at lower speeds the turbulent characteristics increase. There is higher mass flux, halfwidth thickness, turbulence, Reynolds, and thrust for the lower slot jet speed runs. Convection is believed to be the driving force behind this described trend. Confinement spacing is another variable tested in the experiment and exhibited high effects on the turbulent mixing aspects of the flow. For the more constricted flow assemblies, combined flow is seen and larger turbulence, and Reynolds. This indicates that turbulent mixing becomes dominant in the momentum mixing process when airfoils are brought closer together indicating greater boundary layers affects.

Angle of attack was the last variable tested in the experiment. The outward angling of the airfoils increased the flow cross section downstream allowing more mass in the system. Applying Bernoulli's theorem, RANS equations and the comparing the associated Reynold force with the increasing cross sectional flow change turbulent mixing is shown to be the dominant driving force for the momentum mixing in the +5AOA setups Angling the flow inwards restricts the cross sectional flow and causes combined self-similar flow to be achieved leaving the system. This indicates high upstream mixing which is also shown in the large upstream growth rates of the halfwidth and shear layer thicknesses. The driving force behind such rapid mixing and high growth

rates is shown to be the pressure developed in the system through application of Bernoulli's theorem and comparison of cross sectional decline with pressure. At no angle of attack the greatest velocity magnitudes are seen but lower amounts of momentum mixing due to the constant flow cross section which leads to low thrust production.

Thrust, and thrust augmentation calculations are presented meeting the goal of this research; to present an optimal setup. The optimal assembly for thrust production is found to be when the airfoils are separated by 1 inch and angled outwards. This research shows that the increase in cross sectional area of the flow reduces pressure gradients but allows for higher turbulent mixing. The increase in turbulent mixing stems from the increase in cross sectional area which develops larger bulk fluid flow which in turn produces the greatest thrust.

Pitot testing accounts for only one dimensional flow dynamics and so is used to further validate the two dimensional information obtained in the PIV testing. Uncertainty is seen to decrease as the spacing between the airfoils is decreased either through angling or airfoil body movement. The constricting cross section when the airfoils helps to choke out some of the error stemming from the experimental procedures. But error is seen to stay low for all assemblies and the error associated when the airfoils are angled outwards is below 1% which is negligible; validating the optimized assembly with a 95% certainty. Velocity magnitudes extracted from Pitot Probe testing and PIV testing are seen to be of the same order which further validates both experiments.

Turbulent flows develop numerous process stemming from the shear layer interactions and different pressure gradients in the flows; the major one in this research is Entrainment. Research into the thrust producing capabilities of this process is presented in this paper and is being done by others for numerous different systems. The greatest new knowledge presented in this paper is that

momentum mixing for this coflow system is governed by either pressure or turbulent mixing depending on the airfoil angle. Such information can be used in new propulsion systems or other coflow propulsion system being developed for industrial use. Research to see how slot jet geometries, tripped slot jet turbulence, and thermodynamic analysis effect these fluidic behaviors are just some of the areas further work can be done on these systems. This report has discussed and shown that the proposed propulsion system meets industry needs and the data presented can help further the continued research on these coflow propulsion systems.

APPENDIX A: PITOT PROBE VELOCITY PROFILES
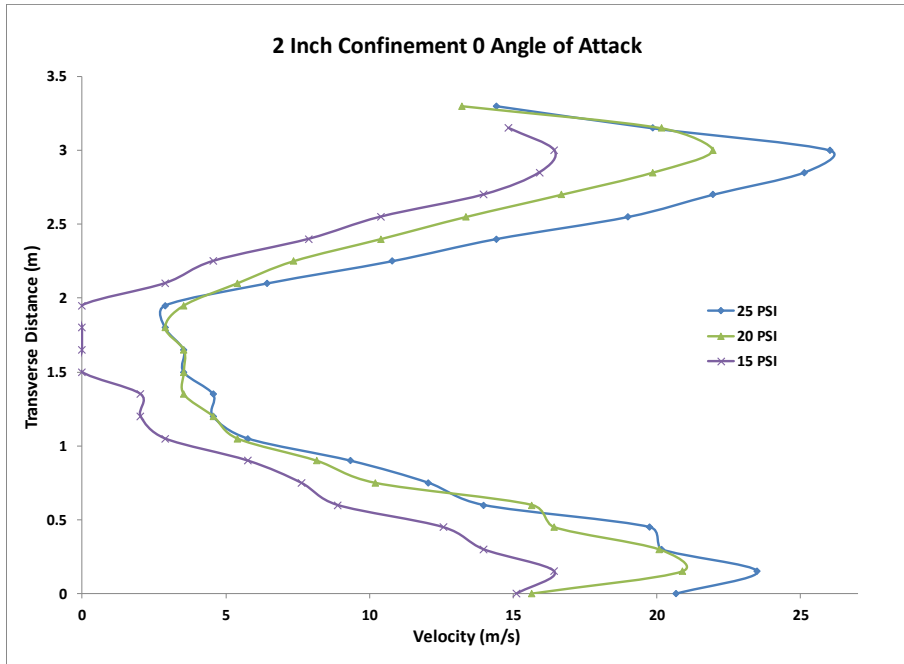
Figure 5.1 2 inch confinement space velocity profiles at different jet velocities and with the airfoils at 0 Angle of Attack
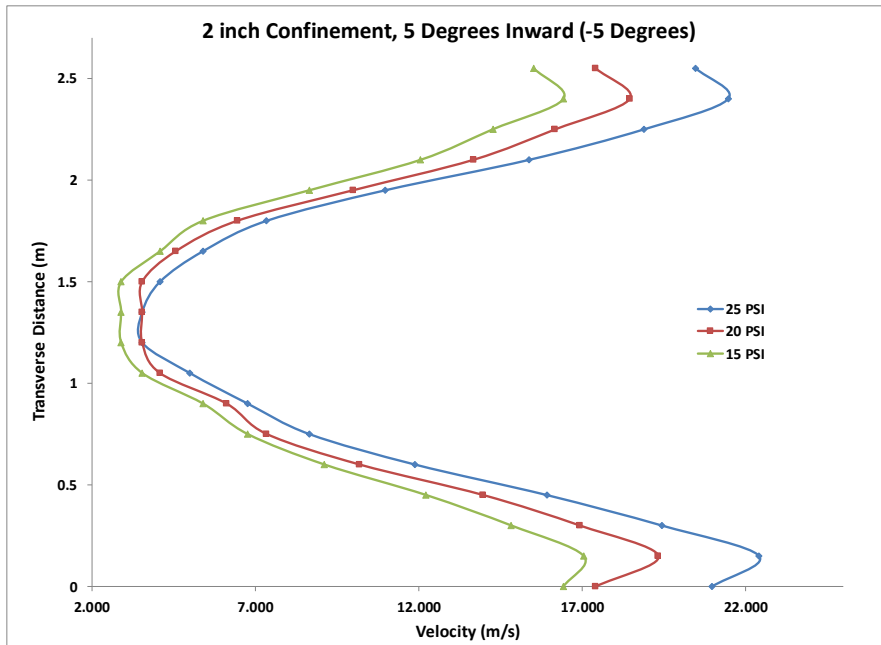
Figure 5.2 2 inch confinement space velocity Profiles at different jet velocities with the airfoils at 5 Degrees Inward Angle of Attack
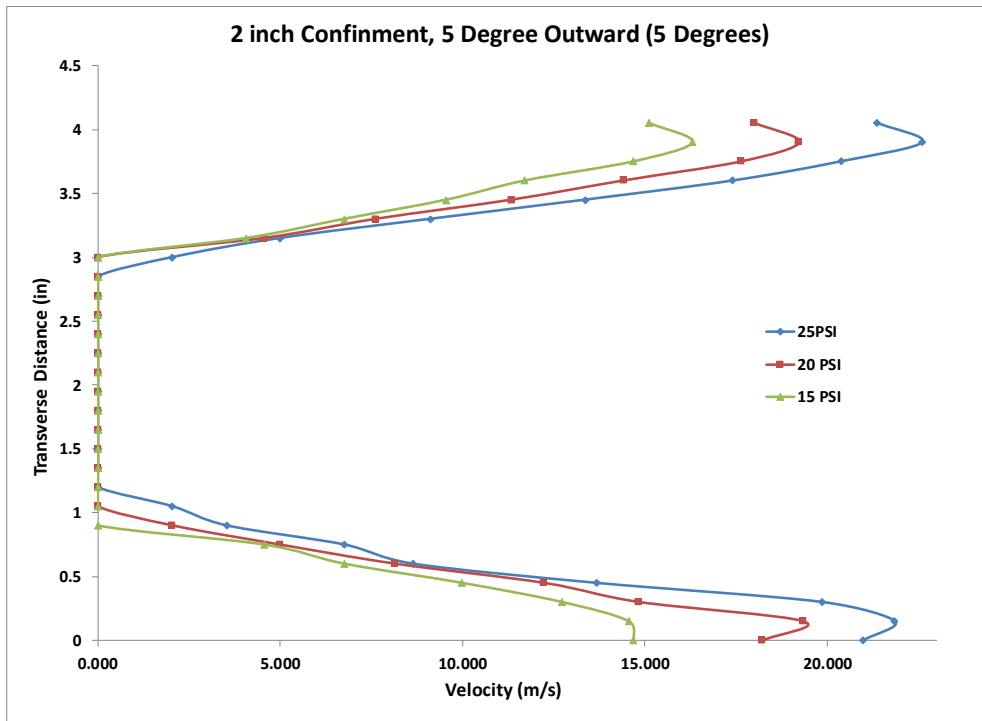
Figure 5.3 2 inch confinement space velocity profiles at different Jet Velocities with the airfoils at 5 Degrees Outwards Angle of Attack
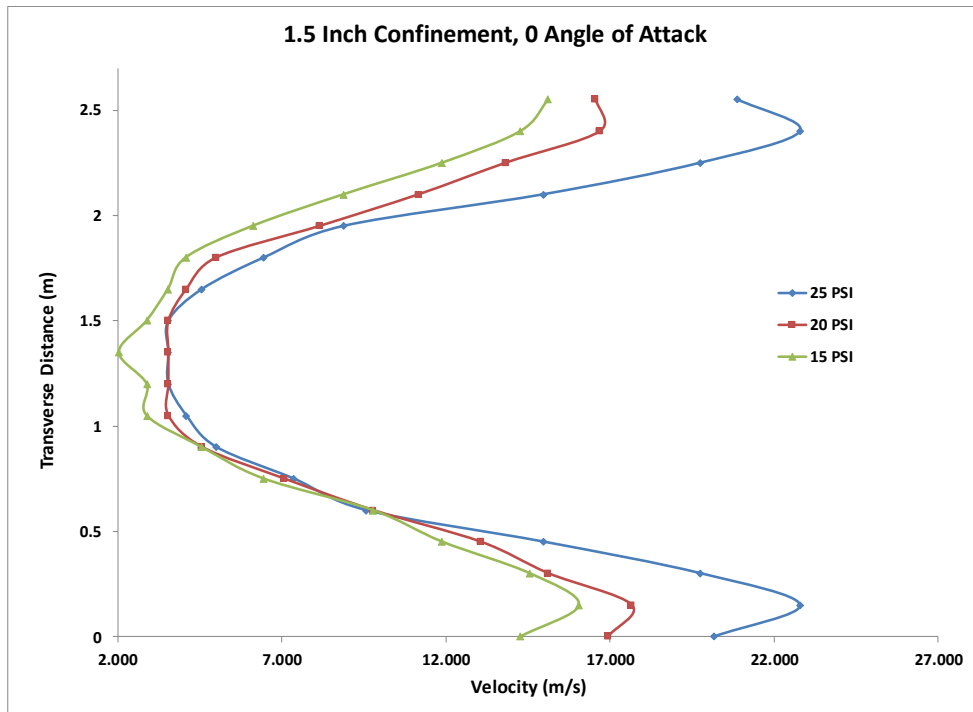
Figure 5.4 1.5 inch Velocity Profiles at different Jet Velocities at 0 Degrees Angle of Attack
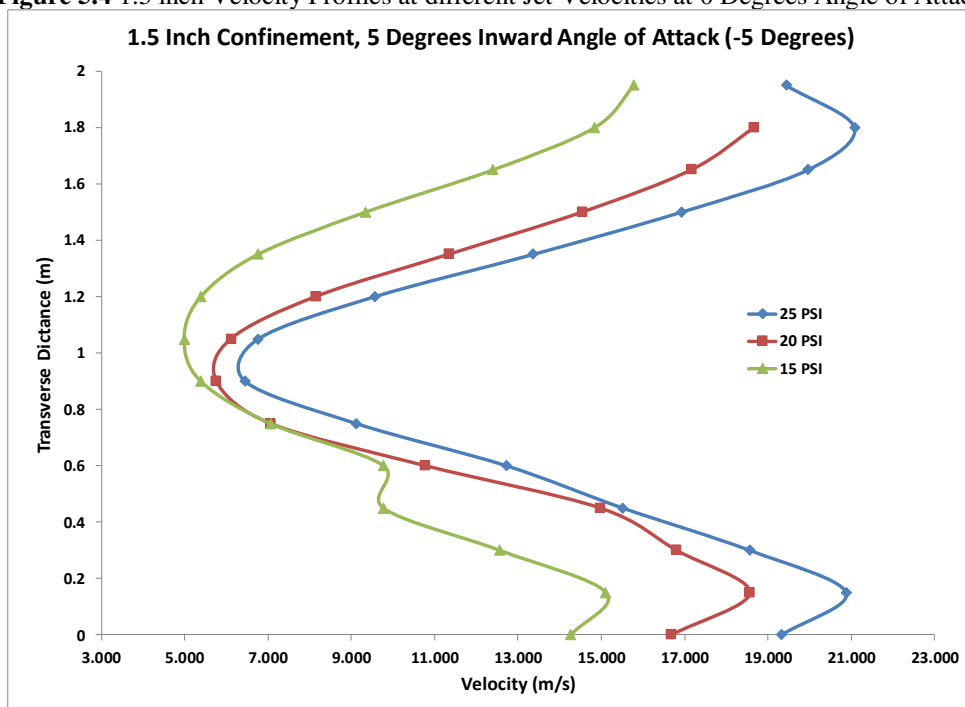
Figure 5.5 1.5 inch Velocity Profiles at different Jet Velocities at 5 Degrees Inward Angle of Attack
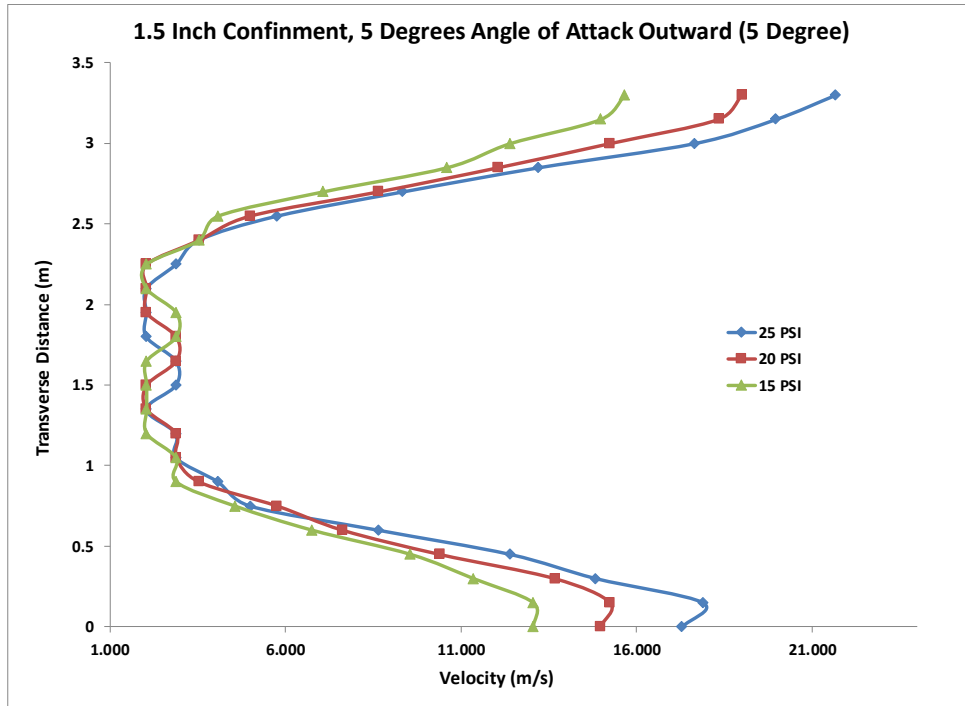
Figure 5.6 1.5 inch Velocity Profiles at different Jet Velocities at 5 Degrees Outward Angle of Attack
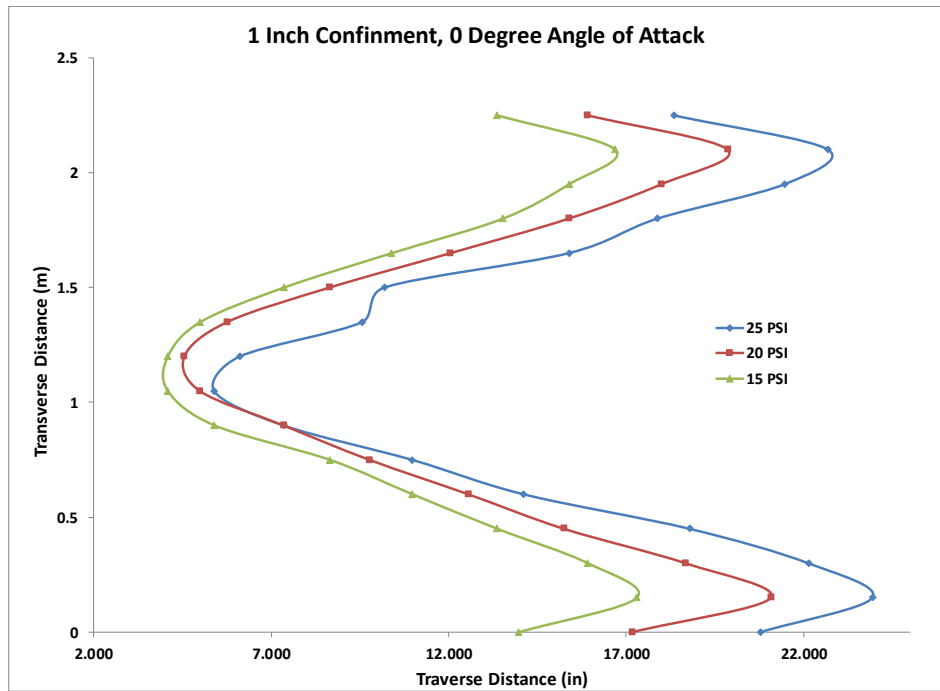
Figure 5.7 1inch Velocity Profiles at different Jet Velocities at 0 Degrees Angle of Attack
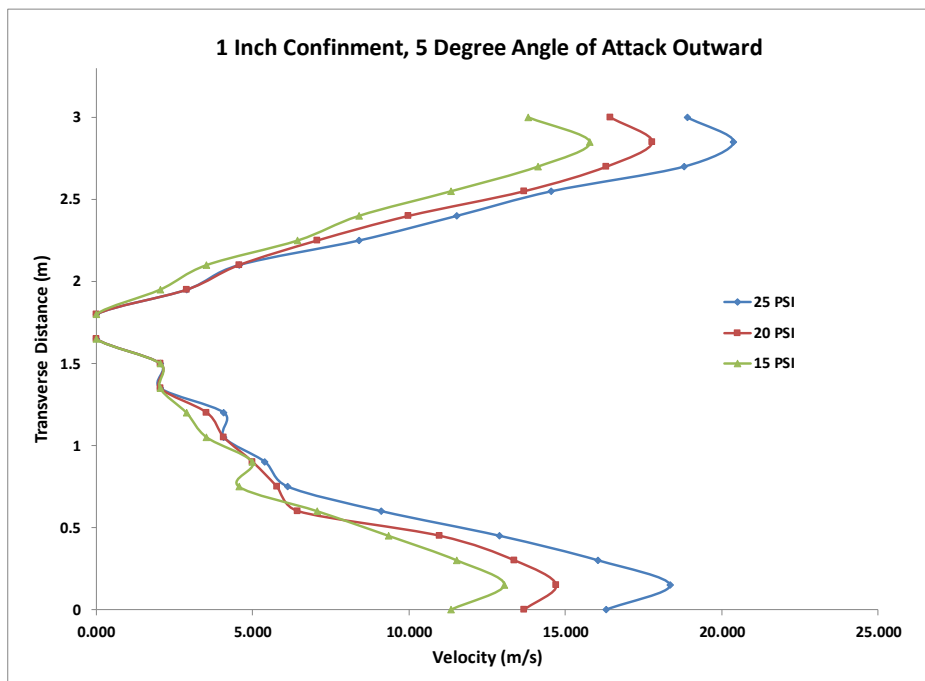
Figure 5.8 1inch Velocity Profiles at different Jet Velocities at 5 Degrees Outward Angle of Attack

APPENDIX B: PITOT PROBE UNCERTAINTY PROFILES
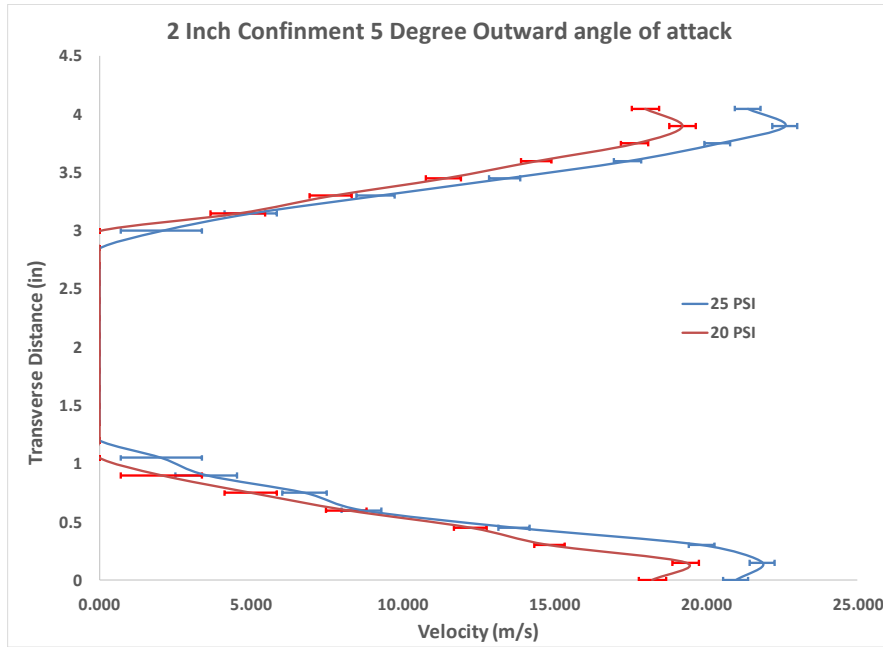
Figure 5.9 Velocity profiles at +5-degree angle of attack with error bars indicating the uncertainty of the velocity data for the 2 inch setup
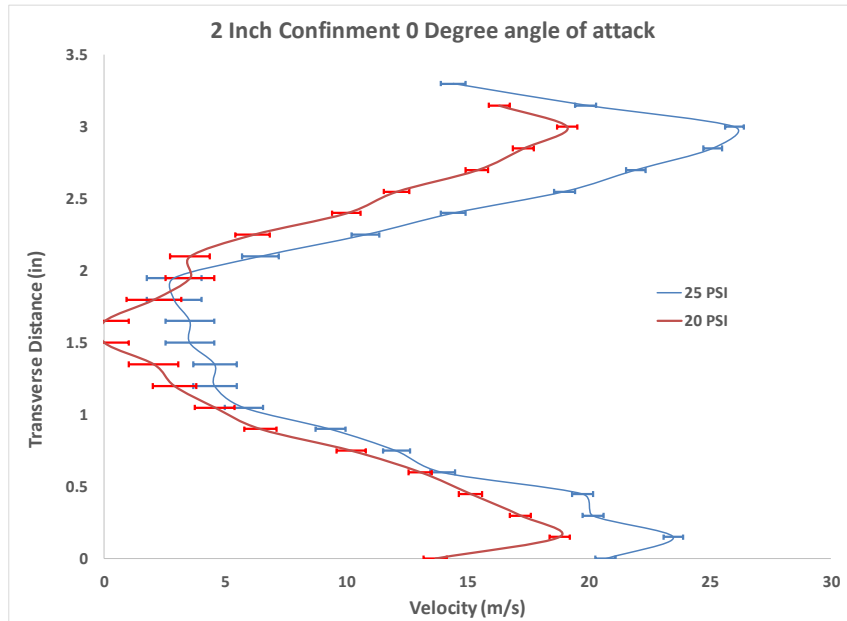
Figure 5.10 Velocity profiles at 0-degree inward angle of attack with error bars indicating the uncertainty of the velocity data for the 2 inch setup
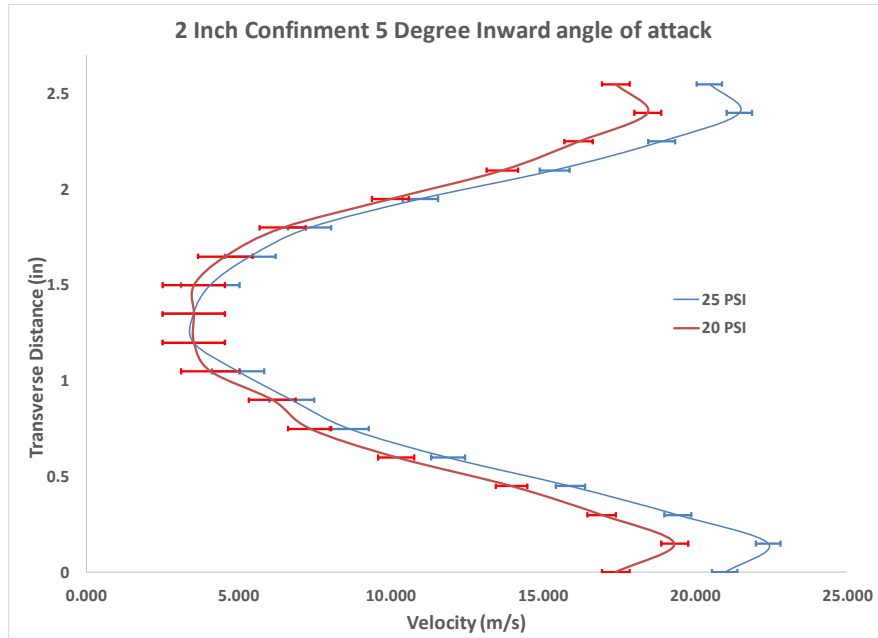
Figure 5.11 Velocity profiles at -5-degree Outward angle of attack with error bars indicating the uncertainty of the velocity data for the 2 inch setup
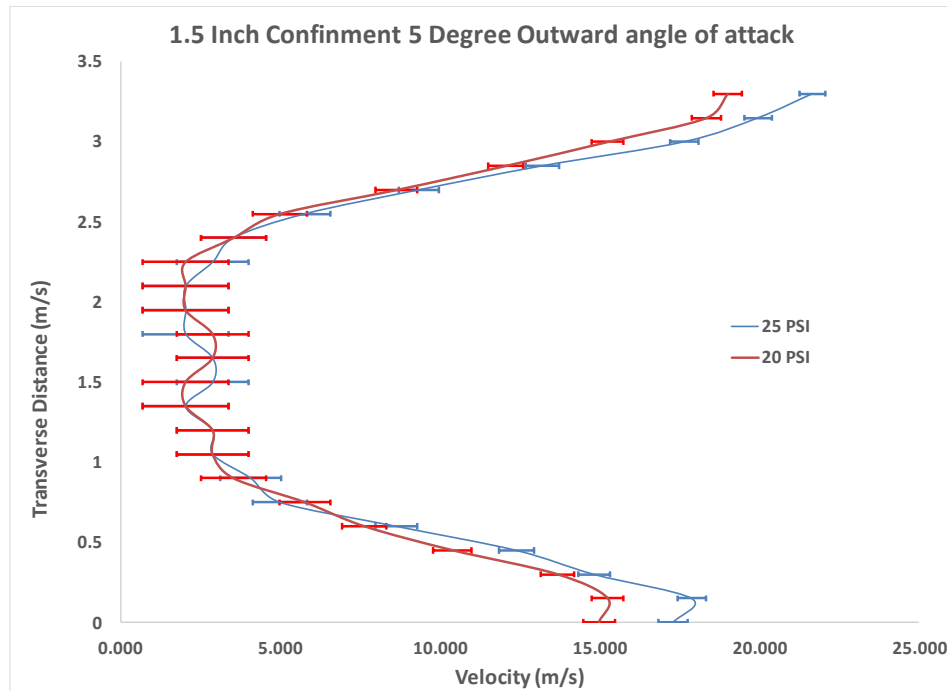
Figure 5.12 Velocity profiles at 0-degree angle of attack with error bars indicating the uncertainty of the velocity data for the 1.5 inch setup
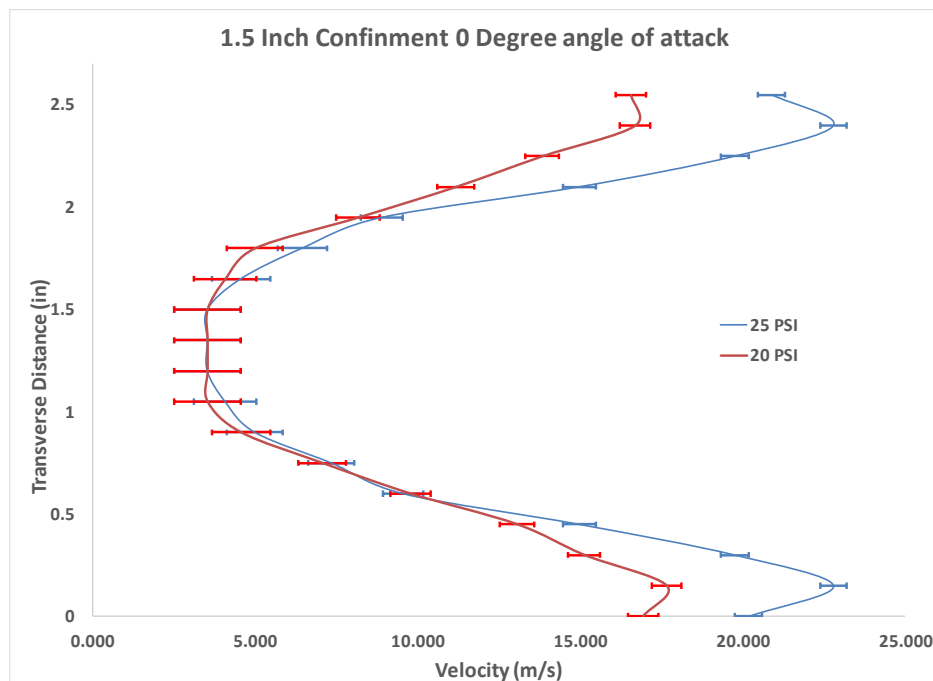
Figure 5.13 Velocity profiles at 5-degree inward angle of attack with error bars indicating the uncertainty of the velocity data for the 1.5 inch setup

107
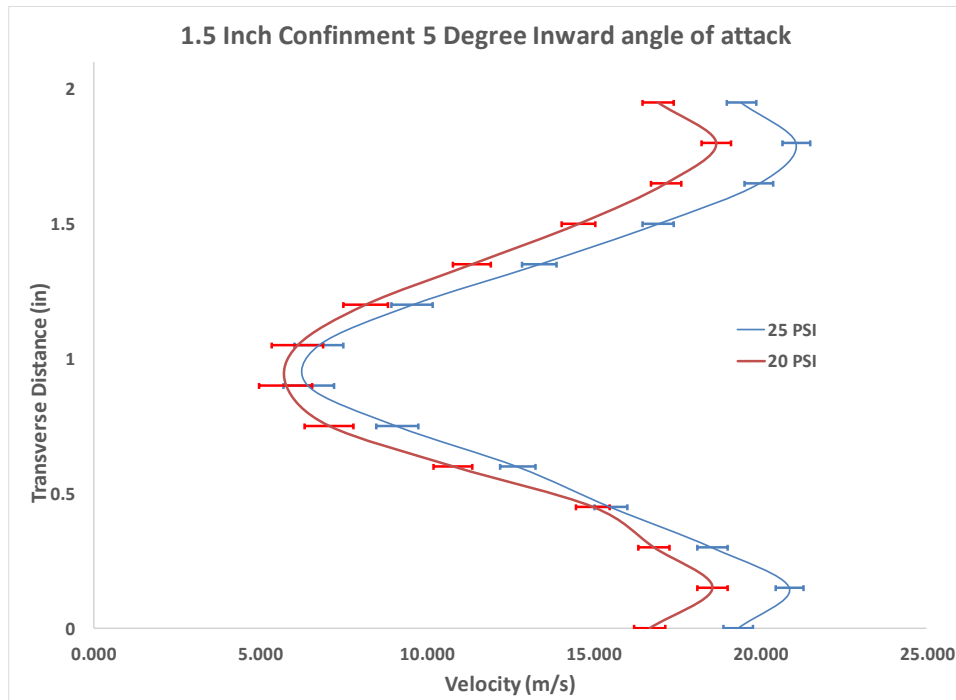
Figure 5.14 Velocity profiles at 5-degree Outward angle of attack with error bars indicating the uncertainty of the velocity data for the 1.5 inch setup

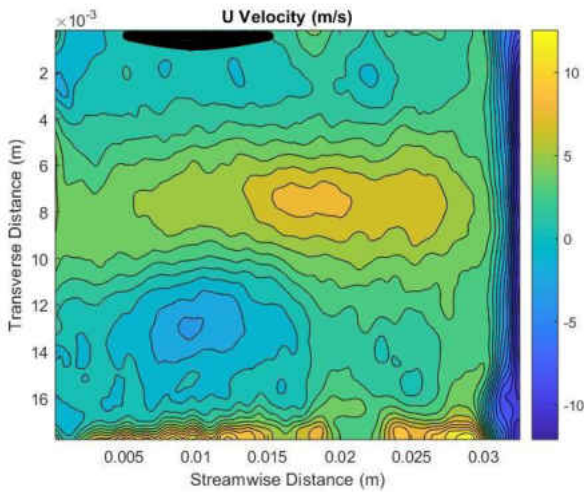# APPENDIX C: U VELOCITY CONTOUR MAPS
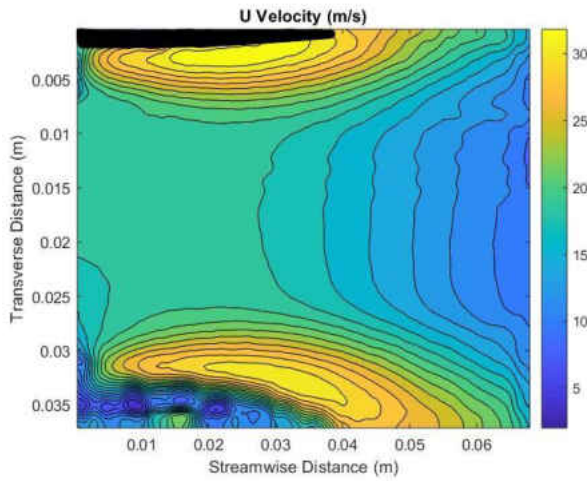
Figure 5.15 U Velocity contour plot of the Mid-Section of the 25 PSI run with airfoils angled 5 degrees outwards and spaced 1 inch apart
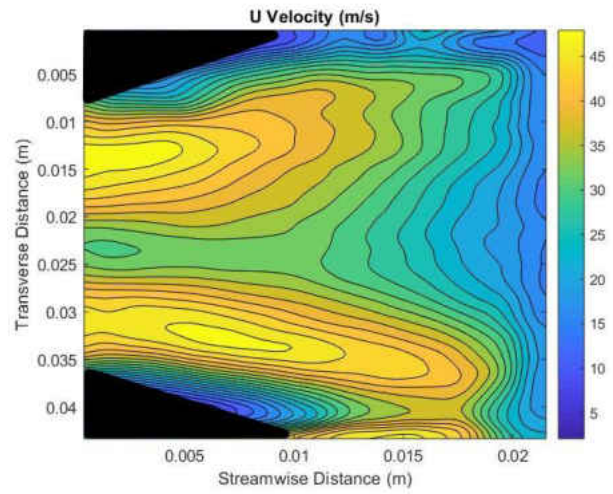
Figure 5.16 U Velocity contour plot of the Bottom Section of the 25 PSI run with airfoils angled 5 degrees outwards and spaced 1 inch apart
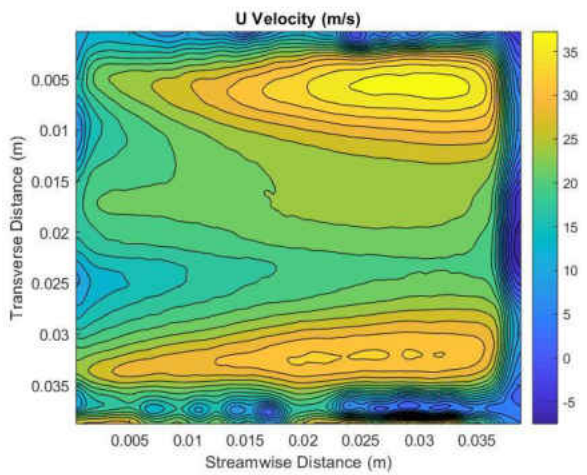
Figure 5.17 U Velocity contour plot of the Mid-Section of the 25 PSI run with airfoils at zero angle of attack and spaced 1 inch apart
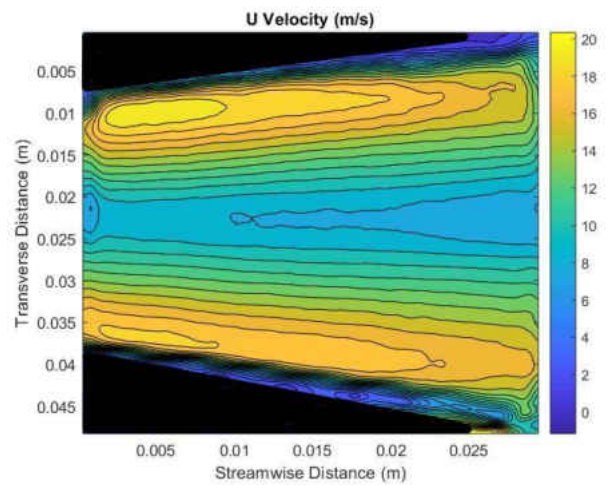
Figure 5.18 U Velocity contour plot of the Bottom Section of the 25 PSI run with airfoils at zero angle of attack and spaced 1 inch apart
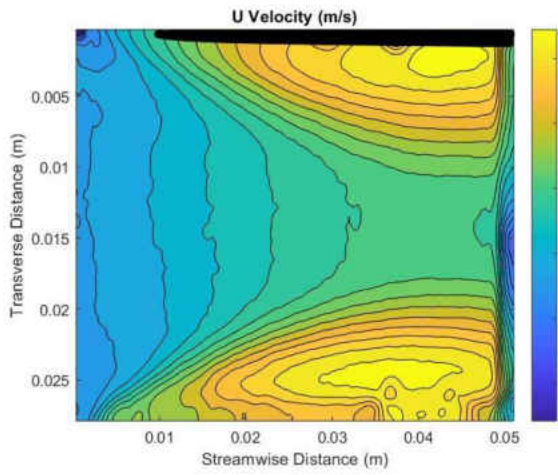
Figure 5.19 U Velocity contour plot of the Mid-Section of the 25 PSI run with airfoils angled 5 degrees inwards and spaced 1 inch apart
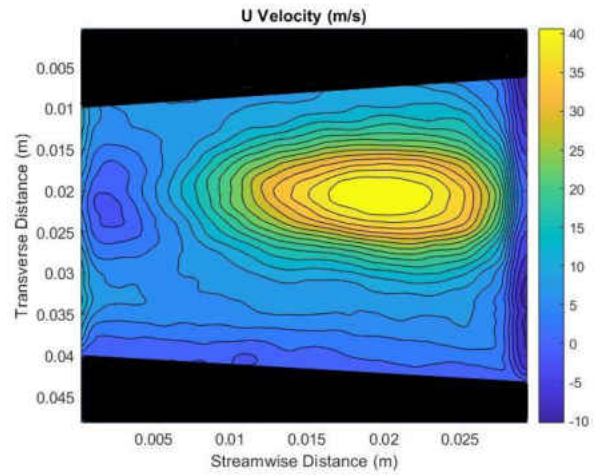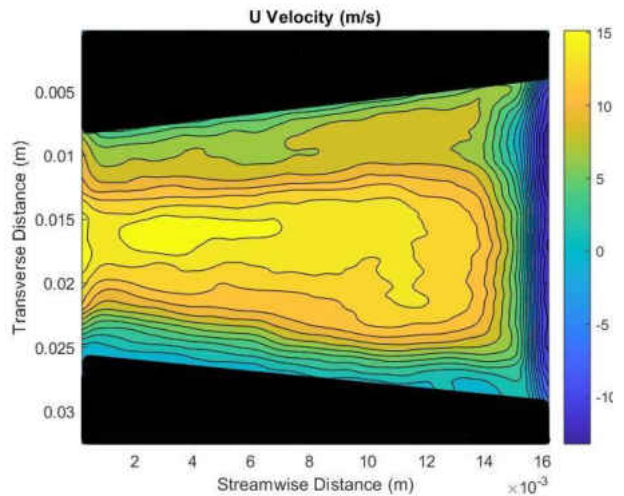
Figure 5.20 U Velocity contour plot of the Bottom Section of the 25 PSI run with airfoils angled 5 degrees inwards and spaced 1 inch apart
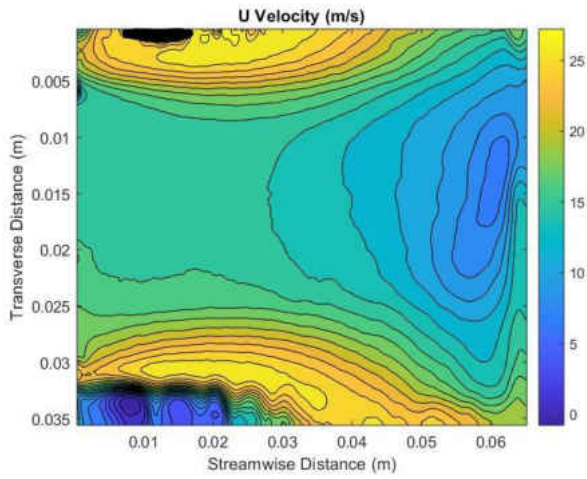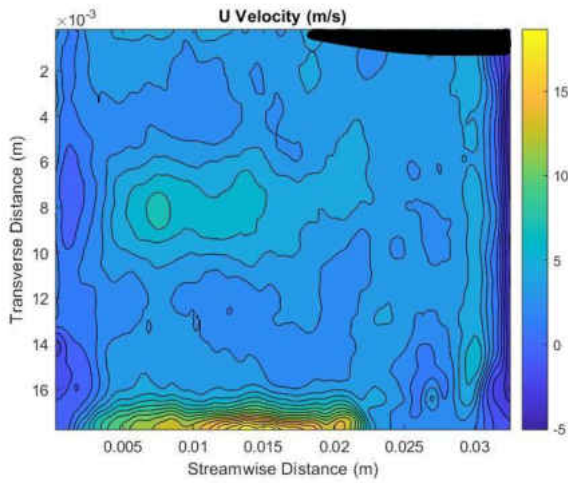
Figure 5.21 U Velocity contour plot of the Mid-Section of the 20 PSI run with airfoils angled 5 degrees outwards and spaced 1 inch apart
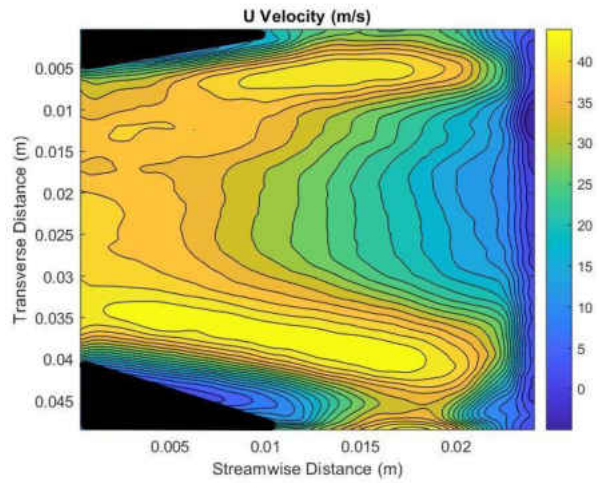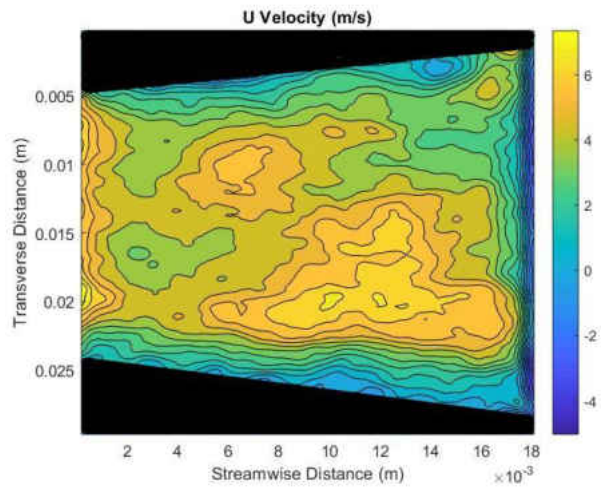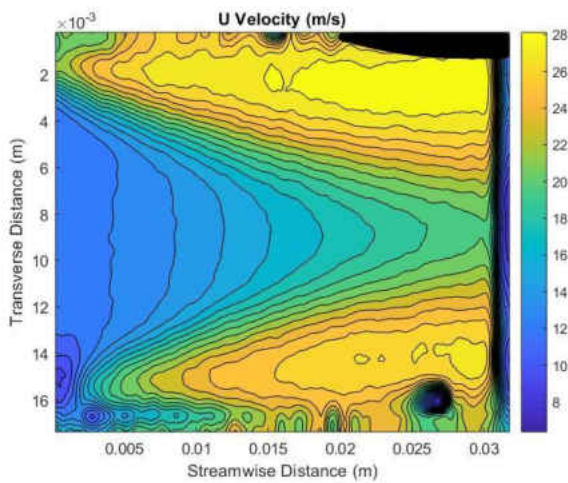

Figure 5.22 U Velocity contour plot of the Bottom Section of the 20 PSI run with airfoils angled 5 degrees outwards and spaced 1 inch apart
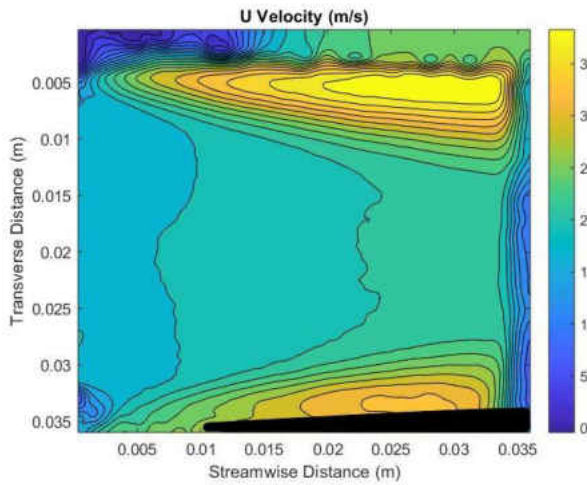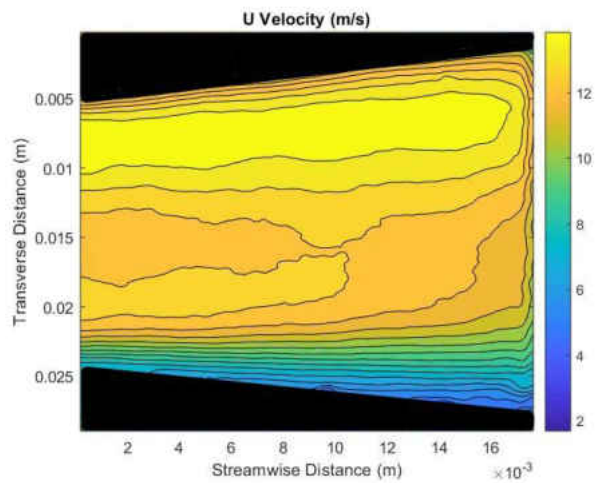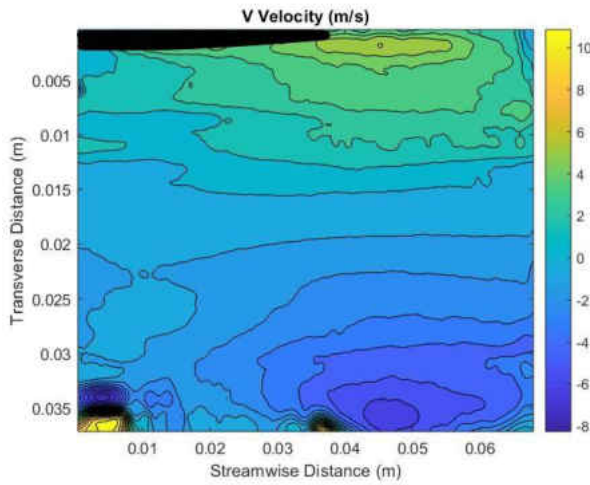

Figure 5.23 U Velocity contour plot of the Mid-Section of the 20 PSI run with airfoils at zero angle of attack and spaced 1 inch apart
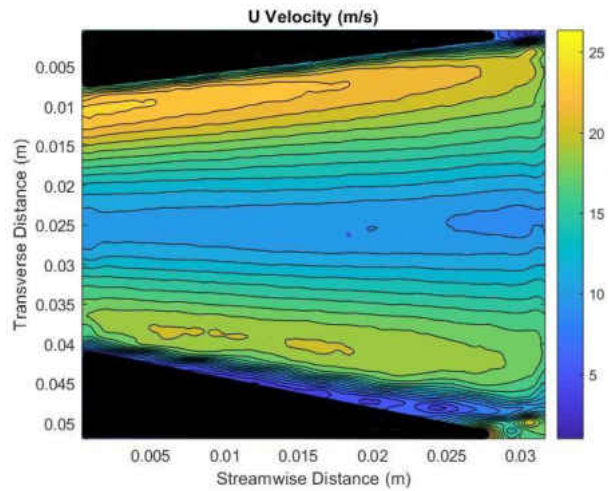
Figure 5.24 U Velocity contour plot of the Bottom Section of the 20 PSI run with airfoils at zero angle of attack and spaced 1 inch apart

112
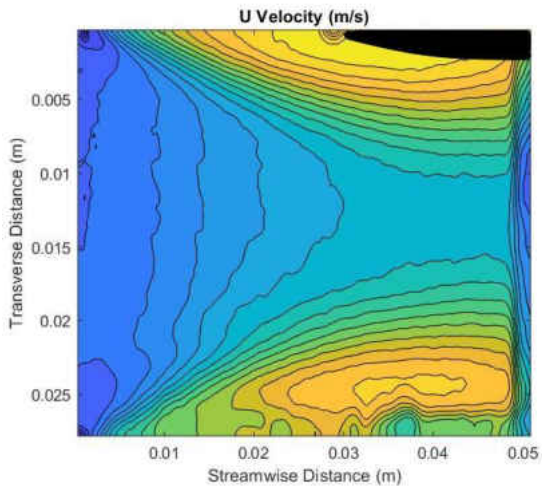
Figure 5.25 U Velocity contour plot of the Mid-Section of the 20 PSI run with airfoils angled 5 degrees inwards and spaced 1 inch apart
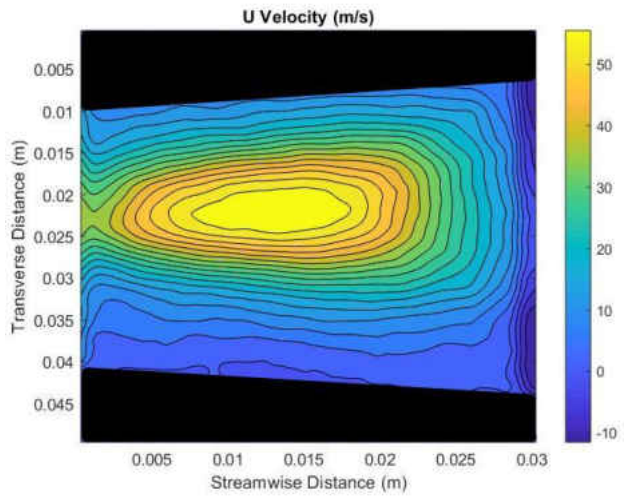
Figure 5.26 U Velocity contour plot of the Bottom Section of the 20 PSI run with airfoils angled 5 degrees inwards and spaced 1 inch apart
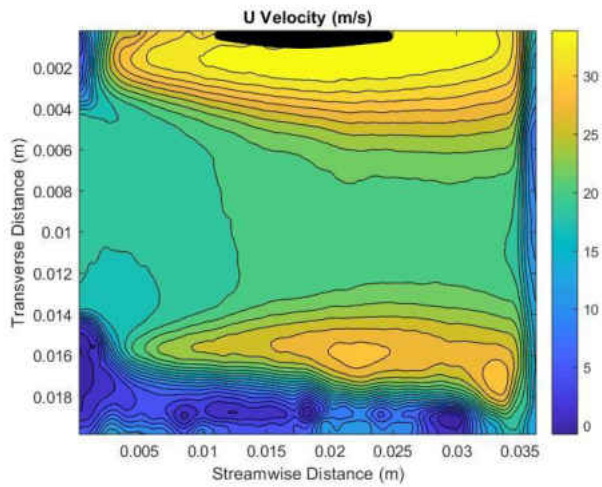
Figure 5.27 U Velocity contour plot of the Mid-Section of the 25 PSI run with airfoils angled 5 degrees outwards and spaced .5 inch apart

Figure 5.28 U Velocity contour plot of the Mid-Section of the 20 PSI run with airfoils angled 5 degrees outwards and spaced .5 inch apart

Figure 5.29 U Velocity contour plot of the Bottom Section of the 20 PSI run with airfoils angled 5 degrees outwards and spaced .5 inch apart

114

Figure 5.30 U Velocity contour plot of the Mid-Section of the 25 PSI run with airfoils at zero angle of attack and spaced .5 inch apart
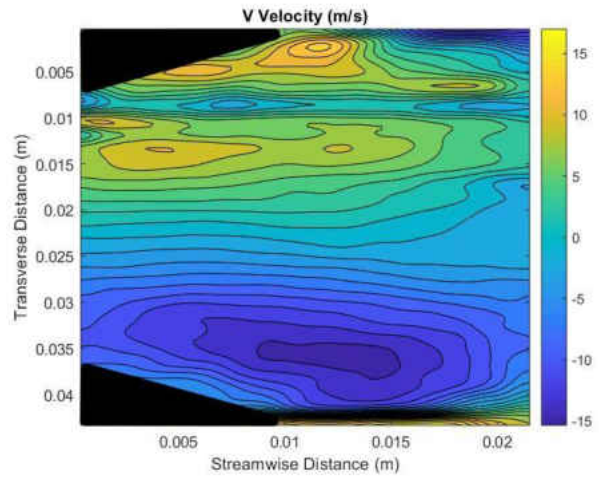

Figure 5.31 U Velocity contour plot of the Bottom Section of the 25 PSI run with airfoils at zero angle of attack and spaced .5 inch apart
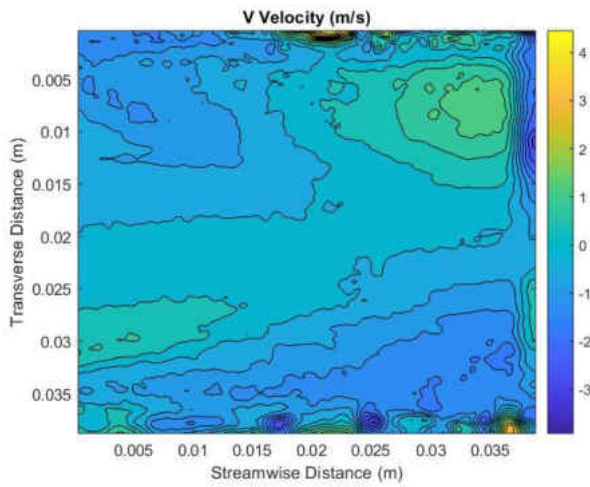

Figure 5.32 U Velocity contour plot of the Mid-Section of the 20 PSI run with airfoils at zero angle of attack and spaced .5 inch apart

Figure 5.33 U Velocity contour plot of the Bottom Section of the 20 PSI run with airfoils at zero angle of attack and spaced .5 inch apart

115

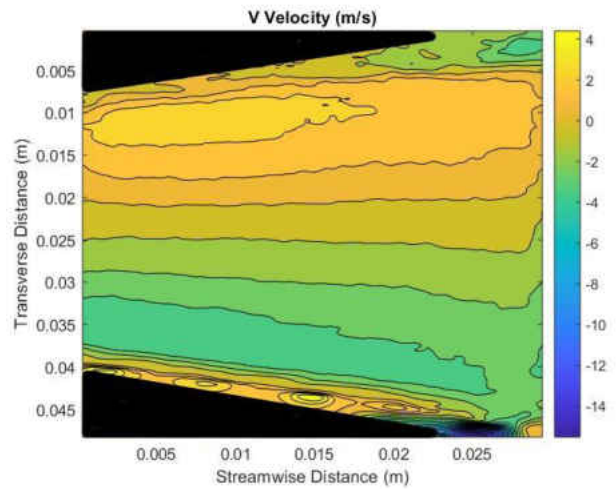# APPENDIX D: V VELOCITY CONTOUR MAPS

Figure 5.34 V Velocity contour plot of the Mid-Section of the 25 PSI run with airfoils angled 5 degrees outwards and spaced 1 inch apart
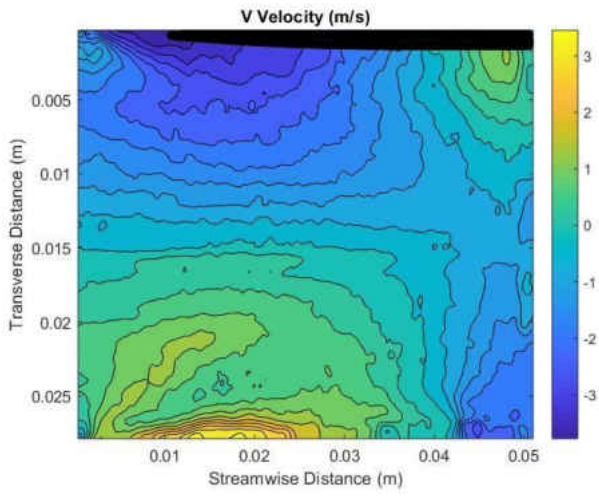

Figure 5.35 V Velocity contour plot of the Bottom Section of the 25 PSI run with airfoils angled 5 degrees outwards and spaced 1 inch apart
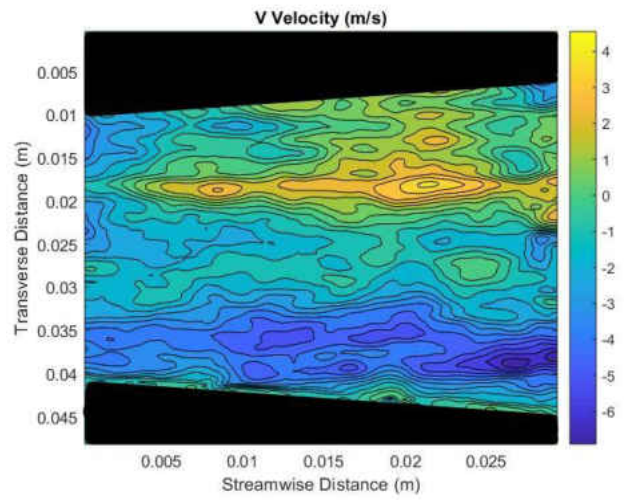

Figure 5.36 V Velocity contour plot of the Mid-Section of the 25 PSI run with airfoils at zero angle of attack and spaced 1 inch apart

Figure 5.37 V Velocity contour plot of the Bottom Section of the 25 PSI run with airfoils at zero angle of attack and spaced 1 inch apart
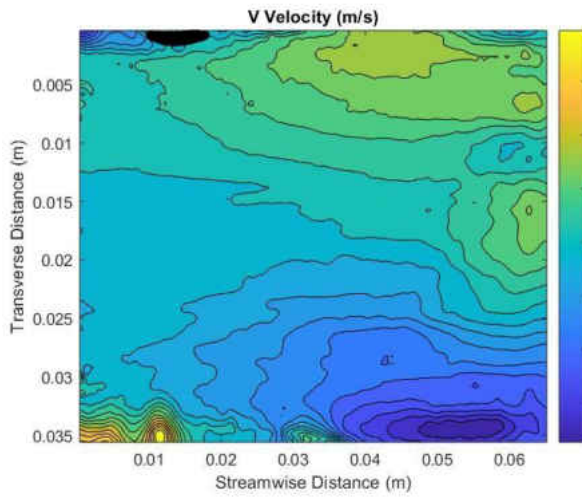
117

Figure 5.38 V Velocity contour plot of the Mid-Section of the 25 PSI run with airfoils angled 5 degrees inwards and spaced 1 inch apart
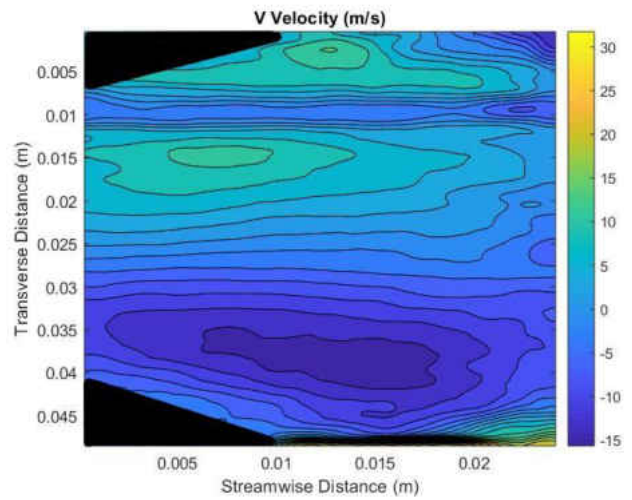

Figure 5.39 V Velocity contour plot of the Bottom Section of the 25 PSI run with airfoils angled 5 degrees inwards and spaced 1 inch apart
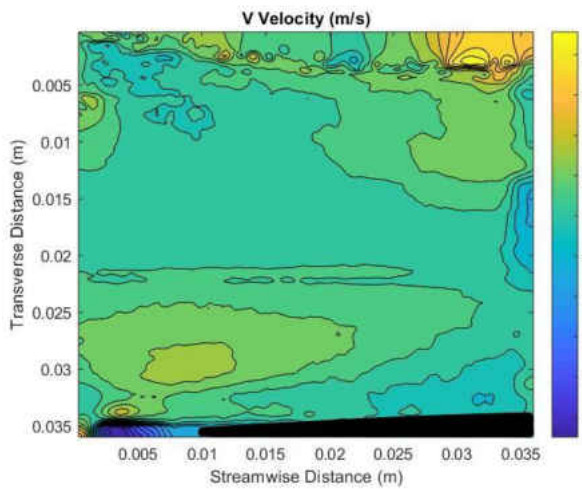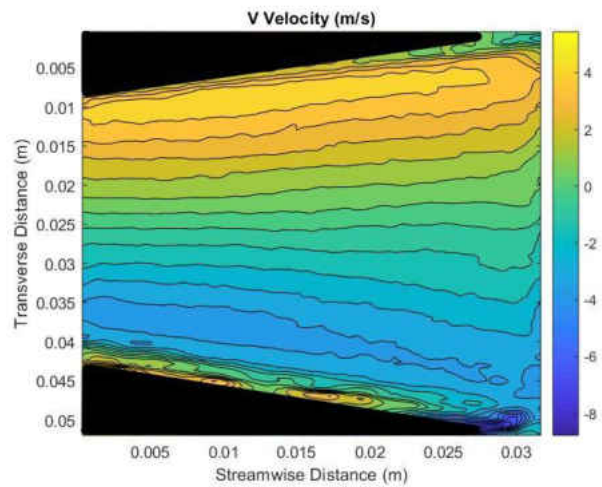
Figure 5.40 V Velocity contour plot of the Mid-Section of the 20 PSI run with airfoils angled 5 degrees outwards and spaced 1 inch apart

Figure 5.41 V Velocity contour plot of the Bottom Section of the 20 PSI run with airfoils angled 5 degrees outwards and spaced 1 inch apart

Figure 5.42 V Velocity contour plot of the Mid-Section of the 20 PSI run with airfoils at zero angle of attack and spaced 1 inch apart

Figure 5.43 V Velocity contour plot of the Bottom Section of the 20 PSI run with airfoils at zero angle of attack and spaced 1 inch apart

119

Figure 5.44 V Velocity contour plot of the Mid-Section of the 20 PSI run with airfoils angled 5 degrees inwards and spaced 1 inch apart
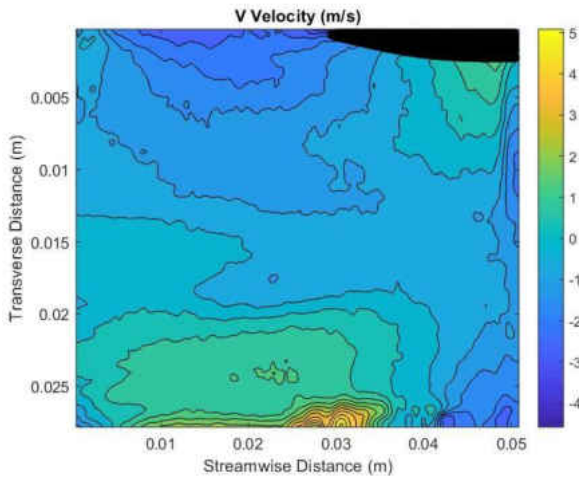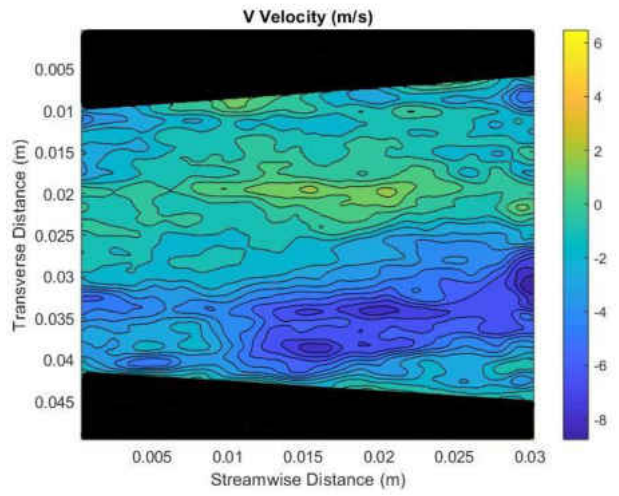

Figure 5.45 V Velocity contour plot of the Bottom Section of the 20 PSI run with airfoils angled 5 degrees inwards and spaced 1 inch apart

Figure 5.46 V Velocity contour plot of the Mid-Section of the 25 PSI run with airfoils angled 5 degrees outwards and spaced .5 inch apart

Figure 5.47 V Velocity contour plot of the Mid-Section of the 20 PSI run with airfoils angled 5 degrees outwards and spaced .5 inch apart

Figure 5.48 V Velocity contour plot of the Bottom Section of the 20 PSI run with airfoils angled 5 degrees outwards and spaced .5 inch apart

121

Figure 5.49 V Velocity contour plot of the Mid-Section of the 25 PSI run with airfoils at zero angle of attack and spaced .5 inch apart
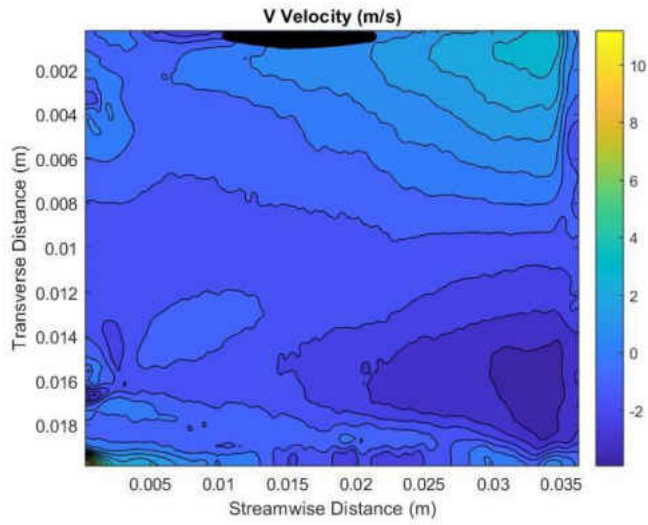

Figure 5.50 V Velocity contour plot of the Bottom Section of the 25 PSI run with airfoils at zero angle of attack and spaced .5 inch apart
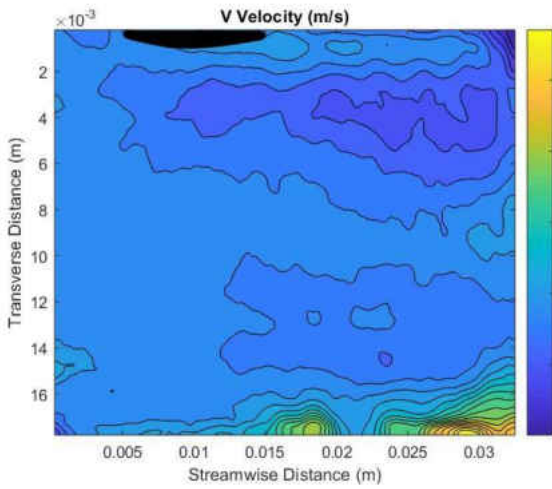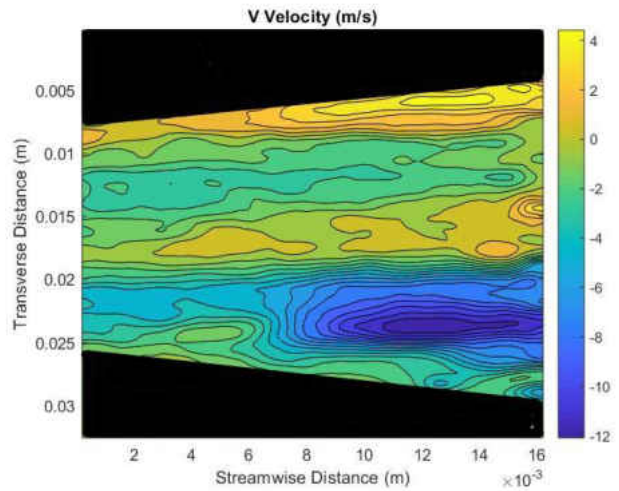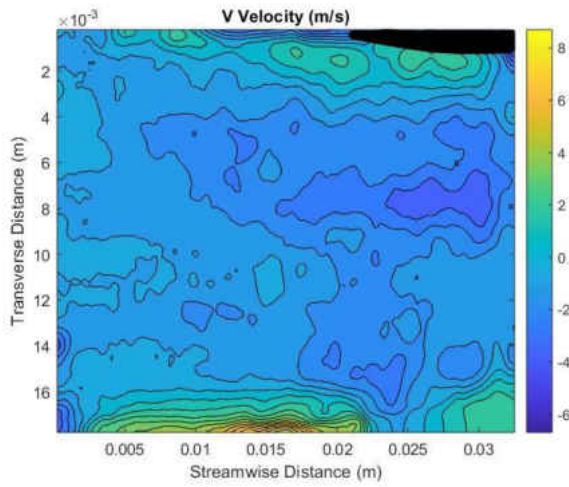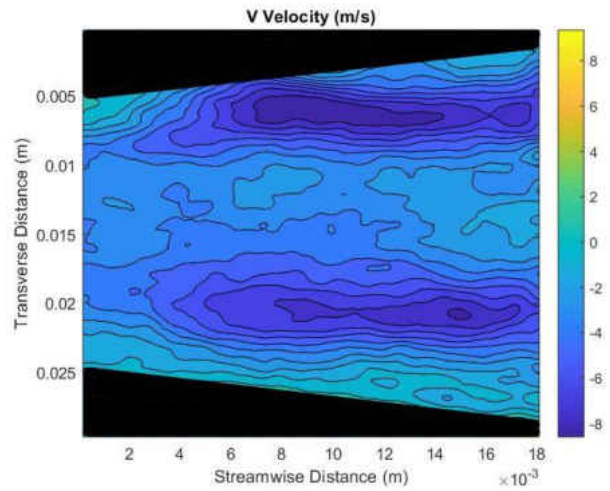

Figure 5.51 V Velocity contour plot of the Mid-Section of the 20 PSI run with airfoils at zero angle of attack and spaced .5 inch apart
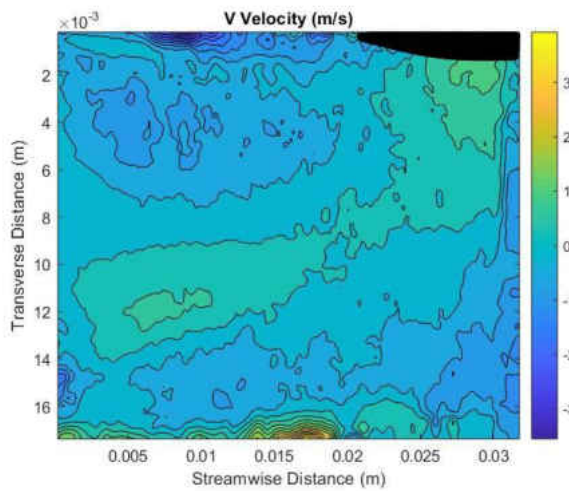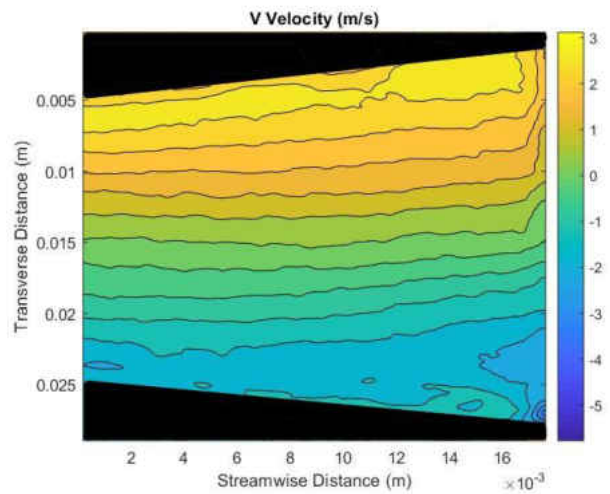

Figure 5.52 V Velocity contour plot of the Bottom Section of the 20 PSI run with airfoils at zero angle of attack and spaced .5 inch apart

REFERENCES

[1] Spall, Robert E. "Momentum Flux in Plane Parallel Jets" *ASME Journal of Fluids Engineering* Volume 126. (2004): 665-670. Asme.org. 12/24/2018

[2] C.D. Winant, F.K. Browand. "Vortex Pairing: the mechanism of turbulent mixing-layer growth at moderate Reynolds number" *Journal of Fluid Mechanics* Vol. 63. Issue 2 (1974): 237-255. Cambridge Journals. 11/22/2018

[3] Bevilaqua, Paul, et al. "Jet Entrainment Theory for Vertical Takeoff and Landing Aircraft Suckdown." *AIAA Journal*, vol. 48, no. 2, Feb. 2010, pp. 330–339.

[4] https://www.businessinsider.com/commercial-uav-market-analysis-2017-8

[5] Holland Michel, Arthur and Dan Gettinger. "*Drone Year in Review: 2017*," Center for the Study of the Drone at Bard College, January 3, 2018, http://dronecenter.bard.edu/drone-year-in-review-2017/.

[6] Davidson, P.A. *Turbulence: An Introduction for Scientist and Engineers*. Oxford University Press, 2004.

[7] Arroyo, Jaen, et al. "IEEE Mexican Humanitarian Technology Conference (MHTC)." IEEE, *UAV Technology and Machine Learning Techniques Applied to the Yield Improvement in Precision Agriculture*, 2017, pp. 137–143.

[8] "MILCOM 2018 - 2018 IEEE Military Communications Conference (MILCOM)." IEEE, *Autonomous, Cooperative UAV Operations Using COTS Consumer Drones and Custom Ground Control Station*, 2018, pp. 1–6.

[9] Dewid, Jessica. "This Shocking Video Shows What Happens When a Drone Crashes into a Plane." *Business Insider*, Business Insider, 8 Nov. 2018,

www.businessinsider.com/shocking-video-shows-what-happens-when-a-drone-crashes-into-a-plane-2018-11

[10] Ungerleider, Neal. "What Happens When A Drone Crashes?" *Fast Company*, Fast Company, 9 Apr. 2014, www.fastcompany.com/3028781/what-happens-when-a-drone-crashes.

[11] Nicas, Jack. "What Happens When Your Drone Escapes -- Safety Risks, Rise in Novice Pilots Pose Big Challenge for Burgeoning Industry." *Wall Street Journal*, 9 Dec. 2014.

[12] Brentner, Kenneth S. *Modeling Aerodynamically Generated Sound: Recent Advances in Rotor Noise Prediction*. American Institute of Aeronautics and Astronautics, 2000, pp. 1–11

[13] Kusyumov, Alexander, et al. "CAA Modeling of Helicopter Main Rotor in Hover." *EDP Sciences*, vol. 143, 2017, pp. 1–6.

[14] Hu, Bing, et al. "The Influence of Large-Scale Structures on Entrainment in a Decelerating Transient Turbulent Jet Revealed by Large Eddy Simulation." *Physics of Fluids*, vol. 24, 16 Apr. 2012, pp. 045106–1-045106–17.

[15] Tanaka, Eiichi. "The Interference of Two-Dimensional Parallel Jets (1st Report Experiments on Dual Jets)" *Journal of Japan Society of Mechanical Engineers*, Vol. 13, No. 56, 1970, pp. 272-280

[16] Tanaka, Eiichi. "The Interference of Two-Dimensional Parallel Jets (2nd Report)" *Journal of Japan Society of Mechanical Engineers*, Vol. 17, No. 109, 1974, pp. 920-927

[17] Anderson, E and Spall, R. "Experimental and Numerical Investigation of Two-Dimensional Parallel Jets" *Journal of Fluids Engineering,* Vol. 123, 2001, pp. 401-406

[18] Nasr, A and Lai, J.C. "Comparison of Flow Characteristics in the near field of two parallel plane jets and an offset plane jet." *Physics of Fluids,* Vol. 9, (1997), 2919-2931

[19] Lin, Y.F. and Sheu, M.J. "Interaction of Parallel Turbulent Plane Jets" *AIAA Journal*, Vol. 29, No. 9. 1372-1373

[20] Stickney, Timothy, et al. *Fan Assembly*. Pat. 10,100,836. 19 Apr. 2012.

[21] Kumar, Naveen, et al. "IOP Conference Series: Material Science and Engineering." IOP Publishing, *Design and Optimization of Aerospike Nozzle Using CFD*, 2017, pp. 1–30.

[22] Currie, I.G. *Fundamental Mechanics of Fluids.* CRC Press, 2013

[23] Schlipf, D, et.al. "Testing of Frozen Turbulence Hypothesis for Wind Turbine Applications with a Scanning LIDAR System." *In Detailed Program ISARS*, 2010, 1-5

[24]Ho, Chin-Ming, and Gutmark Ephrain. "Vortex Induction and Mass Entrainments in a small-aspect-ratio elliptic jet." *Journal of Fluid Mechanics*, Vol. 179, pp. 383-405.

[25] Ho, Chih-Ming, and Huerre, Patrick. "Perturbed Free Shear Layers." *Annual Review of Fluid Mechanics*, Vol. 16, 1984, pp. 365-424

[26] Tennekes & Lumley, A First Course in Turbulence, MIT Press, 1972 (14th printing: 1992).

[27] Pope, Stephen. *Turbulent Flows*. Cambridge University Press, 2000.

[28] Agrawal, A. K, Prasad. "Properties of vortices in the self-similar turbulent jet" *Experiments in Fluids*, Vol. 33, 2002, pp. 565-577

[29] Wygnanski, I. and Fielder, H. "Some Measurements in the Self-Preserving Jet." *Journal of Fluid Mechanics*, Vol. 38, part 3, 1969, pp.577-612

[30] Crow, S.C, and Champagne, F.H. "Orderly Structure in Jet Turbulence." *Journal of Fluid Mechanics*, Vol. 48, part 3, 1971, pp.547-591

[31] Verma, S.B., and Rathakrishnan, E. "Flow and Acoustic Properties of Underexpanded and Elliptic-Slot Jets." *Journal of Propulsion and Power*, Vol. 17, No. 1, Feb. 2001, 49-57

[32] Gutmark, Ephraim and Schadow, Klaus. "Flow Characteristics of orifice and tapered jets." *Physics of Fluids*, Vol. 30, 1987, pp. 3448-3454

[33] Hussain, A. K. M. F. and Ramjee, V. "Effects of the Axisymmetric Contraction Shape on Incompressible Turbulent Flow." *Journal of Fluids Engineering*, March 1976, pp.58-68

[34] Sfeir, A.A. "Investigation of Three-Dimensional Turbulent Rectangular Jets." *AIAA Journal*, Vol. 17, No. 10, October 1979, pp. 1055-1060

[35]"Thrust Augmentation." *Merriam-Webster*, Merriam-Webster, 2019, www.merriam-webster.com/dictionary/thrust%20augmentation.

[36] Banazadeh, A., and F. Saghafi. "An Investigation of Empirical Formulation and Design Optimization of Co-Flow Fluidic Thrust Vectoring Nozzles." *AERONAUTICAL JOURNAL*, vol. 121, no. 1236, pp. 213–236. *EBSCOhost*, doi:10.1017/aer.2016.110. Accessed 21 Jan. 2019.

[37] Bevilaqua, Paul. "Lifting Surface Theory for Thrust-Augmenting Ejectors ." *AIAA Journal*, vol. 16, no. 5, May 1978, pp. 475–481.

[38] Florin, Frunzulica, et al. "2018 9th International Conference on Mechanical and Aerospace Engineering." IEEE, *A Passive Flow Control Method Based on the Coandă Effect*, 2018, pp. 306–310.

[39] Lund, T.S. "Augmented Thrust and Mass Flow Associated with Two-Dimensional Jet Reattachment." *AIAA Journal*, vol. 24, no. 12, Dec. 1986, pp. 1964–1970.

[40] Saghafi, F, and A Banazadeh. "Investigation on the Flight Characteristics of a Conceptual Fluidic Thrust-Vectored Aerial Tail-Sitter." *Institute for Mechanical Engineers*, vol. 221, no. G, 2007, pp. 741–755.

[41] Banazadeh, A, et al. "Experimental and Computational Investigation into the Use of Co-Flow Fluidic Thrust Vectoring on a Small Gas Turbine." *The Aeronautical Journal*, Jan. 2008, pp. 17–24.

[42] Bevilaqua, Paul. "47th AIAA Aerospace Sciences Meeting ." AIAA, *Inventing the F-35 Joint Strike Fighter*, 2009, pp. 1–18.

[43] Heiser, W. "Ejector Thrust Augmentation," *Journal of Propulsion and Power* Vol. 26, No. 6, 2010, pp. 1325-1330.

[44] Wiedow, B and Ahmed, K. "Performance characteristics of Slot Jet Propulsion System Using Fluidic Thrust Augmentation for Use in Unmanned Aerial Vehicle Application" *AIAA Journal*

[45] Joint Committee for guides in Metrology. "Evaluation of Measurement Data-Guide to the Expression of Uncertainty in Measurement ." *Bureau International Des Poids Et Mesures*, Sept. 2008, www.bipm.org.

[46] Clark, Edward. "Error Propagation Equations for Estimating the Uncertainty in High-Speed Wind Tunnel Test Results." *Association for Information and Image Management*, 1994.

[47] Bendat, Julius, and Allan Piersol. *Random Data Analysis and Measurement Procedures*. 3rd ed., Wiley-Interscience Publications, 2000.

[48] Thielicke, W and Stamhuis, E J "PIVlab – Towards User-friendly, Affordable and Accurate Digital Particle Image Velocimetry in MATLAB". *Journal of Open Research Software*, 2014, 2: e30, DOI: http://dx.doi.org/10.5334/jors.bl